UNIVERSITY OF CALIFORNIA

Los Angeles

Mixing and transport of materials in the Ocean Surface Boundary Layer

A dissertation submitted in partial satisfaction

of the requirements for the degree

Doctor of Philosophy in Atmospheric and Oceanic Sciences

by

Tomas Luis Guimaraes Chor

2020

ABSTRACT OF THE DISSERTATION

Mixing and transport of materials in the Ocean Surface Boundary Layer

by

Tomas Luis Guimaraes Chor
Doctor of Philosophy in Atmospheric and Oceanic Sciences
University of California, Los Angeles, 2020
Professor Marcelo Chamecki, Chair

Turbulence in the ocean surface boundary layer (OSBL) directly controls transport and dispersion of passive materials near the ocean surface. Many such materials directly affect human and ecosystem health and human activities (e.g. microplastic, oil and nutrients and phytoplankton) as well as climate-change-relevant global budgets (e.g. carbon dioxide), making their mixing and transport mechanisms an important topic of investigation. However, the dynamics of the upper ocean are such that most of the processes and flow structures that are relevant to such transport are too small to be investigated with global circulation models and challenging to be investigated with field and laboratory experiments. As a result much is unknown about how the transport and mixing of materials is affected by OSBL turbulence in different regimes, particularly when surface waves are present, which have no analog in atmospheric boundary layers.

Based on these considerations, this dissertation is dedicated to the investigation of passive material transport and mixing in OSBLs under generalized regimes (i.e. regimes that are a combination of convection, wind-stress-driven turbulence and wave-driven turbulence). Focus is given to small-scale processes (smaller than an OSBL depth) and the tool of choice is the large-eddy simulation (LES) technique, which can resolve the relevant eddies for transport while parameterizing smaller ones.

One of the contributions of this dissertation is the exploration of a wide range of upper ocean

regimes and its analysis over a general framework. This is challenging since the dynamics of these regimes can be extremely different from each other, which reflects on material transport as extremely different outcomes for different regimes. Furthermore, another major contribution is the development of a method to aid in the development of eddy-diffusivity models for OSBL mixing. While development of such models has historically depended on choices of scaling laws and shape functions that have to be made *a priori* (and therefore constrain the outcome), the method developed here does not make any such assumptions. Thus, all results naturally emerge from data. Finally, after showing that results conform to current knowledge of upper ocean physics, we modify existing models accordingly and show that results are improved with the adopted modifications.

The dissertation of Tomas Luis Guimaraes Chor is approved.

Jonathan M. Aurnou

Andrew L. Stewart

James C. McWilliams

Marcelo Chamecki, Committee Chair

University of California, Los Angeles

2020

To my family.

TABLE OF CONTENTS

LIST OF FIGURES

LIST OF TABLES

ACKNOWLEDGMENTS

Chapter 2 is reproduced from Chor et al. (2018a), Chapter 3 is reproduced from Chor et al. (2020b)[1], Chapter 4 is reproduced from Chor et al. (2020a, preliminary version not yet submitted) and Appendix A is reproduced from Chor et al. (2018b). All four publications are supported by a grant from the Gulf of Mexico Research Initiative and the ones that are already published are reproduced with permission from the publishers.

[1] © American Meteorological Society. Used with permission. This preliminary version has been accepted for publication in the Journal of the Atmospheric Sciences and may be fully cited. The final typeset copyedited article will replace the EOR when it is published

VITA

2019 Richard P. Turco exceptional research award, UCLA: for exceptional research publication.

2018 M.S. (Atmospheric and Oceanic Sciences), UCLA.

2014 Odelar Leite Linhares award, Brazilian Society for Applied and Computational Mathematics: for best Masters thesis in Applied and Computational Mathematics in Brazil.

2014 M.S. (Environmental Engineering), Federal University of Paraná.

2012 B.S. (Environmental Engineering), Federal University of Paraná.

PUBLICATIONS

Tomas Chor, James C. McWilliams, and Marcelo Chamecki. "Diffusive-nondiffusive flux decompositions in atmospheric boundary layers". In: Journal of the Atmospheric Sciences (2020), pp. 1–55. DOI: 10.1175/JAS-D-20-0093.1

Marcelo Chamecki, Tomas Chor, Di Yang, and Charles Meneveau. "Material transport in the ocean mixed layer: recent developments enabled by large eddy simulations". In: Reviews of Geophysics 57.4 (2019), pp. 1338–1371. DOI: 10.1029/2019RG000655.

Tomas Chor, Ailín Ruiz de Zárate, and Nelson L. Dias. "A Generalized Series Solution for the Boussinesq Equation With Constant Boundary Conditions". In: Water Resources Research 55.4 (2019), pp. 3567–3575. DOI: 10.1029/2018WR024154.

Cléo Quaresma Dias-Júnior et al. “Is There a Classical Inertial Sublayer Over the Amazon Forest?” In: Geophysical Research Letters 46.10 (2019), pp. 5614–5622. DOI: 10.1029/2019GL083237.

Tomas Chor, Di Yang, Charles Meneveau, and Marcelo Chamecki. “A Turbulence Velocity Scale for Predicting the Fate of Buoyant Materials in the Oceanic Mixed Layer”. In: Geophysical Research Letters 45.21 (2018), pp. 11–817. DOI: 10.1029/2018GL080296.

Tomás Chor, Di Yang, Charles Meneveau, and Marcelo Chamecki. “Preferential concentration of noninertial buoyant particles in the ocean mixed layer under free convection”. In: Phys. Rev. Fluids 3 (2018), p. 064501. DOI: 10.1103/PhysRevFluids.3.064501.

Tomás L. Chor et al. “Flux-variance and flux-gradient relation- ships in the roughness sublayer over the Amazon forest”. In: Agricultural and Forest Meteorology 239 (2017), pp. 213–222. DOI: 10.1016/j.agrformet.2017.03.009.

Einara Zahn, Tomas L. Chor, and N. L. Dias. “A Simple Methodology for Quality Control of Micrometeorological Datasets”. In: American Journal of Environmental Engineering 6.4A (2016), pp. 135–142. DOI: 10.5923/s.ajee.201601.20.

Tomas L. Chor and Nelson L. Dias. “Technical Note: A simple generalization of the Brutsaert and Nieber analysis”. In: Hydrology and Earth System Sciences 19.6 (2015), pp. 2755–2761. DOI: 10.5194/hess-19-2755-2015.

Tomas Chor, Nelson L. Dias, and Ailín Ruiz de Zárate. “An exact series and improved numerical and approximate solutions for the Boussinesq equation”. In: Water Resources Research 49.11 (2013), pp. 7380–7387. DOI: 10.1002/wrcr.20543.

CHAPTER 1

Introduction

1.1 Introduction of the problem

One of the challenges of current oceanic sciences research is to understand and predict the vertical mixing and horizontal transport of properties in the Ocean Surface Boundary Layer (OSBL; the upper layer of the ocean which is defined and described in Section 1.2). A subset of that problem is the transport and mixing of passive scalar quantities, which are properties that are present in the flow but do not affect it. Examples of scalars of interest for oceanic studies include dissolved gases, dissolved nutrients, phytoplankton, oil and microplastic. Tracking such quantities in the ocean is important not only for assessing ecosystem health (Denman et al., 1995; Mendelssohn et al., 2012; Worm et al., 2017) but also for human activities and human health (Cherry et al., 2015) and subjects that directly relate to climate change such as the carbon budget (Chen et al., 1986; Houghton, 2007). With these issues in mind, this dissertation is dedicated to the investigation of vertical mixing of passive scalars in the OSBL under generalized oceanic regimes.

There are several aspects of this topic that make it challenging. Field observations of the upper ocean are difficult and few (D'Asaro, 2014) and laboratory experiments also face a number of challenges (Melville et al., 1998), which makes reliance on numerical models imperative. Numerical studies, however, are of limited help since scalar transport is affected by turbulent flow structures that range (conservatively) from a few centimeters in the vertical direction (OSBL turbulence) to many kilometers in the horizontal directions (Chamecki et al., 2019). Although there are alternative approaches which try to simulate both small and large scales simultaneously (Malecha et al., 2014; Chen et al., 2016b), a simulation that truly includes all relevant scales for scalar transport including their interactions is still unfeasible (and will probably remain so for a many years (Pope, 2000,

Chapter 8)), with the largest possible small-eddy-resolving domain sizes currently being on the order of 10 km in the horizontal directions and 100 m in the vertical direction (Hamlington et al., 2014).

Due to these challenges, our efforts to numerically investigate scalar transport mostly rely on two approaches. One approach is to run small-domain numerical experiments to identify, understand, and develop models for the relevant small-scale physical phenomena (e.g. McWilliams et al. (2000), Hamlington et al. (2014), Yang et al. (2015), and Kukulka et al. (2016)). The second approach consists of large-domain experiments which parameterize small-scale phenomena with the aforementioned models and focus on large scale transport (e.g. Uchiyama et al. (2017), Dauhajre et al. (2017), and Thyng (2019)). In this dissertation we take the former approach and perform fine-resolution, small-domain numerical simulations. The main focus lies in investigating scalar transport and mixing in scales that are smaller than $\mathcal{O}$(100 m), with the main general goals of broadening our understanding of these processes and informing the models that ultimately parameterize their effects (more specific goals are defined in Section 1.3).

1.2 Physical background

1.2.1 Ocean surface boundary layers

We focus on scalar transport within the OSBL, which is the weakly stratified upper layer of the ocean and serves as an interface between the atmosphere and deep ocean. Its depth depends on specific ocean surface conditions but it is generally $\mathcal{O}$(10-100 m), which makes it a thin layer when compared to the whole ocean (McWilliams, 2006, Chapter 6). Although small in volume, its role in setting boundary conditions for air-sea fluxes makes it an important piece in the global ocean circulation and, therefore, climate change (Gargett, 1989; Belcher et al., 2012; D'Asaro, 2014; Li et al., 2017). Furthermore, because human interactions with the ocean are generally confined near the surface, OSBL dynamics are of general interest for human activities (Nemani et al., 2001; Cherry et al., 2015; Clements et al., 2017).

The dynamics of the OSBL are strongly influenced by processes induced by the atmospheric

forcing, which transfer energy through the surface and generate turbulence, making it weakly stratified and well mixed (Pedlosky, 1987; McWilliams, 2006). Most notably, there are three main forcings that account for most of the turbulence in the OSBL: buoyancy fluxes, wind and waves (Belcher et al., 2012). Surface buoyancy fluxes happen whenever a process changes the water density at the air-sea interface, which can be done through changes in temperature (via heat fluxes) or salinity (via precipitation or evaporation). These fluxes are widely responsible for the deepening of the OSBL during nighttime (through surface cooling, which creates an instability in the density profile) and shoaling during daytime (Price et al., 1986; McWilliams, 2006). Ocean regimes that are dominated by buoyancy fluxes are called convective (or sometimes free-convection (Wyngaard, 2010)) regimes.

The direct contribution of the wind happens through the wind stress at the surface which injects momentum into the upper layers of the flow and feeds the shear-driven turbulence below. Indirectly, the surface wind stress creates waves, whose particular effects on the flow depend on whether or not they break (which in turn depends on their steepness and wind conditions (Perlin et al., 2013)). For example, nonbreaking waves introduce fluctuations associated with the motion of the free surface. Most notably the orbital motions of nonbreaking waves produce a mean Lagrangian velocity profile that horizontally moves particles called the Stokes drift (McWilliams et al., 1997; Thorpe, 2004), which is generally accepted as the mechanism behind the formation of Langmuir circulations (depicted in Figure 1.1). These are counter-rotating wind-aligned vortices that are often present in the OSBL (Leibovich, 1983). In a wind-driven OSBL the effects of Langmuir circulations generally reorganize and ultimately dominate the flow dynamics, whose turbulent regime came to be known as Langmuir turbulence (McWilliams et al., 1997).

Finally, breaking waves inject momentum into the water column, producing bubbles and sea spray (which perform gas exchanges between the ocean and the atmosphere (Melville, 1996; Sullivan et al., 2010)). The effects of breaking waves on scalar mixing are generally confined to a depth of the order of the wave height, which is generally smaller than a boundary layer depth (Melville, 1996). Due to this fact, and for the sake of simplicity, we neglect the effects of breaking waves throughout this dissertation, limiting ourselves to considering wave effects through the Stokes drift.

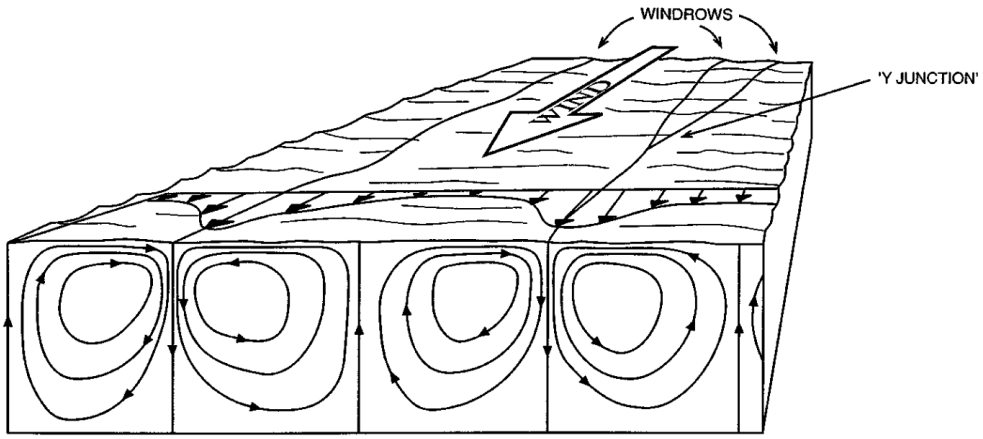

Figure 1.1: Cartoon showing the pattern of mean flow in idealized Langmuir circulation. The Langmuir cells are aligned with the wind and may be $\mathcal{O}$(1-100 m) apart but merge and meander due to the turbulent nature of the flow. Figure reproduced from Thorpe (2004) with permission from the publisher.

In numerical simulations the Stokes drift is generally imposed *a priori* and is not affected by the flow, which allows us to consider it as a forcing process. Thus, the forcings considered throughout this dissertation ultimately are surface wind stresses, surface buoyancy fluxes and nonbreaking waves (parameterized through Stokes drift profiles). Each of these forcings contributes with very different dynamics to the OSBL turbulence. Therefore a buoyancy-flux-dominated OSBL is very different from a wind-dominated OSBL, both of which are also very different from a Langmuir-dominated OSBL. Figure 1.2 illustrates such a difference with the concentration of different sets of buoyant materials in three distinct cases of OSBL regimes. (This figure was reproduced from Chapter 2 and the simulations are explained in detail therein.)

In the left panels of Figure 1.2 we see material concentrated in cell-like patterns on the surface and in thermal plumes that advance downwards, which is typical of a free-convection regime. The middle panels show material concentrated in a roughly horizontally-homogeneous fashion, typical of a surface-wind-stress-dominated regime, which is populated mostly by small eddies (loosely defined for now as eddies significantly smaller than an OSBL depth). The right panels come from a simulation dominated by Langmuir turbulence, where we can see the material organizing in bands at surface (evidence of Langmuir circulations) and within strong regions of downwelling. From Figure 1.2 it becomes clear that the different regimes result in different outcomes for the transport

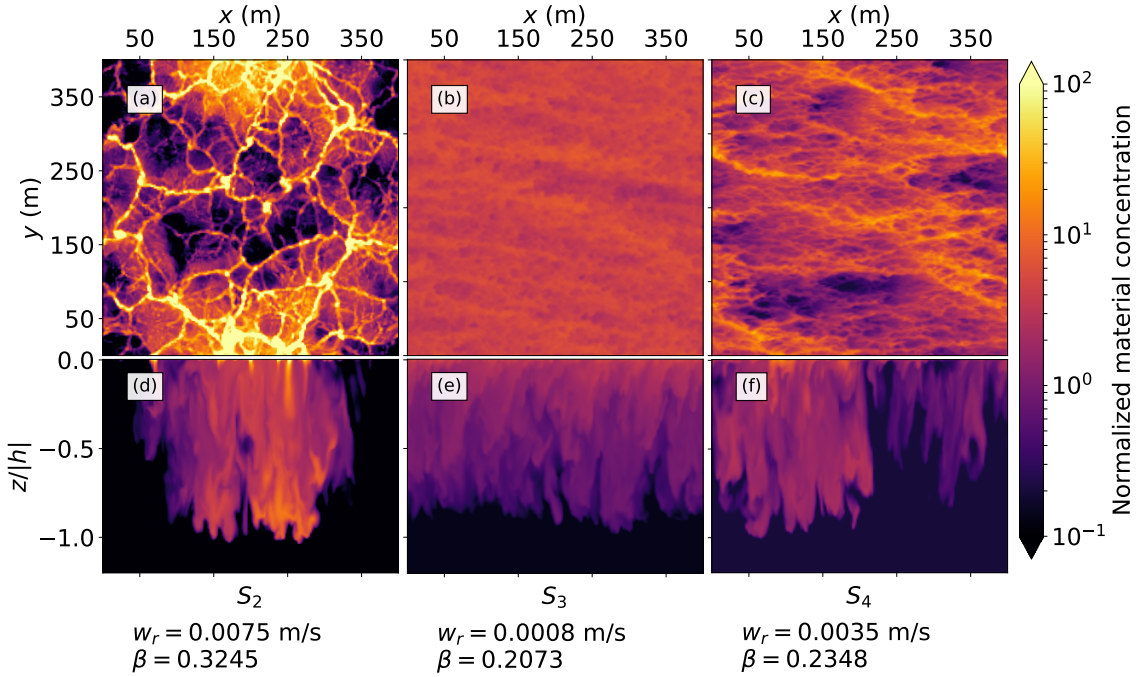

Figure 1.2: Buoyant material concentration under different regimes. Panels a, d: free convection. Panels b, e: wind-shear-dominated. Panels c, f: Langmuir-dominated. Top panels are horizontal cross-sections at the surface, while bottom panels are vertical cross-sections (shown with normalized depth). The captions below the columns indicate the rise velocity of the material w_r and the floatability parameter β (defined in Equation (2.8)) for each simulation. Details about the simulations depicted in the figure in Chapter 2.

and mixing of scalars, and that a theoretical framework that encompasses all possible cases is challenging.

Of all possible regimes emerging from the combination of these three forcings, regimes in which Langmuir circulations are significant are the ones with the most uncertainty among investigators (Thorpe, 2004; Belcher et al., 2012). Incidentally, Langmuir circulations are almost always present in the ocean (Thorpe, 2004; Li et al., 2019), which constitutes a challenge for the correct representation and quantification of scalar transport and mixing in OSBLs.

1.2.2 Passive scalar assumptions and modeling

Throughout this manuscript we consider generic materials that behave approximately without influence of inertial effects, lift forces, added mass, etc. (Ferry et al., 2001), such that they can be

modeled as parcels whose velocity $\boldsymbol{v}$ is given by

$$\boldsymbol{v} = \boldsymbol{u} + w_r \boldsymbol{e}_3, \tag{1.1}$$

where $\boldsymbol{v}$ is the total particle velocity, $\boldsymbol{u}$ is the flow velocity, w_r is the particle terminal rise velocity, and $\boldsymbol{e}_3$ is the unit vector in the vertical upward-pointing direction. Equation (1.1) is known to be a good approximation for most material of interest in the OSBL, with the possible exception of large bubbles in the presence of breaking waves (Chamecki et al., 2019). In the case of dissolved gases and nutrients, $w_r = 0$ (since the scalar follows water parcels) and when modeling materials like microplastic or oil, $w_r > 0$ (for the purposes of this dissertation). In all cases we consider the scalar concentration to be large enough to make an Eulerian approach valid and small enough to neglect feedback on the flow (Ferry et al., 2001).

1.2.3 K-profile parameterization

A large part of the work described in this dissertation relies, in one way or another, on the K-profile parameterization (KPP; Large et al. (1994)), which can be expressed as

$$\left\langle w'c' \right\rangle = -K(z)\frac{\partial \langle C \rangle}{\partial z} + F_{ND}, \tag{1.2}$$

where z is the vertical coordinate, C is the scalar concentration, c' is its turbulent fluctuation, $K(z)$ is its eddy diffusivity, F_{ND} is the nondiffusive component of the turbulent flux and $\langle \cdot \rangle$ is a horizontal and temporal averaging operator. Gradient models like KPP are widely used due to the fact that they generally produce reasonable results and due to their extreme simplicity (Corrsin, 1975; Large et al., 1994; Ghannam et al., 2017). Implied in its formulation is the assumption that part of the turbulent fluxes can be represented by a diffusive mathematical operator ($F_D = -K(z)\frac{\partial \langle C \rangle}{\partial z}$) while another part cannot ($F_{ND}(z)$). This has historically been associated with local and nonlocal processes of the flow, respectively, even though there is evidence that this may not be the case (Zhou et al., 2018).

While $F_{ND}(z)$ can be neglected in some specific applications (e.g. Chapter 2 and Liang et al. (2018)), this component is generally necessary whenever some level of convection is present (see Chapters 3 and 4). In the OSBL there is evidence that nonbreaking waves affect this term (Chen

et al., 2016a), but there is no consensus on the quantitative aspects, which is one of the questions tackled by this dissertation (see Section 1.3). A large part of the contributions of this dissertation is focused on the representation of $F_{ND}(z)$ in wavy situations (see Chapter 4).

1.3 Objectives

Based on the previous discussion, we list the main objectives of this dissertation below:

Objective 1 Investigate how different oceanic regimes impact the vertical mixing of passive scalars with a focus on quantifying Langmuir effects.

Objective 2 Develop a theoretical framework to inform development of KPP-like models.

Objective 3 Quantify the effects of vertical mixing on horizontal transport of passive scalars.

Objective 1 is motivated by our uncertainties regarding ocean regimes given the huge number of possible combinations of the three main forcings relevant to the real ocean. Given this large range, it is common for studies to focus on specific subsets of the parameter space, which may make it challenging to obtain a complete picture of scalar mixing — e.g. most studies focus either on Langmuir-dominated regimes or convection-dominated regimes, rarely combining Langmuir and convection systematically. We thus aim for a more complete picture including a wide range of regimes. We focus on quantitative aspects of wave effects in particular, since much of the uncertainty is due to Langmuir circulations. Although it has been confirmed that Langmuir turbulence generally serves to enhance vertical mixing, existing versions of KPP vary significantly in their estimates (Li et al., 2019; Chamecki et al., 2019). We tackle this question in Chapter 4 using a more complete approach than previous studies (which includes effects on nondiffusive fluxes).

The motivation behind Objective 2 is the lack of a systematic method to estimate two quantities that are needed for the implementation of KPP: $K(z)$ and $F_{ND}(z)$. In the atmospheric community the shape for $K(z)$ comes from neutral wall-bounded flows, which predict a cubic polynomial, and from assuming that such a shape also holds for convective cases. The shape for $F_{ND}(z)$ comes from assuming the same $K(z)$ shape extends to the nondiffusive term (which is done in order to

avoid counter-gradient fluxes (Zhou et al., 2018)). In the oceanic community these assumptions are further extended so that the same cubic shape is applied for both quantities in all regimes that have a combination of wave effects and convection. Although there are no arguments against this generalization, it does not necessarily need to be true. Thus we develop a method to estimate these quantities as free from *a priori* assumptions as possible in Chapter 3. Application of this method in Chapters 3 and 4 provide evidence that indeed the formulations for $K(z)$ and $F_{ND}(z)$ should change in the presence of de-stabilizing buoyancy fluxes and waves.

Objective 3 is motivated by the fact that vertical mixing is primarily performed by flow structures that are orders of magnitude smaller than the eddies responsible for large-scale horizontal transport (Chamecki et al., 2019), which makes it impossible for their effects to be modeled in large-scale coarse-resolution models. Furthermore, this large scale separation may create the misconception that small-scale eddies are not relevant for large-scale transport. This is not case and we show that vertical mixing can significantly impact large-scale horizontal transport of passive scalars in Chapter 2, which serves as an extra incentive to better represent this vertical mixing in large-scale models.

1.4 Outline

The bulk of this dissertation is composed of different papers that were either published over the course of the doctorate program or are being written at the time of the defense. The text and figures are reproduced in each chapter exactly as they appear in the journals with permission from the publishers. Because of that, each chapter corresponds to the full text of a paper and it has its own nomenclature that is consistent throughout that chapter, although not necessarily consistent with other chapters.

Chapter 2 is a paper that was published in Geophysical Research Letters (Chor et al., 2018a) in which we analyzed vertical mixing and horizontal transport of buoyant materials in oceanic regimes that span a large range of forcing combinations (tackling Objectives 1 and 3). The focus of this work was the development of a generalized framework that allows one to predict the horizontal transport of buoyant materials in any regime that is forced by a combination of surface wind stress, buoyancy fluxes and nonbreaking waves. In order to achieve that goal we introduced a velocity

scale that was applied to KPP without considering nondiffusive effects (F_{ND}) for simplicity.

In Chapter 3, published in the Journal of the Atmospheric Sciences (Chor et al., 2020b), we broadened our scope and explored KPP including the nondiffusive flux component that was neglected in the previous chapter. Although this work is performed for an atmospheric boundary layer (ABL) — being somewhat out of context in the present dissertation — we chose to include it in the main text for two reasons: (i) the ABL is dynamically similar to a waveless OSBL, with a majority of the knowledge and conclusions being interchangeable between both; and (ii) this paper introduces a method that accomplishes Objective 2 and is used as the basis for Chapter 4.

In Chapter 4, we apply the theoretical framework developed in Chor et al. (2020b) to the OSBL in order to gain insight into vertical mixing in different regimes (with a focus on wavy conditions), tackling Objective 1. Furthermore, we take advantage of the results and introduce a version of KPP for passive scalars that is optimized for passive scalar mixing in wavy situations. The main difference between our proposed model and previous ones are the shapes of $K(z)$ and $F_{ND}(z)$, which do not rely on atmospheric results as previous models did. This chapter is a preliminary version of a manuscript that will be submitted to an oceanography journal after some refining and some extra analyses are done.

We conclude the dissertation in Chapter 5, where we make an assessment of the main accomplishments of the work as a whole. Furthermore, these accomplishments are put into general context and used to discuss future directions for research.

Finally, we include an additional paper that was chronologically the first publication of the doctorate program (Chor et al., 2018b) but, since it is somewhat out of the general scope of the dissertation, it is reproduced in Appendix A. This work investigates the dispersion of buoyant materials under a pure convection regime (with buoyancy fluxes being the only forcing) with a focus on the horizontal patterns that emerge on the surface for different levels of material buoyancy.

CHAPTER 2

A turbulence velocity scale for predicting the fate of buoyant materials in the Oceanic Mixed Layer

Authors: Tomas Chor, Di Yang, Charles Meneveau and Marcelo Chamecki.

Abstract:

We introduce a general framework to predict the fate of buoyant materials in the oceanic mixed layer (OML). The framework is based on the estimation of a turbulence velocity scale for the vertical mixing of buoyant materials. By combining this velocity scale with the material's terminal rise velocity and a K-profile parameterization we are able to derive an analytical prediction for the vertical profile of material concentration that is shown to be a reasonably accurate and general representation for OML regimes driven by various levels of wind shear, Stokes drift and buoyancy flux. The analytically predicted profile allows us to estimate relevant parameters for the fate of buoyant materials, such as the depth of a plume's center of mass and the horizontal transport. We show that the predictions agree with large-eddy simulations driven by various combinations of wind shear, Stokes drift and buoyancy fluxes.

2.1 Introduction

Predicting the fate of buoyant materials in the Oceanic Mixed Layer (OML) is challenging for both numerical and theoretical studies. One issue is the very different dynamics associated with each of the main forcings in the OML (most notably wind shear, Stokes drift and buoyancy fluxes) which have distinct effects on the fate of buoyant plumes (Yang et al., 2014; Chen et al., 2016a; Taylor, 2018; Chen et al., 2018; Liang et al., 2018). This issue is aggravated by the lack of a reliable

approach to generalize results across the different regimes that arise by the combination of these forcings (Zilitinkevich, 1994). For the case of noninertial particles, whose defining parameter is their terminal rise velocity, the challenge can be traced back to the lack of a general (i.e., appropriate for several forcing conditions) turbulence velocity scale with which to analyze results. The lack of a common velocity scale makes it difficult both to combine results from individual studies (which tend to focus on a subset of the forcings), and to translate them into realistic regimes in which different forcings are acting together. For instance, Yang et al. (2014) and Yang et al. (2015) focused on the effect of Langmuir turbulence and used the Stokes drift velocity; Chor et al. (2018b) studied particle plumes under free convection and used a convective velocity scale; and Kukulka et al. (2015) and Liang et al. (2018) studied effects of Ekman and Langmuir turbulence, and used the friction velocity. These velocity scales represent very different physical processes and it is not clear how the conclusions of one study affect the others.

In this work we address this issue by defining a generalized turbulence velocity scale (W) for the vertical mixing of buoyant materials that is based only on bulk properties of the flow. Generalized expressions for a velocity scale to characterize flow dynamics under different forcing conditions have been sought in the literature, for example, by Zilitinkevich (1994) and Large et al. (1994) using Monin-Obukhov theory, and by De Bruin et al. (1994) using statistical measures of the flow. Our approach is to seek a turbulence velocity scale to characterize the mixing of buoyant materials specifically, instead of more general flow dynamics, which significantly simplifies the problem.

We demonstrate the applicability of W as an appropriate framework by deriving an analytical model to predict some key features of buoyant materials transport in the OML (Section 2.2). As will be demonstrated, the main advantage of our model is the representation of the vertical material distribution with an expression that is valid over different combinations of forcing conditions, which is possible only because of the validity of W in a wide range of cases (correct representation of vertical material distribution is crucial in order to correctly determine the transport and spreading of plumes (Chen et al., 2018; Liang et al., 2018)). We demonstrate the usefulness of the model by making comparisons with a set of numerical experiments using large-eddy simulation (LES) that span a range of forcing conditions (Sections 2.3 and 2.4).

2.2 Theory

For the purposes of this work we model the materials as noninertial buoyant particles, which is a valid approximation for a range of particulate materials in the ocean, most notably oil and microplastic marine debris (Kukulka et al., 2015; Chor et al., 2018b). For these cases we can accurately express the velocity of the particles as (Yang et al., 2016; Chor et al., 2018b)

$$\mathbf{v} = \mathbf{u} + w_r \mathbf{e}_3, \tag{2.1}$$

where $\mathbf{v}$ is the total particle velocity, $\mathbf{u}$ is the flow velocity, w_r is the material's terminal rise velocity and $\mathbf{e}_3$ is the unit vector in the direction opposite to the gravitational force. With these assumptions each material is uniquely characterized by its terminal rise velocity w_r.

2.2.1 Turbulence velocity scale

Here we seek to estimate a general turbulence velocity scale W to which w_r may be compared to in realizations of buoyant material dispersion in the OML under different forcing conditions. In order to establish a unique velocity scale, we consider the turbulent kinetic energy budget equation in steady state, neglecting horizontal gradients, turbulent transport and pressure effects:

$$0 = u_*^2 \frac{\partial \langle u \rangle}{\partial z} + u_*^2 \frac{\partial \langle u_S \rangle}{\partial z} + \langle w'b' \rangle - \varepsilon, \tag{2.2}$$

where ε is the turbulent kinetic energy (TKE) dissipation rate, u_S is the Stokes drift velocity, $u_* = \sqrt{\tau_s/\rho}$ is the friction velocity (τ_s is the surface wind stress and ρ is the seawater density), b is the buoyancy, $\langle . \rangle$ is the horizontal average operator (assumed here to approximate a Reynolds average operator) and a primed variable denotes a fluctuation with respect to the horizontal average. We can approximate each of the terms as ratios between velocity scales and length scales:

$$\varepsilon \sim \frac{W^3}{l_\varepsilon}, \qquad \frac{\partial \langle u \rangle}{\partial z} \sim \frac{u_*}{l_s}, \qquad \frac{\partial \langle u_S \rangle}{\partial z} \sim \frac{u_{S_0}}{l_L}, \qquad \langle w'b' \rangle \sim \frac{w_*^3}{l_c} \tag{2.3}$$

where $w_* = (B_0 |h|)^{1/3}$ is the Deardorff convective velocity (Kaimal et al., 1976) (h is the OML depth and B_0 is the outward buoyancy flux at the surface), and u_{S_0} is the Stokes drift velocity at the

surface. This produces

$$W^3 = u_*^3 \left(\kappa^3 + \frac{A_L^3}{La_t^2} \right) + A_c^3 w_*^3, \tag{2.4}$$

where $La_t = \sqrt{u_*/u_{S_0}}$, $A_L^3 = l_\varepsilon/l_L$ and $A_c^3 = l_\varepsilon/l_c$ are coefficients that represent, respectively, the contributions of Langmuir and convective turbulence to W, and $\kappa = 0.41$ is the Von Kármán constant (any constant of proportionality from Eq. (2.3) is absorbed into the coefficients of Eq. (2.4)).

In deriving Eq. (2.4) we also assume that $l_\varepsilon/l_s = \kappa^3$, such that in shear turbulence the relation reduces to $W = \kappa u_*$ (in agreement with the standard K-profile parameterization). We also assume that the different forcings have negligible coupling with each other. Although this assumption may not be valid at times (e.g., convection could reduce the vertical shear for a given wind stress, while turbulence generated by wind shear might disrupt convective plumes) our results seem to support this idea for the cases studied here. Finally, although there are no formal grounds to suggest that the ratios of length scales should be universal, fixing their values for the range of applications examined in this paper will be shown to produce good results (Section 2.4). With the ratios fixed, coefficients A_L and A_c can be determined by obtaining W for two separate simulations. This process will be detailed in Section 2.4, but we present the results here for completeness:

$$A_L = 0.816, \qquad A_c = 1.170, \tag{2.5}$$

which are the values used throughout the paper. Although this is similar to the approach used by Belcher et al. (2012) to estimate the TKE dissipation rate, using their fit directly in the present context produces poor results. This is mainly due to the significantly lower value of the coefficient for the wind stress when compared to other coefficients in our fit, which suggests that wind shear has a smaller influence on the vertical mixing of buoyant materials than on TKE production. Eq. (2.4) is valid as long as the buoyancy flux at the surface is not stabilizing ($B_0 \geq 0$). In cases where $B_0 < 0$ the buoyancy flux acts to decrease turbulent kinetic energy and, although there have been investigations on vertical mixing under stabilizing buoyancy fluxes (e.g. Kukulka et al. (2013) and Pearson et al. (2015)), further research is needed in order to incorporate this effect in our approach.

2.2.2 Plume predictions

In this section we use W to scale the eddy diffusivity and make analytical predictions later to be compared with numerical simulations. We start with the Eulerian conservation of particle mass for a homogeneous steady-state flow averaged in the horizontal direction with no particle flux across the surface (Kukulka et al., 2015),

$$\left\langle w'c' \right\rangle + w_r C = 0, \tag{2.6}$$

where $C(z)$ is the material concentration in steady state averaged in the horizontal direction, and c' is the fluctuation around it. We assume the turbulent flux can be represented with a K-profile parameterization (KPP) formulation (Large et al., 1994) neglecting nonlocal contributions,

$$\langle w'c' \rangle = -W\,|h|\,G(z/h)\,\frac{dC}{dz}, \tag{2.7}$$

where W is given by Eqs. (2.4)-(2.5) and $G(z/h) = (z/h)(1-z/h)^2$. In the absence of Stokes drift, the eddy diffusivity $W\,|h|\,G(z/h)$ reduces to the same form given by Large et al. (1994) for the bulk of the OML.

Following the goal of simplicity, we refrain from modifying the shape of the KPP profile to account for the different forcing conditions. Instead this information is condensed into W via its definition in Eq. (2.4). Motivated by Eqs. (2.6)-(2.7), we define the floatability parameter β as

$$\beta = \frac{w_r}{W}, \tag{2.8}$$

which measures the tendency of turbulent mixing (characterized by W) to counteract the tendency of buoyant material to float upwards (given by w_r). This is a generalization of the analogous parameter defined in Chor et al. (2018b). Depending on the value of β, the buoyant material ranges from a flow tracer ($\beta = 0$) to a surface floater ($\beta \to \infty$) (Chor et al., 2018b).

Eqs. (2.6)-(2.8) can be combined to produce (note that $h < 0$ for the OML)

$$\frac{dC}{dz} + \frac{\beta}{hG(z/h)}C = 0,$$

which can be integrated to obtain an analytical solution for $C(z)$ as (Kukulka et al., 2015)

$$C(z) = C_0 \left(\frac{1 - z/h}{z/h} \right)^{\beta} \exp\left(\frac{-\beta}{1 - z/h} \right) \qquad \text{for } h \leq z \leq z_c, \tag{2.9}$$

where C_0 is a constant used to enforce $\int_h^{z_c} C\,dz/|h - z_c| = 1$. Here, z_c is a cut-off depth that marks a point were other physical processes not considered in Eq. (2.6) become important and it should not impact results provided it is small enough. Since an accurate expression for $C(z)$ in the interval $z_c < z \leq 0$ would necessarily include these other processes, we make no attempt to describe the concentration in this range of z. Processes that could be considered when setting the value of z_c include diffusion, breaking waves, slick formation (in the case of oil), etc. Note that the relevant physical processes (and therefore the value of z_c) may depend on the choice of material to be studied.

As will be shown in Section 2.4, $C(z)$ captures the overall features of vertical mixing rather well, even though the precise shape of individual profiles may not be represented with full accuracy. Eq. (2.9) is relevant because it is a closed-form analytical solution that, as will be shown later, produces good results for a wide range of combinations of Langmuir, shear and convective turbulence (due to the wide range of validity of the floatability parameter β). Thus, predictions made using Eq. (2.9) are, in principle, valid for a wide range of realistic conditions observed in the ocean.

As a bulk measure of the vertical mixing implied by $C(z)$, we can estimate the normalized depth of the plume's center of mass $\sigma_{cm} = h^{-1} \int_h^{z_c} zC(z)\,dz / \int_h^{z_c} C(z)\,dz$ with an approximated expression as:

$$\sigma_{\mathrm{cm}} \approx \begin{cases} \frac{1}{2} \frac{2\sin(\pi\beta) + 5\pi\beta(\beta - 1)}{2\sin(\pi\beta) - 5\pi\beta} & 0 \leq \beta < 1 \\ 0 & \beta \geq 1, \end{cases} \tag{2.10}$$

which will be used throughout this work. A detailed derivation of Eq. (2.10) from Eq. (2.9) can be found in the Support Information, text S1.

One of the main large-scale consequences directly controlled by the vertical distribution of material is the horizontal transport. A plume's center of mass with average vertical distribution $C(z)$

is horizontally advected with a velocity $\mathbf{U}_h$ that can be approximated by

$$\mathbf{U}_h = \frac{1}{|h - z_c|} \int_h^{z_c} C_0 \langle \mathbf{u}_h \rangle \left(\frac{1 - z/h}{z/h} \right)^{\beta} \exp\left(\frac{-\beta}{1 - z/h} \right) dz, \tag{2.11}$$

which neglects horizontal transport by turbulence. Here, $\mathbf{u}_h$ is the total horizontal flow velocity (including the Stokes drift). From Eq. (2.11) we have that for flow tracers $\mathbf{U}_h$ is analogous to the Ekman transport, while for surface floaters the center of mass moves following the flow velocity at the surface, as observed in the simulations of Chen et al. (2018).

2.3 Numerical set-up

We use a LES model to investigate the analytical predictions in Section 2.2. The model was already extensively described and used in several other investigations (Yang et al., 2014; Yang et al., 2016; Chor et al., 2018b). Detailed information on the LES model and the simulation setup can be found in text S2 of the Support Information (Craik et al., 1976; Smagorinsky, 1963; Lilly, 1967; Bou-Zeid et al., 2005; McWilliams et al., 1999; Chamecki et al., 2008; Donelan et al., 1987; McWilliams et al., 1997).

All simulations presented here have a value for the Coriolis frequency of $f = 7 \times 10^{-5}\,\mathrm{s}^{-1}$ and used a total of eight different cases of buoyant materials (modelled as sets of particles) characterized by rise velocities $w_r = 0$, 2.0×10^{-4}, 8.5×10^{-4}, 3.5×10^{-3}, 7.5×10^{-3}, 1.5×10^{-2}, 3.0×10^{-2} and 5.5×10^{-2} m/s (these correspond to a passive tracer and oil droplets rising in water of diameters between 0.05 mm to 1.5 mm (Zheng et al., 2000), and also fall in the range of observed values for microplastic (Kukulka et al., 2016)). Five simulations were run using a 400 m horizontal and 120 m vertical domain length (which we name $S_1, S_2, ..., S_5$) and the relevant parameters are given in Table 2.1. Thus, as can be seen in Table 2.1, the simulations span a wide range of conditions dominated by different forcings. It is worth mentioning that simulation S_4 is configured to match the peak of the joint probability density function of the Stokes drift, wind shear and surface buoyancy flux according to Belcher et al. (2012), thus being the most representative case we can run with our LES model.

Figure 2.1 shows snapshots of material concentrations from three of the simulations in which

Table 2.1: Parameters for the simulations used in this paper. DP87 and MS97 indicate that the Stokes drift was calculated according to the spectra in Donelan et al. (1987) and as in McWilliams et al. (1997), respectively. U_{10} is the wind velocity at 10 meters corresponding to u_*. All simulations have a vertical resolution of $\Delta z = 0.5\,\mathrm{m}$.

Sim.	u_* (m/s)	U_{10}(m/s)	w_* (m/s)	La_t	W (m/s)	h (m)	Domain type	$\Delta z/\lvert h\rvert$	Short description of forcings
S_1	0.01	8.1	0	0.3 (DP87)	0.021	-69.8	Periodic	7.2×10^{-3}	Wind stress + Stokes drift
S_2	0	0	0.019	–	0.022	-82.3	Periodic	6.0×10^{-3}	Buoyancy flux
S_3	0.01	8.1	0	∞	0.004	-69.3	Periodic	7.2×10^{-3}	Wind stress
S_4	0.007	5.9	0.009	0.3 (DP87)	0.016	-58.3	Periodic	8.6×10^{-3}	Wind stress + Stokes drift + Buoyancy flux (in a typical combination for the ocean)
S_5	0.007	5.9	0.009	0.5 (MS97)	0.013	-55.2	Periodic	9.0×10^{-3}	Wind stress + Stokes drift + Buoyancy flux (Stokes drift decoupled from the wind)
E_3	0.01	8.1	0	∞	0.004	-69.3	ENDLESS	7.2×10^{-3}	Same as S_3
E_4	0.007	5.9	0.009	0.3 (DP87)	0.016	-58.3	ENDLESS	8.6×10^{-3}	Same as S_4

the distinct dynamics become clear: S_2 (left panels) is dominated by convective plumes, S_3 (middle panels) is more uniformly mixed only by the surface shear and S_4 (right panels) is dominated by Langmuir turbulence.

We have also run two extra simulations that are identical to simulations S_3 and S_4 except for the boundary conditions for the buoyant materials (which we denote E_3 and E_4). While in simulations S_n the particles recirculate in a closed periodic domain until they are horizontally homogeneous, in simulations E_n we use the ENDLESS approach (Chen et al., 2016a; Chen et al., 2018), which allows us to simulate plumes that are much larger than the flow domain. This is done by simulating the turbulent flow on an affordably small horizontal domain with periodic boundary conditions. The velocity field is then replicated periodically to cover much larger scales while it advects the buoyant material. Thus, with the ENDLESS approach a finite-sized plume can be realistically modeled, which allows us to accurately quantify the long-range horizontal transport.

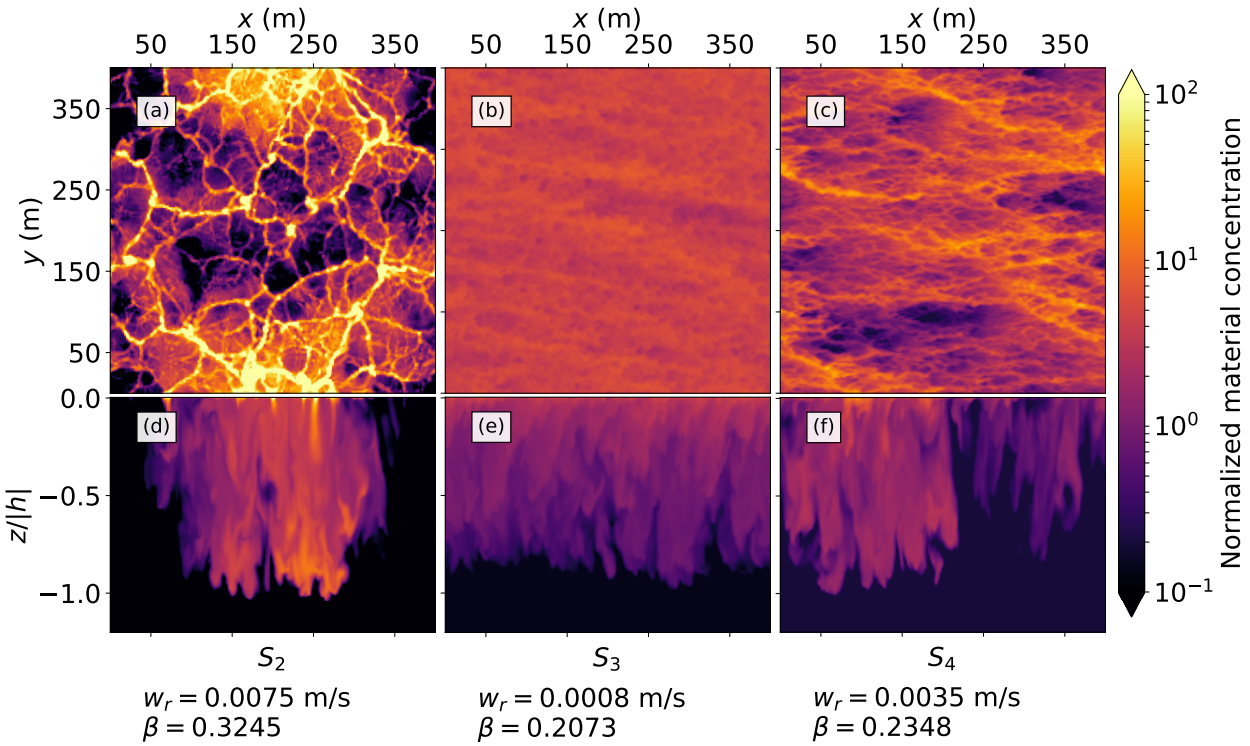

Figure 2.1: Instantaneous snapshots of concentration in simulations S_2, S_3 and S_4 (left, middle and right panels, respectively). Top panels show the surface concentration and bottom panels show the concentration in a vertical plane. Concentrations are normalized by their averages in the OML. Horizontally averaged profiles for these cases are shown in Figure 2.2c.

2.4 Results

2.4.1 Vertical mixing

We first consider the determination of the coefficients of Eq. (2.4). The first step was to calculate the center of mass σ_{cm} for each different set of materials for simulations S_1 and S_2 only. Using these results we fitted two optimal values of W (one for each simulation) against the analytical prediction given by Eq. (2.10). With two equations and two unknowns (from Eq. (2.4)) we were able to determine the coefficients A_L and A_c. The results were already given in Eq. (2.5) and we can see how they collapse estimates for σ_{cm} in Figure 2.2d. The fit was performed only for σ_{cm} in S_1 and S_2, and all other results follow with no further fitting.

It is clear from the organization of the points in Figure 2.2d that β is able to properly collapse the results for σ_{cm}. Results from simulation S_2 somewhat deviate from others, which is caused by the distinct dynamics between convective turbulence (dominant mechanism in S_2) and shear turbulence (dominant mechanism in the other simulations). Note that in Figure 2.2d the values for the coefficients A_L and A_c (and subsequently the values for β) are used to scale the x-axis only, while the y-axis is simply calculated from the LES results. The theoretical prediction given by Eq. (2.10) is also plotted in the figure and shows good agreement with the measured points. Note in particular the validity of the prediction that the buoyant material is almost exclusively present at the surface (thus, $\sigma_{cm} \to 0$) for $\beta > 1$.

Figures 2.2a-c show the results for groups of horizontally averaged material concentration profiles with similar floatability contained within the circles in Figure 2.2d (following the same color-coding). It is clear that there are differences among the profiles within a group due to distinct turbulence dynamics. In order to predict individual curves accurately, nontrivial changes to the parameterization of the turbulent mass flux would be needed. However, even though the precise shapes of the profiles differ, the differences between profiles on distinct beta groups is much larger than those caused by different turbulent regimes within the same beta group (and thus with similar values of β). This explains the good agreement of Figure 2.2d.

Analytical profiles calculated with Eq. (2.9) for the average β value in each group are also

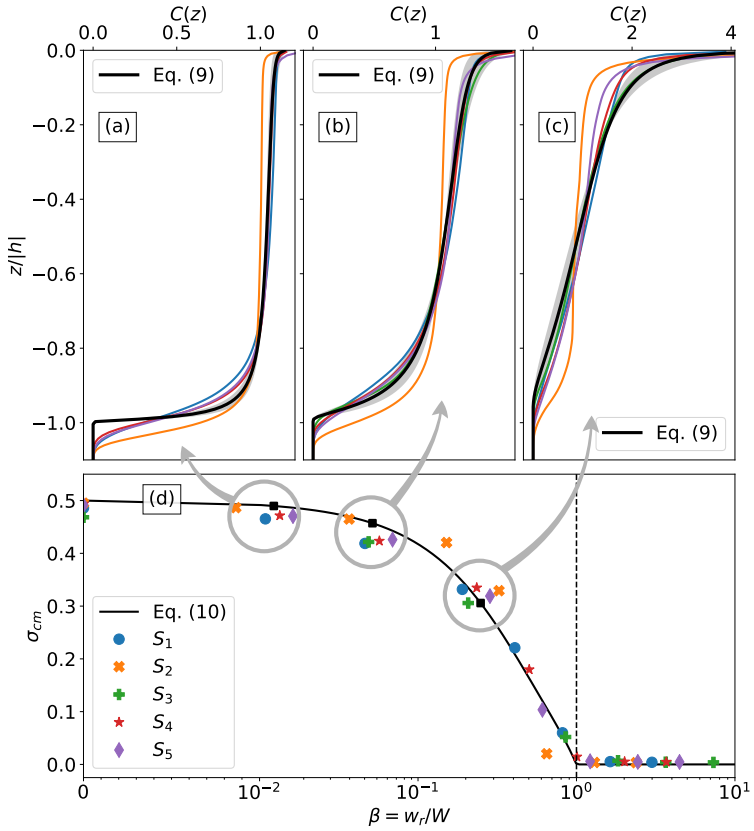

Figure 2.2: Panels a, b and c: Vertical profiles of horizontally averaged material concentrations for cases contained within grey circles in panel d as colored lines along with the analytical predictions $C(z)$ (Eq. (2.9); black lines). The shaded grey area in these panels corresponds to the area defined by the predicted profile (Eq. (2.9)) using the minimum and the maximum values of β from the simulated cases for each panel. Panel d: Analytical prediction for the normalized center of mass (Eq. (2.10); black line) along with measured results from simulations (colored points). The leftmost part of panel d uses a linear scale, while the rest uses a logarithmic scale for the horizontal axis.

plotted in Figures 2.2a-c, respectively, as solid black lines for comparison (and indicated in Figure 2.2d as black squares). It is clear that $C(z)$ agrees with LES results within the variations seen in the simulations themselves. This means that the analytical solution given by Eq. (2.9), which only requires knowledge of β, yields a good first approximation to the vertical distribution of material over broad ranges of oceanic conditions. It is a significant achievement that a simple theory can collapse results for simulations with such different dynamics as can be seen in Figure 2.1.

2.4.2 Horizontal advection

We proceed to use simulations E_3 and E_4 to assess predictions for the horizontal velocity of the

center of mass $\mathbf{U}_h$ which are presented in Figure 2.3. Notice that the limit $\beta \to 0$ in Figure 2.3 corresponds to a nonbuoyant tracer (which is predicted to move with the vertical average of $\langle \mathbf{u}_h \rangle$ over the complete depth of the OML; *vide* Eq. (2.11)), while the limit $\beta \to \infty$ corresponds to a surface floater (which is predicted to be advected purely by the horizontal flow at the surface of the OML). Note also that for all cases considered in this work, the resolution of the data for $\langle \mathbf{u}_h \rangle$ was coarser than any appropriate choice for the cut-off scale z_c. Therefore, when calculating $\mathbf{U}_h$ from Eq. (2.11), the topmost data point for $\langle \mathbf{u}_h \rangle$ set the upper limit of integration.

Results obtained by following the center of mass from simulations are plotted as points in Figures 2.3a-b for simulation E_3 and in Figures 2.3c-d for simulation E_4. Results obtained using Eq. (2.11) with the horizontal mean velocity $\langle \mathbf{u}_h \rangle$ from the LES are plotted as dashed lines in the same panels. There is overall good agreement between the predicted and measured transport velocities for both simulations. The fact that the shape of the curve is being well-captured in both cases is a result of the profile given by Eq. (2.9) being successful in capturing the vertical mixing.

Notably, the estimate for $\mathbf{U}_h$ obtained using Eq. (2.11) with the LES velocity profile $\langle \mathbf{u}_h \rangle$ slightly underestimates the transport for $\beta > 0.3$ (thus, highly buoyant materials tend to move faster than the mean horizontal velocity of the surface flow). This is due to the fact that strongly buoyant materials tend to concentrate in regions of horizontal convergence at the surface (Chor et al., 2018b). The results presented here indicate that these regions have faster-moving flow; a feature that has already been reported for Langmuir turbulence (Thorpe, 2004). Our results indicate that this effect is also true for wind-driven OMLs without Langmuir circulations. This effect on the horizontal transport cannot be predicted by Eq. (2.11) or any scheme that neglects horizontal turbulent transport and deserves future investigation.

For a completely predictive simple model, we evaluate $\boldsymbol{U}_h$ without needing to use LES to determine the profiles of $\langle \boldsymbol{u}_h \rangle$. For this purpose we determine the mean velocity from a one-dimensional model

$$\begin{aligned} f\mathbf{e}_3 \times \langle \mathbf{u}_h \rangle &= \frac{d}{dz}\left(\nu_e \frac{d\langle \mathbf{u}_h \rangle}{dz} \right), \\ \nu_e(z) &= \kappa u_* |h| \, G(z/h), \end{aligned} \tag{2.12}$$

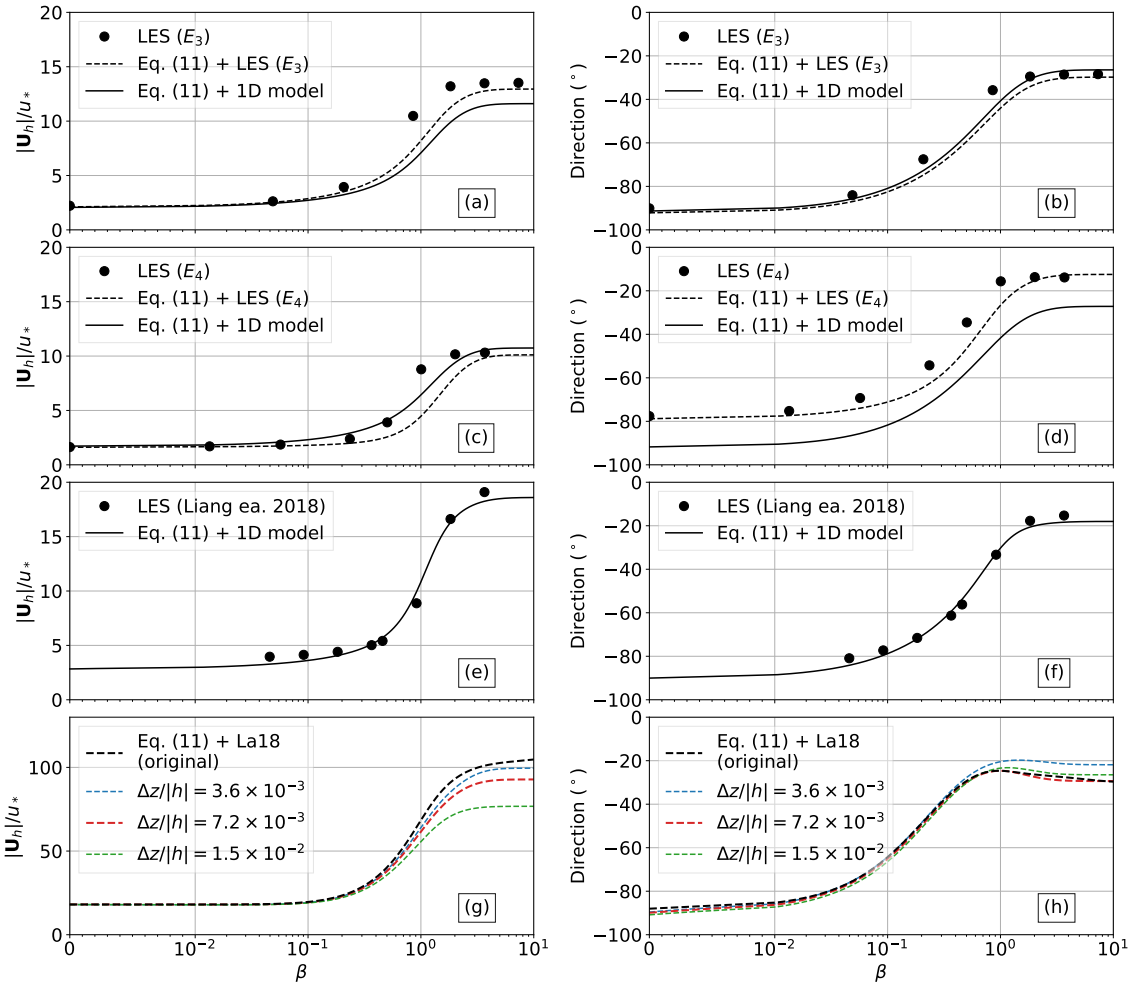

Figure 2.3: Measured and predicted results for the center of mass horizontal velocity $\mathbf{U}_h$. Left panels show the magnitude and right panels show the direction of $\mathbf{U}_h$. Panels (a) and (b): simulation E_1. Panels (c) and (d): simulation E_4. Panels (e) and (f): results from the simulation performed by Liang et al. (2018). Panels (g) and (h): results from the measurements given in Laxague et al. (2018) (denoted as La18). In all panels the points are results obtained only with LES, dashed lines results are obtained with Eq. (2.11) and the averaged velocity from the simulations (a-d) or field measurements (g-h), and solid lines are obtained with Eq. (2.11) using velocities from the 1D model in Eq. (2.12). The colored dashed lines in panels g-h represent different coarse-grainings of the original high-resolution data (Δz is the vertical resolution).

which is integrated numerically. In this model we do not use any information from the LES results (other than the depth of the mixed layer h) or from the material properties and floatability parameter β. Although we calculate the velocities with a sufficiently fine grid for grid-convergence, we perform the integration in Eq. (2.11) using only the vertical grid points used by the LES to avoid mismatches due to different resolution of the quadrature. Results for this approach are plotted in

Figures 2.3a-d as solid lines. Once again there is reasonable agreement for both magnitude and direction. Estimates with the 1D model tend to differ from simulations more than using $\langle \mathbf{u}_h \rangle$ from the LES model, which is expected since the 1D model given by Eq. (2.12) ignores changes in the mean velocity from the different forcing conditions. Nonetheless, it is possible for the 1D model to have better agreement than the LES-based model in some cases (e.g. in Figure 2.3c). We conclude that Eq. (2.11) along with the 1D model in Eq. (2.12) are sufficient to reasonably predict the LES results for $\boldsymbol{U}_h$ with virtually no information from the simulations. Modifying the 1D model used here (for example by modifying ν_e to account for Langmuir circulations and convection effects) can improve results for flow prediction and potentially improve the estimation of $\mathbf{U}_h$ (Large et al., 1994; McWilliams et al., 2000; Smyth et al., 2002).

We proceed to compare our 1D model from Eq. (2.12) with the results presented by Liang et al. (2018) for the Langmuir-dominated case, shown in Figures 2.3e-f (information on this data can be found in text S3 of the Supporting Information). This case is similar to our simulation S_1, but with a considerably different steady-state mixed layer depth of approximately 40 meters. Again, there is good agreement with the 1D model, with both the direction and magnitude being well captured.

Recently, Laxague et al. (2018) presented field observations that show large shear close to the surface, suggesting that numerical models must have very fine resolution to capture the correct transport direction of buoyant materials. Testing this hypothesis by simulating the conditions in which their measurements were obtained is beyond the scope of this work. However, we use their data along with our analytical predictions to assess the resolution of our simulations and the ability of LES in general to capture the transport of materials over a wide range of β. (Information about the data can be found in text S4 of the Supporting Information.)

Results for $\boldsymbol{U}_h$ calculated using $\langle \boldsymbol{u}_h \rangle$ from the original data by Laxague et al. (2018) and Eq. (2.11) are shown in Figure 2.3g-h as black dashed lines. The red dashed lines show results for the same data coarse-grained to match the median of the vertical resolutions used in our LES experiments ($\Delta z/|h| \approx 7.2 \times 10^{-3}$, see Table 2.1). Blue and green dashed lines show the same results for half and double this resolution, respectively. Figure 2.3g-h shows that with our current resolution (dashed red lines) we are able to capture changes in $\boldsymbol{U}_h$ as a function of β. In the worst case, which is the limit $\beta \gg 1$, we underestimate $\boldsymbol{U}_h$ by $\approx 12\%$ (due to the underestimation of

$\langle \boldsymbol{u}_h \rangle$). The effects on the direction are less straightforward due to the variance of the velocity close to the surface exhibited by the observations, however, the error is always less than 10°. Overall, our analysis suggests that the vertical resolutions used in the simulations in this paper (corresponding to approximately 143 points in the OML) produce reasonable results, which adds more confidence to our simulation results.

2.5 Conclusions

We have introduced a generalized turbulence velocity scale W, which we used to define the floatability parameter β, leading to a simple analytical expression for the averaged vertical material concentration profile valid for a range of forcing conditions (Eq. (2.9)). Based on this expression, we derived predictions for the depth and horizontal advection velocity of a plume's center of mass with respect to β, which were then compared with LES results for a range of different oceanic regimes.

We showed that Eq. (2.9) is able to reproduce observed behaviors and represent the most important features of the phenomena investigated, and in this sense there was good agreement with the simulations. We also showed that a one-dimensional model for estimating the velocity yields reasonable results for the horizontal transport, allowing our analytical approach to be completely predictive. These results are particularly useful in the context of oil spills, where there is a large level of uncertainty concerning the application of chemical dispersants in the plume (Chen et al., 2018) and simple models such as the one presented here may be helpful. Furthermore, we obtained predictions for plume transport using field measurements of horizontal velocity from Laxague et al. (2018) which illustrate the impact of vertical resolution on the estimation of plume fate.

The framework presented here can also be used to determine other quantities of interest such as the horizontal effective diffusivity due to vertical shear, whose theoretical formulation was already demonstrated by Liang et al. (2018). With our framework it can be shown that the horizontal effective diffusivity scales with an inverse dependence on the solute's diffusivity as originally reported by Taylor (1953), and its calculation can be made applicable to general forcing conditions (details in text S5 of the Supporting Information (Taylor, 1953; Esler et al., 2017)).

In summary, Eqs. (2.4)-(2.5) and (2.8)-(2.11) can be used to make predictions of mean transport speed, direction, and horizontal diffusion of buoyant plumes without the need of performing simulations with buoyant materials. Although it is preferred to have horizontal velocities from regional models or measurements for better results, reasonable estimates can still be obtained by using the 1D model given in Eq. (2.12) if high resolution velocity data is not available.

CHAPTER 3

Diffusive-nondiffusive flux decompositions in atmospheric boundary layers

Authors: Tomas Chor, James C. McWilliams and Marcelo Chamecki

Abstract:

Eddy diffusivity models are a common method to parameterize turbulent fluxes in the atmospheric sciences community. However, their inability to handle convective boundary layers leads to the addition of a nondiffusive flux component (usually called nonlocal) alongside the original diffusive term (usually called local). Both components are often modeled for convective conditions based on the shape of the eddy diffusivity profile for neutral conditions. This assumption of shape is traditionally employed due to the difficulty of estimating both components based on numerically-simulated turbulent fluxes without any *a priori* assumptions. In this manuscript we propose a novel method to avoid this issue and estimate both components from numerical simulations without having to assume any *a priori* shape or scaling for either. Our approach is based on optimizing results from a modeling perspective and taking as much advantage as possible from the diffusive term, thus maximizing the eddy diffusivity. We use our method to diagnostically investigate four different large-eddy simulations spanning different stability regimes, which reveal that nondiffusive fluxes are important even when trying to minimize them. Furthermore, the calculated profiles for both diffusive and nondiffusive fluxes suggest that their shapes change with stability, which is an effect that is not included in most models currently in use. Finally, we use our results to discuss modeling approaches and identify opportunities for improving current models.

3.1 Introduction

In the atmospheric sciences community, eddy diffusivity models have been invaluable when representing turbulent fluxes (Ghannam et al., 2017). The premise in these models is that the action of eddies can be parameterized as a diffusive process via a flow-dependent eddy diffusivity. This approach (hereafter referred to as gradient transport models (GTM) but also known as K-theory (Stull, 1988)) can be written as

$$\left\langle w'c' \right\rangle = -K(z)\frac{\partial \langle C \rangle}{\partial z}, \tag{3.1}$$

where C is the concentration of a passive tracer, $K(z)$ is the eddy diffusivity of the flow, and the brackets denote an average over homogeneous dimensions.

In order to justify GTMs from a theoretical perpective, it is necessary that the eddies be smaller than some characteristic length scale over which the mean gradient of the transported quantity profiles do not change appreciably (Corrsin, 1975). Thus, Equation (3.1) can be formally justified for neutral atmospheric boundary layers (ABLs), where the eddies are relatively small (Moeng et al., 1994; Stull, 1988), but should not be expected to hold for convective ABLs which have large convective plumes (also called thermals (Hunt et al., 1988; Williams et al., 1993)). If we calculate the eddy-diffusivity K from observations of turbulent fluxes and mean gradient profiles in convective ABLs via Equation (3.1), two undesired effects indicate that pure GTMs are not suited for convective conditions:

1. The presence of heights with zero mean tracer gradient and nonzero turbulent flux, implying $K \to \infty$; and

2. The presence of heights where the turbulent flux and the mean gradient have the same sign, implying $K < 0$.

Both of these effects are unphysical considering the initial premise of GTMs that $K(z)$ is akin to a diffusivity, and are linked to the presence of large convective plumes that can produce transport both with zero gradient and against the mean local gradient (counter-gradient transport) (Zhou et al., 2018). We refer to the appearence of these unphysical effects in pure GTMs applied to convective ABLs as GTM failure.

Wyngaard et al. (1984) (hereafter WB84) analyzed this issue and showed that GTM failure is a consequence of trying to parameterize the highly asymmetric vertical transport in convective ABLs using only one diffusive term. There are many examples of attempts to overcome this issue (Hamba, 1993; Stull, 1993; Fiedler, 1984; Wyngaard et al., 1991; Dop et al., 2001), but in this manuscript we focus on the approach usually attributed to Deardorff (1966) (hereafter D66), which consists of adding an extra term F_{ND} to Equation (3.1) which does not depend on local properties of the flow:

$$\left\langle w'c' \right\rangle = \underbrace{-K(z)\frac{\partial \langle C \rangle}{\partial z}}_{F_D(z)} + F_{ND}(z), \tag{3.2}$$

which is general enough to work in convective (where $F_{ND}(z) \neq 0$) and neutral or stable conditions (where one would expect $F_{ND}(z) \approx 0$). In D66's original work F_{ND} is assumed to have the same shape as $K(z)$ (see Equation (3.9)), but we relax this assumption here. This model introduces a conceptual separation of the flux into two components: a diffusive component $F_D = -K\partial \langle C \rangle / \partial z$, which is conceptually tied to the small eddies of the flow, and a nondiffusive component F_{ND}, which is conceptually tied to the action of large eddies (in this case, large convective plumes). This decomposition has been widely accepted by the community and it is used in many different forms, mostly distinct by their formulations for K and F_{ND} (Deardorff, 1966; Holtslag et al., 1991; Siebesma et al., 2007; Ghannam et al., 2017). It should be noted that in most uses of D66's approach, the goal was parameterizing heat fluxes, but they are used here for examining passive tracers.

The main issue with Equation (3.2) is that the addition of another unknown without an extra equation produces an under-determined system and prevents us from directly estimating $K(z)$ and $F_{ND}(z)$ from measured quantities. Since there is no well-defined scale separation between "large" and "small" eddies in ABL flows, any diffusive/nondiffusive decomposition is bound to be artificial. Two workarounds are usually employed. One of them is to introduce an extra prognostic equation for the turbulent fluxes and, after several approximations, reach a separation of the fluxes into diffusive and nondiffusive components which can be used to infer $K(z)$ and $F_{ND}(z)$ (e.g. Holtslag et al. (1991) and Ghannam et al. (2017) for temperature). The second workaround is to assume *a priori* shapes and/or scalings for both components (Troen et al., 1986). We refrain from using both approaches here in order to avoid constraining our results.

To that end we introduce an optimization-based method that is capable of estimating profiles for F_D and F_{ND} without any imposed shape or scaling. Our focus lies on the diagnostic study of transport of passive tracers, although a brief analysis for temperature is included at the end. The case of momentum has extra complications (due to $K(z)$ being a tensor) which are beyond the scope of the present work. Our method works in any ABL regime (stable, neutral and unstable) and it only requires that two separate tracers with different sources into the interior be present. We apply our method to four large eddy simulations (LESs) that range from weakly stable to strongly unstable and show that it captures general features that are expected from our understanding on ABL dynamics and modeling. Our results are then analyzed in reference to currently-used models and used to discuss model development practices.

3.2 Theoretical aspects and definitions

Throughout this work, we use the word "separation" rather loosely to indicate a conceptual partition of the total turbulent flux into different terms, each tied to a different physical process, which can then be separately modeled. Conversely, we use the word "decomposition" in a mathematical sense, where an observed total flux is exactly decomposed into different terms that, by definition, exactly add up to the original flux.

A brief discussion on nomenclature practices is useful here. The first and second terms on the right-hand side of Equation (3.2) are usually referred to as local and nonlocal terms. This is a reference to both the modeling of these terms (which depend on local and nonlocal flow quantities) and their intent to represent fluxes due to "local" and "nonlocal" processes (interpreted here as small eddies that remain localized in space and all remaining eddies, respectively; Moeng et al. (1994)). However, it is up for debate whether F_D and F_{ND} actually represent the turbulent vertical fluxes due to local and nonlocal processes (Zhou et al., 2018). Thus, this nomenclature is somewhat misleading since it blurs the line between the physical processes themselves and our attempt to parameterize them, while erroneously implying that a clear separation between both physical processes exist. Therefore we use the names diffusive and nondiffusive fluxes for F_D and F_{ND}, which focuses on their mathematical form.

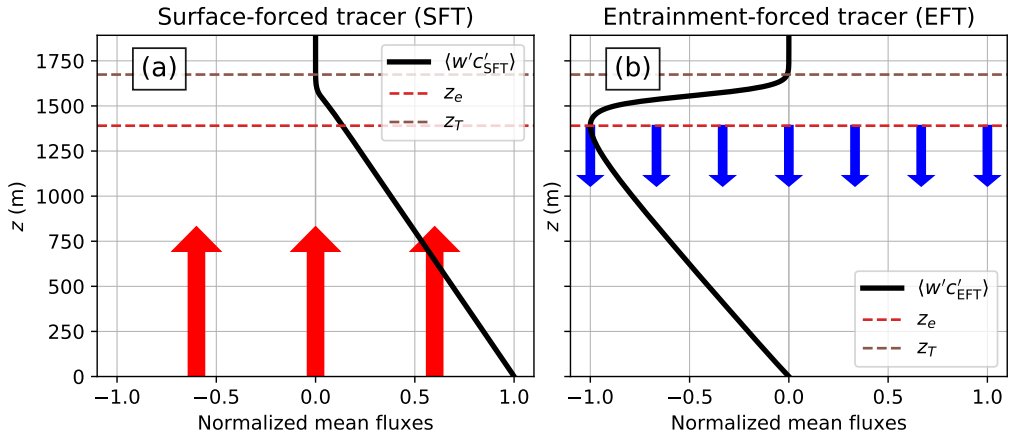

Figure 3.1: Mean turbulent flux profiles for a SFT (a) and an EFT (b). The data for this plot is taken from simulation Plumes, to be described in Section 3.3. Both fluxes are normalized so that the maximum magnitude of the fluxes is unity. Sketched in the figure are also arrows for transport via coherent convective plumes (red arrows) and entrainment processes (blue arrows), and the maximum-entrainment height z_e and entrainment layer top z_T.

3.2.1 Surface-forced and entrainment-forced transport

The concept of surface-forced versus entrainment-forced transport was first introduced by WB84, who noticed that tracer transport from the bottom up was more effective than from the top down in a convective ABL, with the source of asymmetry being the presence of organized coherent plumes emerging from the surface. Throughout our paper we refrain from using the terminology top-down and bottom-up (which is WB84's nomenclature) in favor of using the more general terms surface-forced and entrainment-forced tracers (SFT and EFT, respectively). We thus define a SFT as a tracer which has a source at the surface and no other sources/sinks in the domain. We denote its concentration with C_{SFT} and the subscript SFT is used throughout the paper to indicate quantities associated with this tracer. Figure 3.1a shows the normalized mean turbulent flux profile for a SFT in a convective regime as a solid black line (the simulation used for this plot will be detailed in Section 3.3). SFTs are effectively transported in convective ABLs since their main transport mechanism is advection by coherent motions due to large convective plumes (Kaimal et al., 1976; Moeng et al., 1994), which is sketched in Fig. 3.1a as red arrows.

An EFT, on the other hand, is defined as a tracer whose flux into the ABL is performed solely by entrainment processes; a mechanism that is sketched in Fig. 3.1b as blue arrows. In practice this flux

occurs due to a change in concentration across the entrainment layer. Figure 3.1b also shows the mean turbulent flux profile for an EFT as a solid black line. Concentrations for EFTs are denoted as C_{EFT} and the subscript EFT is used throughout the manuscript to identify quantities associated with it. We use EFTs to define the maximum entrainment depth z_e and the top of the entrainment layer z_T. z_e is the height at which the turbulent flux of an EFT is at its minimum (as can be seen by the red dashed line in Fig. 3.1). z_T is the height at which the mean turbulent flux of an EFT goes to roughly zero (excluding the surface) and can be seen in Fig. 3.1 as a dashed brown line.

It should also be noted that SFTs and EFTs span most passive tracers of interest. While passive tracers with surface sources are represented by SFTs and passive tracers with entrainment sources are represented by EFTs, passive tracers with sources in both boundaries are linear combinations of both. The exceptions that cannot be represented by these two cases are tracers with sources/sinks in the interior of the ABL.

3.2.2 Flux decompositions and models

Equations (3.1) and (3.2) are two different flux separations on which most models are based. We proceed with a brief description of some models of interest to this research and their approaches to partitioning fluxes. The reader is directed to Dop et al. (2001) and Ghannam et al. (2017) for more information on the models.

3.2.2.1 Fully diffusive

Fully diffusive separations are pure GTMs and follow Equation (3.1). In the case of fully diffusive decompositions, the total turbulent flux is treated as one diffusive process only and the result is trivial: $F_{ND} = 0$ and $F_D = \langle w'c' \rangle$.

An early example of a fully diffusive model is given by Prandtl (1942), who estimated the eddy diffusivity with a mixing length approach. Another example is the one by WB84, where the asymmetry of the flow (transport from the top-down versus bottom-up) is understood as two separate diffusive processes that act alongside each other. Thus in WB84's model the total eddy-diffusivity $K(z)$ depends on the bottom-up diffusivity K_{SFT}, associated with convective plumes, and on the

top-down diffusivity K_{EFT}, associated entrainment processes. Since transport via convective plumes is more efficient than via small eddies, $K_{\mathrm{SFT}} > K_{\mathrm{EFT}}$ for most of any convective ABL. Their method can be written as

$$K_{\mathrm{SFT}}(z) = -\frac{\left\langle w'c'_{\mathrm{SFT}}\right\rangle}{\partial\langle C_{\mathrm{SFT}}\rangle/\partial z}, \tag{3.3}$$

$$K_{\mathrm{EFT}}(z) = -\frac{\left\langle w'c'_{\mathrm{EFT}}\right\rangle}{\partial\langle C_{\mathrm{EFT}}\rangle/\partial z}, \tag{3.4}$$

$$K_i(z) = \frac{K_{\mathrm{SFT}}K_{\mathrm{EFT}}\left(\left\langle w'c'_i\right\rangle_s(1-z/z_e) + \left\langle w'c'_i\right\rangle_e z/z_e\right)}{K_{\mathrm{EFT}}\left\langle w'c'_i\right\rangle_s(1-z/z_e) + K_{\mathrm{SFT}}\left\langle w'c'_i\right\rangle_e z/z_e}, \tag{3.5}$$

where $\left\langle w'c'_i\right\rangle_s$ and $\left\langle w'c'_i\right\rangle_e$ are the tracer's turbulent flux at the surface and at the entrainment layer, respectively, and the subscript i differentiates between tracers. Although conceptually useful, WB84's model is of limited practical applicability due to GTM failure and because $K_i(z)$ depends on the ratio $\left\langle w'c'_i\right\rangle_e / \left\langle w'c'_i\right\rangle_s$ for specific tracers (thus it is no longer a property of the flow alone).

3.2.2.2 One diffusive and one nondiffusive component

This case follows Equation (3.2) and F_{ND} is a single term that can be estimated in various ways (see Holtslag et al. (1991) and Ghannam et al. (2017)), resulting in a two-term flux partition. Troen et al. (1986) (hereafter TM86) popularized it with their model, which can be written as

$$K(z) = u_s(z)\,h\,G(z/h), \tag{3.6}$$

$$u_s(z) = \frac{\kappa u_*}{\phi(z/L_o)}, \tag{3.7}$$

$$G(z/h) = \frac{z}{h}\left(1-\frac{z}{h}\right)^2, \tag{3.8}$$

$$F_{ND} = C_*\,G(z/h)\left\langle w'c'\right\rangle_s, \tag{3.9}$$

where $\kappa = 0.4$ is the von Kármán constant, C_* is a constant, ϕ is the nondimensional gradient for a tracer in the surface layer, G is a cubic shape function, h is the ABL height, and the velocity scale u_s is capped at its value at $z/h = 0.1$ for unstable conditions.

One other approach to model F_{ND} is the eddy-diffusivity-mass-flux (EDMF) method, whose premise is to explicitly separate the flux due to narrow convective plumes and the rest of the flow

(generally referred to as the environment). The governing equations for this method follow naturally from the updraft-environment separation and, after assuming that updrafts are arbitrarily narrow (Siebesma et al., 2007), the nondiffusive flux becomes

$$F_{ND} = M\left(\langle C\rangle_u - \langle C\rangle\right), \tag{3.10}$$

where M is the vertical mass flux and $\langle C\rangle_u$ is the average concentration of a tracer inside updrafts. In order to model the total turbulent flux, F_{ND} is then combined with a parameterization for $K(z)$ similar to Equation (3.6). It is worth noting that this approach is designed to work well in strongly convective conditions (Siebesma et al., 2007; Witek et al., 2011).

Although estimating the terms of a fully-diffusive decomposition is trivial, doing the same for a two-term decomposition is challenging due to the resulting under-determined system of equations. One example that relies on fitting eddy diffusivities in a plume of passive scalars has been used in the oceanic sciences community (Chen et al., 2016a) and a different approach is introduced in the present work. It is worth noting that approaches to decompose the total flux exist, but all of them focus on separating it into components due to local and nonlocal processes without assuming a diffusive/nondiffusive separation. These approaches are built with convective conditions in mind and rely on some type of conditional sampling of the instantaneous velocity fields (see Zhou et al. (2018) and references therein, and Chinita et al. (2018)).

3.2.3 Criteria for separation

In this section we discuss a set of criteria that are in accordance with what is currently known about the dynamics and modeling of ABLs. These criteria are desired of both decompositions and models based on them, and should be observed by both SFTs and EFTs. It is important to emphasize that there exist many decompositions that satisfy these criteria, and these are merely reality-checks that are necessary but not sufficient for a decomposition to be considered successful. With that in mind, we proceed to list the criteria and discuss them:

1. $K(z)$ should be only a property of the flow and independent of the tracer;

2. $K(z)$ should be a finite non-negative quantity everywhere;

3. $K(z)$ should follow Monin-Obukhov similarity theory (hereafter MO similarity theory) within the surface layer for tracers whose main flux into the ABL happens through the surface.

Although criterion 1 may appear to always be true for passive tracers, this can only be theoretically justified under specific conditions. Let us define a length scale l^c as the distance over which the mean gradient $\partial \langle C \rangle / \partial z$ remains relatively constant (Corrsin, 1975). Note that l^c may be different for different tracers. Let us also loosely define the integral scale of the flow (l^I) as the size of the largest eddies. Since only the effect of eddies smaller than l^c can be theoretically included in $K(z)$, then criterion 1 should only be true when $l^I < l^c$ (Corrsin, 1975) and a tracer-independent $K(z)$ should be viewed as an approximation for all other cases. In practice, however, this approximation seems to be valid since tracer-independent eddy diffusivities have been used for decades (although often there is the introduction of Prandtl and Schmidt numbers (Elliott et al., 2011; Li, 2019)) and have been shown to produce reasonable results. We thus include criterion 1 mostly based on modeling purposes.

Criterion 2 prevents GTM failure and ensures that there is integrated variance reduction for any transported scalar. Criterion 3 is based on empirical observations that, when the necessary assumptions are satisfied, MO similarity theory appears to hold well. This condition is built into all eddy-diffusivity parameterizations that assume an *a priori* shape for K (e.g., Troen et al. (1986), Holtslag et al. (1991)), but may not be true if K is calculated based on a decomposition.

It is important to note that that Criterion 1 is formulated with passive tracers in mind and should not be expected to hold exactly for active tracers, which are cases that could have different values of eddy diffusivities. Criteria 2 and 3, however, are expected to also hold for temperature and momentum. Although these criteria are known to be satisfied in neutral ABLs, all of them are expected to hold for passive tracers independently of stability.

Considering the decompositions used by the models previously described here (using one and two components), it is straightforward to verify that they do not satisfy all three criteria. We illustrate this fact for selected cases in Appendix C.

Note that Siebesma et al. (2007) introduce similar criteria which include the constraint that $\mathrm{MAX}(K)/(w_* z_e) \approx 0.1$. However, this is not strictly required by any physical arguments and the

reason why virtually all parameterizations since Troen et al. (1986) exhibit this feature is that a cubic shape function is the lowest degree polynomial that can satisfy all physically-motivated boundary conditions for $K(z)$ (O'Brien, 1970), which happens to have a maximum of ≈ 0.15 at 1/3 of the domain.

3.2.4 Satisfying the criteria and decomposition options

All of the flux separations reviewed so far divide the total flux into either one or two components. Since decompositions based on these separations fail at least one of the consistency criteria, we argue for a broader three-term decomposition. Thus, instead of one nondiffusive component, we argue for two nondiffusive components in addition to the diffusive term:

$$\left\langle w'c' \right\rangle = -K(z)\frac{\partial \langle C \rangle}{\partial z} + \underbrace{\Gamma_s(z) + \Gamma_e(z)}_{F_{ND}}, \tag{3.11}$$

where Γ_s and Γ_e are separate nondiffusive fluxes more clearly defined below. The main motivator for a decomposition into three terms is that it makes it possible for all three of the aforementioned criteria to be satisfied simultaneously.

Since most tracers in the atmosphere exchange mass with the ABL via surface and/or entrainment processes (idealized here as SFTs and ETFs, respectively), we can conceptually link Γ_s to surface fluxes (and thus convective plumes) and Γ_e to fluxes at the entrainment. This allows one to re-write Equation (3.11) as

$$\left\langle w'c' \right\rangle = -K(z)\frac{\partial \langle C \rangle}{\partial z} + \left\langle w'c' \right\rangle_s G_s + \left\langle w'c' \right\rangle_e G_e, \tag{3.12}$$

where $\Gamma_s = \langle w'c' \rangle_s G_s$ and similarly for Γ_e. Here, $\langle w'c' \rangle_s$ and $\langle w'c' \rangle_e$ are the values of the turbulent flux $\langle w'c' \rangle$ taken at the surface and at $z = z_e$, respectively. Furthermore, G_s and G_e are dimensionless shape functions (with their height dependence omitted for brevity) which are assumed to be a function of the flow alone. Thus, knowledge of K, G_s and G_e is sufficient to reconstruct the total flux of any tracer provided that the fluxes at the vertical boundaries of the ABL are known. Given our focus on diagnostic analyses, we obtain $\langle w'c' \rangle_s$ and $\langle w'c' \rangle_e$ from LES results. However, assuming knowledge of these quantities (especially $\langle w'c' \rangle_e$) may be problematic if Equation (3.12) is used to develop prognostic models, in which case they may need to be parameterized.

Although our experience with entrainment fluxes suggests that $G_e(z)$ is small, our criteria suggests that it may be necessary in some conditions. We thus consider the general three-term decomposition in Equation (3.12) throughout our manuscript and rely on results from numerical simulations to indicate the relative importance of $G_e(z)$ (see Section 3.5).

3.2.5 Estimating the components

In order to decompose the flux using three terms according to Equation (3.12) we need $K(z)$, G_s and G_e. We estimate these functions assuming no *a priori* scaling or shape for either of them by considering a SFT and an EFT subjected to the same flow (and thus with the same $K(z)$, G_e and G_s), which leads to the following system of equations:

$$\left\langle w'c'_{\mathrm{SFT}}\right\rangle = -K(z)\frac{\partial\left\langle C_{\mathrm{SFT}}\right\rangle}{\partial z} + \left\langle w'c'_{\mathrm{SFT}}\right\rangle_e G_e, + \left\langle w'c'_{\mathrm{SFT}}\right\rangle_s G_s, \tag{3.13}$$

$$\left\langle w'c'_{\mathrm{EFT}}\right\rangle = -K(z)\frac{\partial\left\langle C_{\mathrm{EFT}}\right\rangle}{\partial z} + \left\langle w'c'_{\mathrm{EFT}}\right\rangle_e G_e. \tag{3.14}$$

Note that while a SFT has both components of the nondiffusive flux (since there may be a small flux of C_{SFT} through z_e), an EFT only has the entrainment-driven flux, since $\left\langle w'c'_{\mathrm{EFT}}\right\rangle_s = 0$ as a boundary condition.

Exact closures are possible by making extra assumptions (such as $G_e = 0$), but as was mentioned before, these options all fail one or more of the introduced criteria (see Appendix C). The approach proposed here is to introduce an optimization method that uses only fluxes and mean scalar gradients of SFTs and EFTs in order to estimate an eddy diffusivity profile. To that end, we introduce a cost function χ to be minimized in an optimization procedure, which can be written generally as

$$\chi = \mathscr{F}\left(K, G_s, G_e\right). \tag{3.15}$$

Although the definition of χ is ultimately arbitrary, we choose it so that nondiffusive fluxes F_{ND} are minimized, while still accommodating the fact that $K(z)$ is equal for every scalar being transported. This choice is mainly motivated by modeling purposes, but partially by physical arguments. Most of the modeling motivation comes from decades of experience with diffusive closures, which have shown that F_D alone can be very powerful in modeling fluxes (Corrsin, 1975).

Furthermore, diffusive operators are numerically well-behaved, easy to implement, and ubiquitous throughout the atmospheric community. Finally, as a physical motivation, we know that in some regimes (such as neutral or stable) the coherent structures are generally small (Jayaraman et al., 2018) and the flux is mostly diffusive (see Section 3.4), and by minimizing F_{ND} we ensure that such situations are captured by our approach. The chosen cost function for this purpose can be written as

$$\chi = G_s^2 + G_e^2. \tag{3.16}$$

It should be noted that there are different ways to formulate a cost function that minimizes F_{ND} (e.g. using absolute value operators or using fourth powers instead of second powers). We have tried several other variations and found that, while the results are qualitatively similar to results using Equation (3.16), some of the features were less appealing from a physical perpective.

The optimization can be made in two ways and both will be analyzed here. In both cases the constraint that $K \geq 0$ is enforced but in the simplest approach G_e and G_s are left unconstrained and can become negative at some regions of the ABL. This option is called the unconstrained version of the optimization. The alternative (constrained version) is to impose that both G_e and G_s be always nonnegative, which avoids nondiffusive counter-gradient fluxes for SFTs and EFTs. Note that counter-gradient fluxes can happen in ABLs and so, *a priori*, both versions of the optimization are equally plausible.

We emphasize here that even though we make χ a partly physically-motivated function, its choice is ultimately arbitrary given the lack of a proper definition of diffusive and nondiffusive fluxes. We nonetheless show that our choice of χ produces results that make physical sense as the final product (see Section 3.4) and are easily reproducible in any simulation that contains a SFT and an EFT. Furthermore, although all results presented in this paper use a SFT and an EFT (see Equations (3.13)-(3.14)), results using temperature and an EFT as the two scalars are very similar. This builds confidence in our method since temperature is very different from an SFT: not only it is an active tracer but it also has a significant entrainment-forced component. Using temperature and a SFT, however, produces poorer results, most likely because both scalars have very similar turbulent fluxes and gradients in the bottom half of the ABL, producing a system of equations that is approximately linearly dependent. Refer to Section 3.5.3 for the extension of this method to

temperature.

3.3 Numerical aspects

Table 3.1: Parameters for the simulations used in this paper. All simulations have 256 points in the horizontal direction and 400 points in the vertical direction. Note that we show the negative real root corresponding to w_* for the stable case for the sake of simplicity.

Name	$\langle w'\theta' \rangle_s$ (m K/s)	u_* (m/s)	w_* (m/s)	L_o (m)	L_x, L_y (m)	L_z (m)	z_e (m)	z_T (m)
Stable	-0.20×10^{-2}	0.15	-0.17	133.7	500	300	72.8	152.3
Neutral	0	0.20	0	$-\infty$	3000	1000	355.0	542.5
Rolls	0.15×10^{-2}	0.23	0.29	-585.5	3500	1200	462.0	627.0
Plumes	3.76×10^{-2}	0.28	1.22	-41.7	7680	2700	1390.5	1647.0

We use an LES model to apply the theory and methods introduced in Section 3.2. Our model has been extensively validated and was already used in several other investigations (Kumar et al., 2006; Salesky et al., 2017). As a brief description, our model employs a pseudo-spectral scheme in the horizontal directions (with doubly-periodic horizontal boundary conditions) and a centered finite differences in the vertical direction to solve the flow. The top one quarter of the domain has a sponge layer to mimic an open boundary and we use a Lagrangian-Averaged Scale-Dependent dynamic subgrid scale model for closure (Bou-Zeid et al., 2005). The tracer advection is solved using a finite volume scheme embedded into the spectral code with bounded advection (Chamecki et al., 2008).

Four simulations are used in total and their main difference is the buoyancy forcing at the surface, which reflects four different stability conditions ranging from weakly stable to strongly unstable. The rotation frequency was set to $1 \times 10^{-4}\,\mathrm{s}^{-1}$ in all cases and the grid has 256 points in the horizontal direction and 400 in the vertical direction. Note that our model has been shown to converge at coarser resolutions than similar models with different subgrid scale closures (Salesky et al., 2017). The initial potential temperature (θ) profile is well-mixed until approximately 90% the reported ABL height with a constant gradient of $2 \times 10^{-2}\,\mathrm{K\,m}^{-1}$ above it. Each simulation has a different domain length which can be found in Table 3.1 along with other parameters. Note that

the names of the simulations reflect a regime characteristic. Simulations Stable and Neutral are named after their stability condition. Simulations Rolls and Plumes are both convective and are named after the main coherent structure that transports the quantities from the surface (Salesky et al., 2017). They can be both classified as weakly and strongly unstable, respectively (Jayaraman et al., 2018). Note that Salesky et al. (2017) calls the strongly convective regime the "cell" regime, due to the horizontal imprint of convective plumes, but the dominating coherent structures are the plumes, which is why the present name was chosen.

The roughness length is set to $z_0 = 1 \times 10^{-2}\,\mathrm{m}$ throughout, and all simulations are forced with a geostrophic velocity of $5\,\mathrm{m/s}$ in the x-direction imposed by a pressure gradient. We minimized the effects of inertial oscillations by setting the initial conditions for velocity to their average over one inertial period (taken from identical simulations that were run only for this purpose). All of the simulations had a spin-up period of at least 8 convective cycles T_* and the statistics were collected during the next $8T_*$ period (calculated as $T_* = z_e/\mathrm{MAX}(u_*, w_*)$, where the turbulent convective velocity is calculated as $w_*^3 = g\,\langle w'\theta'\rangle_s\, z_e/\theta_s$ and $\theta_s = 300\,\mathrm{K}$ is a potential temperature scale).

All simulations also have two passive tracers: a SFT and an EFT with concentrations C_{SFT} and C_{EFT} which have different initial and boundary conditions. Entrainment fluxes are accomplished, as previously discussed, by imposing different initial concentrations for the mixed layer and above it. Thus, EFTs are initialized with zero concentration until approximately $0.9\,z_e$ and nonzero concentration above. SFTs are initialized with a $C_{\mathrm{SFT}} = 0$ throughout the domain. EFTs have a zero-flux boundary condition at the surface, while we impose a nonzero surface mass flux into the ABL for SFTs. Both tracers have horizontally periodic boundary conditions and a sponge layer assures that the top of the domain does not affect results in the ABL. Throughout this paper tracer fluxes are normalized either by their value at the surface or at z_e, so they are dimensionless. It is worth noting that for both tracers there is no steady-state for the concentrations in the ABL (since there are sources but no sinks). However, our chosen averaging period ($8T_*$) ensures that effects of time-dependency are negligible.

We apply both versions of the optimization procedure introduced in Section 3.2 (constraining G_s and G_e to be non-negative and not constraining them) using an optimization library freely available in the Python package SciPy (Virtanen et al., 2019). The optimization takes an initial guess for $K(z)$,

G_s and G_e, and iterates until an optimal solution is reached. Although the optimization approach proved to be mostly independent of the initial guess, we formalize it by always starting at the uppermost grid point (thus well into the stratified layer above the ABL) and setting the initial guess so that both $K = G_s = G_e = 0$ (which is always approximately true in the stratified layer). We then proceed downwards by using the result from the previous grid point as an initial condition for the next one.

3.4 Results and discussion

In this section we present the results for F_D and F_{ND} based on our decomposition, and then move on to discuss the eddy diffusivity and shape function profiles. For visualization purposes, we normalize the vertical axis in all simulations by z_T. Note that it is useful to analyze results as a function of the bulk ABL stability $-z_e/L_o$ which is equivalent to $\kappa w_*^3/u_*^3$.

3.4.1 Diffusive/nondiffusive flux decompositions

Figs. 3.2 and 3.3 show results for simulations Stable and Neutral, respectively. In both regimes results for the unconstrained (top rows) and constrained (bottom rows) optimizations are very similar and the diffusive components dominate the flux in all cases. This result is in agreement with our expectations for neutral and stable conditions, where the total turbulent fluxes are mostly accomplished by small eddies and are likely to be well represented by F_D alone.

Figure 3.4 shows results for simulation Rolls, where we see that, in general, nondiffusive fluxes are not negligible. The nondiffusive contribution is especially important for the SFT, as one would expect, indicating the role of large coherent flow structures in transporting the mass when the tracer source is located at the surface even in weakly convective regimes. Although there are some differences between the constrained and unconstrained optimizations, they are qualitatively very similar.

Figure 3.5 shows results for simulation Plumes, where we see that a significant portion of the fluxes is performed by the nondiffusive component, as is expected from our knowledge of convective

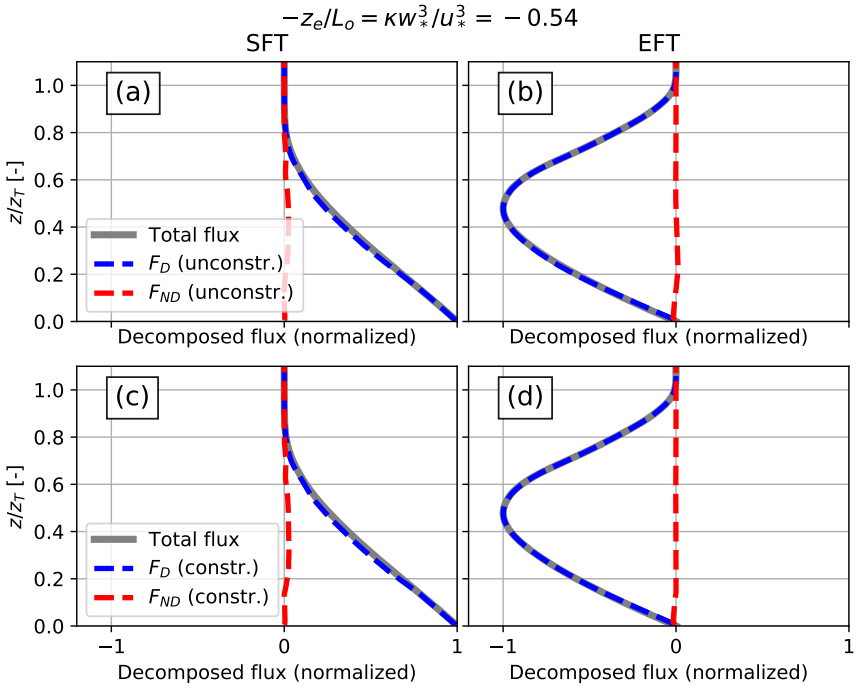

Figure 3.2: Decomposition of mean turbulent tracer fluxes of simulation Stable for the unconstrained optimization approach (top rows; panels a and b) and constrained approach (bottom rows; panels c and d). Left panels show results for the SFT and right panels show results for the ETF. Black lines are the total flux, blue lines show the diffusive component and red lines show the nondiffusive component.

ABLs. For both the constrained and unconstrained optimizations, the majority of the fluxes for the SFT are nondiffusive. Once again, although the constraints do modify the results, there is no qualitative difference between both approaches for the SFT. For the EFT, both optimizations show a smaller importance of nondiffusive fluxes compared to the SFT. However, while the unconstrained version shows a non-negligible counter-gradient flux for the EFT around $z/z_T = 0.2$, the constrained optimization produces almost no nondiffusive fluxes in this case. It is worth mentioning that the resulting diffusive-nondiffusive decompositions for a SFT in this regime are very similar to results for temperature shown in Fig.7d of Siebesma et al. (2007).

Thus, for most decompositions in the regimes analyzed here the choice of a constrained versus an unconstrained optimization does not qualitatively change the results. The exception is the EFT in simulation Plumes, which exhibits regions of negative values for G_e in the unconstrained optimization, implying counter-gradient nondiffusive fluxes due to entrainment. Although this

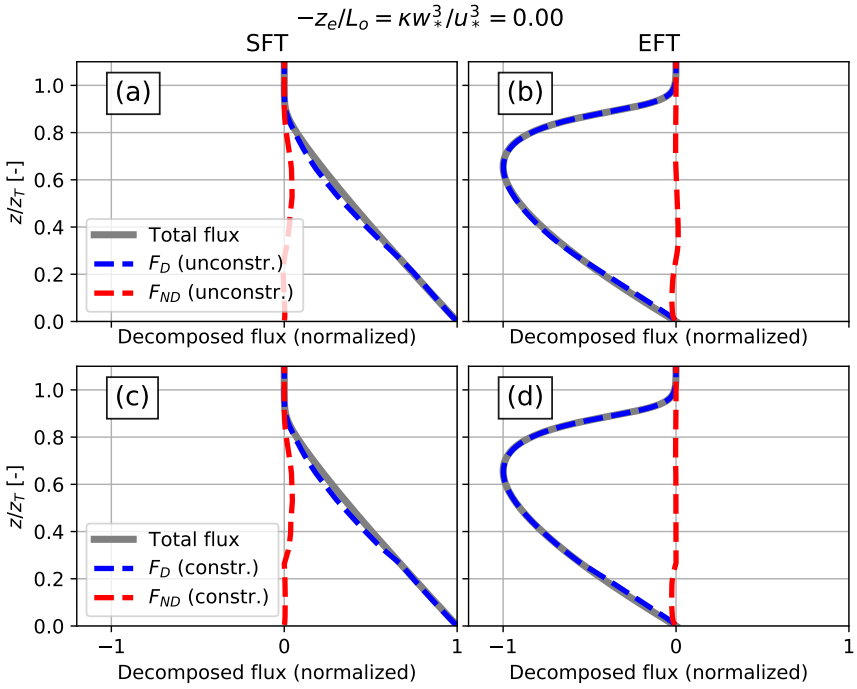

Figure 3.3: Decomposition of mean turbulent tracer fluxes of simulation Neutral for the unconstrained optimization approach (top rows; panels a and b) and constrained approach (bottom rows; panels c and d). Left panels show results for the SFT and right panels show results for the ETF. Black lines are the total flux, blue lines show the diffusive component and red lines show the nondiffusive component.

feature does not immediately fit into our current understanding of transport in convective ABLs, it is not an impossibility (given that not much has been explored about the specific dynamics of tracer transport from the stratified free troposphere into the ABL) and there are no grounds to consider one optimization approach superior to the other with the present data.

Furthermore, in the separation between local and nonlocal fluxes proposed by Zhou et al. (2018), there is evidence that much of the entrainment flux in convective regimes is accomplished by nonlocal fluxes. Our results indicate that despite that fact this flux can be successfully parameterized as a diffusive process.

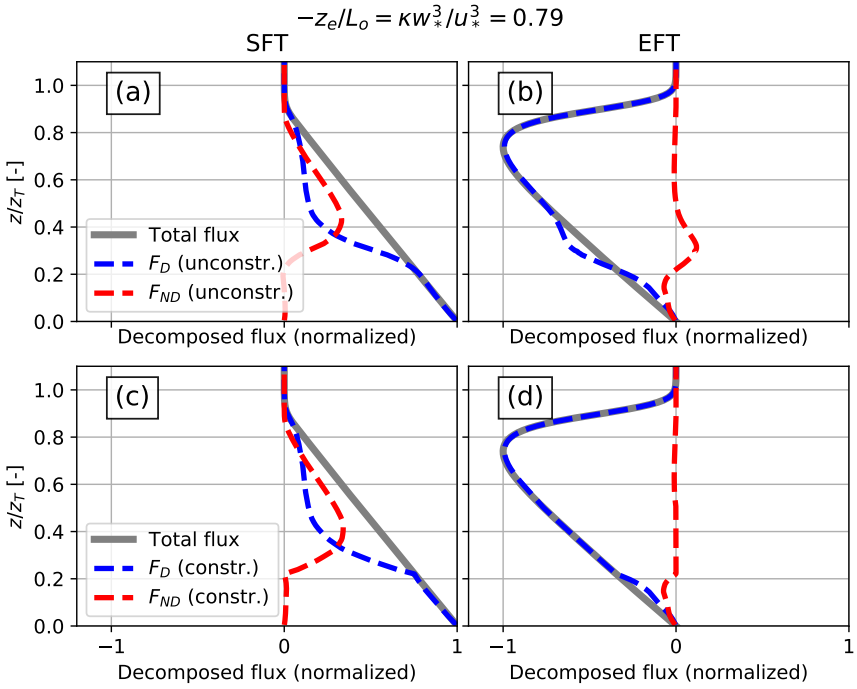

Figure 3.4: Decomposition of mean turbulent tracer fluxes of simulation Rolls for the unconstrained optimization approach (top rows; panels a and b) and constrained approach (bottom rows; panels c and d). Left panels show results for the SFT and right panels show results for the ETF. Black lines are the total flux, blue lines show the diffusive component and red lines show the nondiffusive component.

3.4.2 Eddy diffusivities and shape functions

We dedicate this section to the analysis of $K(z)$, G_s and G_e obtained through our optimization. We use TM86's model, given in Equations (3.6)-(3.9), as a qualitative reference when discussing results. For optimal results h is chosen on a case-by-case scenario to approximately match the height at which the estimated eddy diffusivities go to zero (which is the effect it has on $G(z/h)$). This is done in order for us to focus on the comparison of the eddy diffusivities without worrying about the precise estimation of h. We use the empirical similarity functions ϕ given in Large et al. (1994) for all regimes, which is based on data for the atmosphere and follows the $1/3$ scaling in the convective limit (Kader et al., 1990; Katul et al., 2011). In our implementation we set $C_* = 6.5\,\kappa$ in all cases to match TM86's choice.

Since the neutral case is the most well-studied ABL regime, we start with Fig. 3.6, which shows

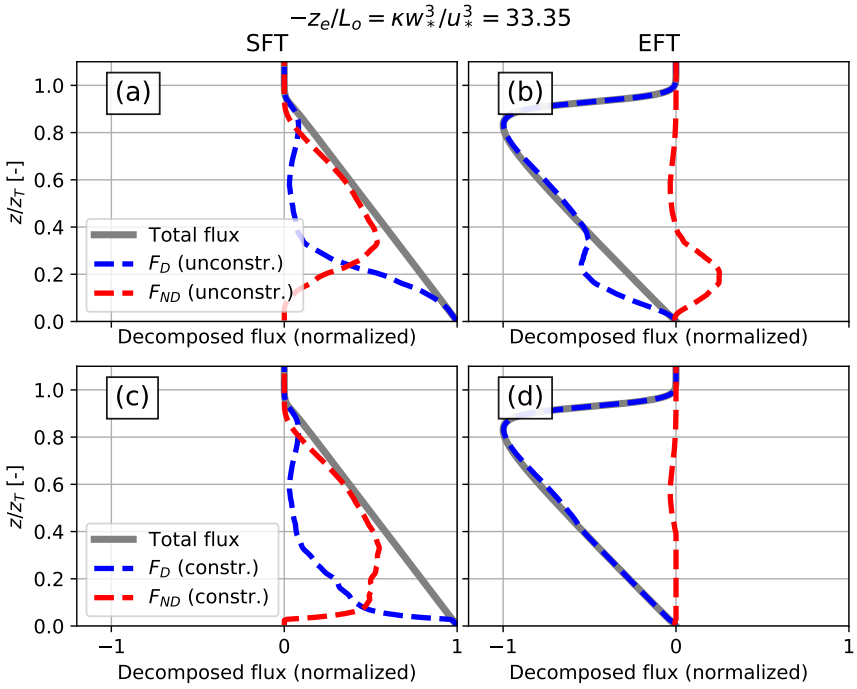

Figure 3.5: Decomposition of mean turbulent tracer fluxes of simulation Plumes for the unconstrained optimization approach (top rows; panels a and b) and constrained approach (bottom rows; panels c and d). Left panels show results for the SFT and right panels show results for the ETF. Black lines are the total flux, blue lines show the diffusive component and red lines show the nondiffusive component.

different estimations of $K(z)$ for simulation Neutral. The ABL height in TM86's profile is set to $h = 0.9z_T$. Figure 3.6a shows results for the entire ABL, where we can see that all estimates are very similar, which is expected. The surface-forced eddy diffusivity K_{SFT} is shown only for reference and is the result of assuming $F_{ND} = 0$; thus it is not a part of our method. Note also that $K_{\mathrm{EFT}}(z)$, which is also not part of our method, is very similar to the other curves shown (as expected) but it is not depicted for brevity. Figure 3.6b zooms in on the lower ABL, where we can see that all estimates of $K(z)$ approximately match MO similarity theory in the surface layer (given by TM86's profile, which is built to follow MO similarity theory close to the surface). We attribute the small deviation to inherent limitations of the subgrid-scale models and wall models employed as part of the LES technique (Khanna et al., 1997; Porté-Agel et al., 2000; Bou-Zeid et al., 2005; Brasseur et al., 2010) and consider that $K(z)$ satisfies criterion 3.

Figure 3.7 shows eddy diffusivity estimations for simulations Stable, Rolls and Plumes. The

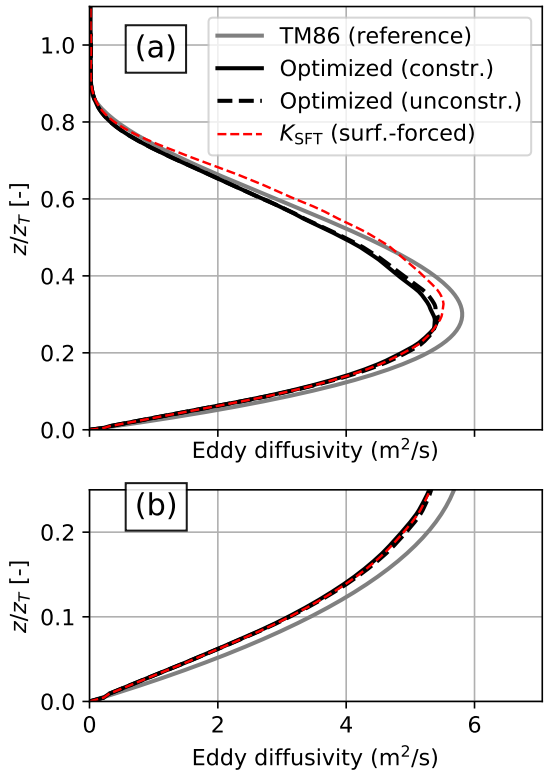

Figure 3.6: Estimation of the eddy diffusivity for simulation Neutral using the constrained optimization (solid black lines), unconstrained optimization (dashed black lines). Also shown for reference are the SFT's eddy diffusivity $K_{\mathrm{SFT}}(z)$ (dashed red line; obtained via Equation (3.3)) and TM86's parameterization (solid gray line). Panels a and b only differ in the range of the vertical axis.

ABL heights for TM86's model is $h = 0.95z_T$ for Stable and $h = 0.9z_T$ for Rolls and Plumes. Note that for the stable case (panel a) all curves are similar to each other, including the reference TM86 profile, which is not true for the other cases, where there is a clear difference between the cubic profiles from TM86 and our estimations from the optimization procedure.

For the weakly convective case (Fig. 3.7b) there is a small difference between the constrained and unconstrained approaches, but both produce significantly larger values than TM86's profile. Although there is some ambiguity when defining h, it cannot account for a discrepancy that large. The $K(z)$ estimations for the strongly convective case (Fig. 3.7c) are also distinct, with clear differences in shape and magnitude between them.

In all cases (including simulation Neutral) the eddy diffusivity profiles are mostly of convex shape, with an approximately zero derivative at z_e. Furthermore, the peak value seems to always be

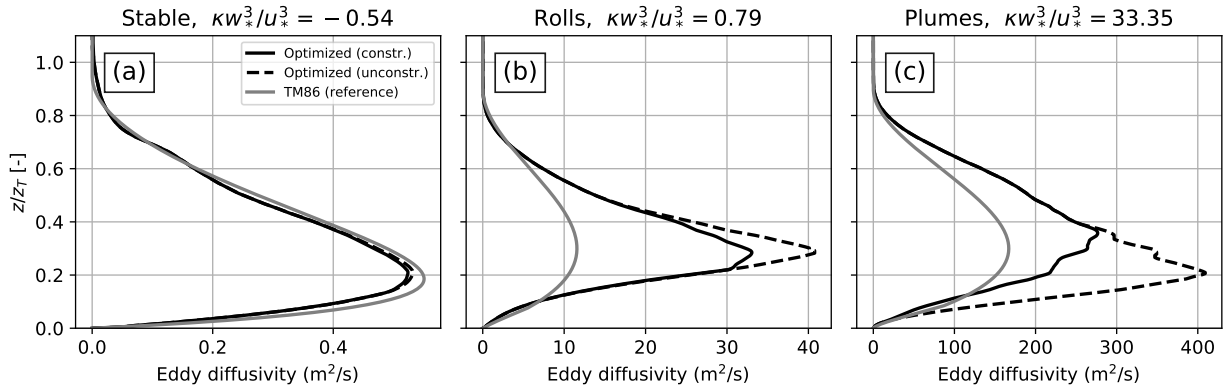

Figure 3.7: Estimates for eddy diffusivity $K(z)$ for non-neutral simulations Stable, Rolls and Plumes. Solid black lines are results for the constrained optimizations, dashed back lines are results for the unconstrained optimization and solid gray lines are results TM86 for reference.

located in the lower portion of the ABL. We emphasize that these features (which are imposed in most eddy diffusivity parameterizations) are not imposed in any way in our optimization procedure, but emerge naturally.

Our optimization-based estimates for simulations Rolls and Plumes are re-plotted in Fig. 3.8 along with $K_{\mathrm{SFT}}(z)$ and $K_{\mathrm{EFT}}(z)$. Note that in both panels K_{SFT} is significantly larger than K_{EFT}. This is expected and it occurs because SFTs are transported vertically by strong coherent updrafts, making them much more well mixed (and with a much lower vertical gradient) than EFTs for a similar turbulent flux, thus producing a larger eddy diffusivity through Equations (3.3)-(3.4) (Wyngaard et al., 1984).

In Fig. 3.8, both optimized $K(z)$ follow $K_{\mathrm{SFT}}(z)$ at the bottom of the domain (thus obeying criterion 3) and $K_{\mathrm{EFT}}(z)$ at the top of the domain. (Note that for the Plumes case the constrained $K(z)$ follows K_{SFT} only in a small percentage of the surface layer.) It is likely that K_{SFT} and K_{EFT} are more relevant in these respective regions, which builds confidence in our optimization. Note also that while the $K(z)$ from our unconstrained optimization lies in between both K_{SFT} and K_{EFT} in a significant region in the middle of the ABL, the constrained version appears to simply switch between both, being approximately equal to K_{SFT} in the lower ABL and K_{EFT} in the upper ABL. This opens the possibility of approximating the resulting $K(z)$ for the constrained optimization as $K(z) = \mathrm{MIN}(K_{\mathrm{SFT}}, K_{\mathrm{EFT}})$, which is a much faster calculation. Finally, K_{EFT} alone appears to be a

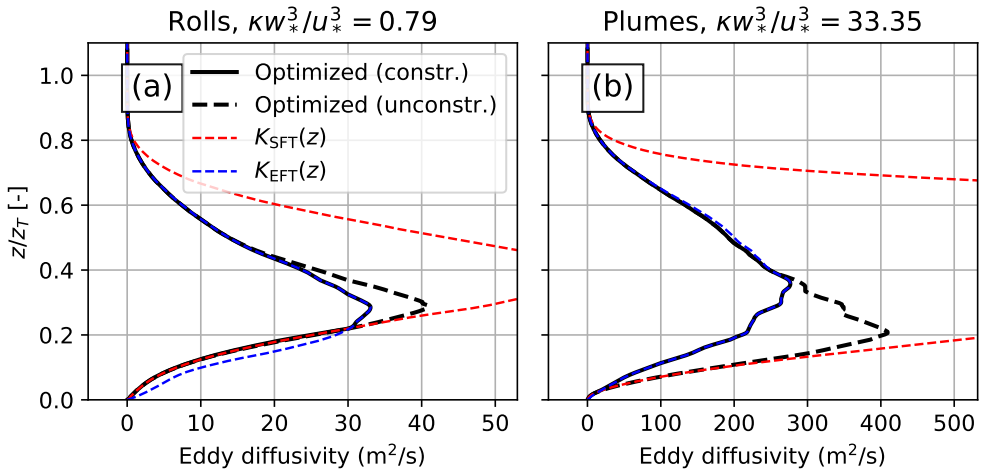

Figure 3.8: Estimates for eddy diffusivity $K(z)$ for non-neutral simulations Rolls and Plumes. Solid black lines are results for the constrained optimizations, dashed back lines are results for the unconstrained optimization, dashed red lines are results TM86 for the surface-forced eddy diffusivity K_{SFT} and dashed blue lines are results for the entrainment-forced eddy diffusivity K_{EFT}.

somewhat good approximation of $K(z)$ calculated with the unconstrained optimization (with the caveat that K_{EFT} does not follow the MO similarity theory prediction at the surface).

Figure 3.9 shows the shape functions G_s (left) and G_e (right) and each row corresponds to a different case, indicated on the right side of the figure. Note that the shape functions for simulations Stable and Neutral have small values in all cases, as can be anticipated by the results from Figs. 3.2 and 3.3. This is not the case for unstable conditions, where we see magnitudes close to 0.4 and 0.6 for G_s. Although it is tempting to interpret this fact as indicating that up to 60% of the tracer flux at surface is carried via nondiffusive processes, this is not strictly true since the total flux changes with height.

There is no significant qualitative difference between the constrained and unconstrained optimizations for G_s in the unstable cases (panels e and g). Furthermore, G_s shapes are similar between these two simulations (with the possible exception of the magnitudes near the surface). Together with the fact that the nondiffusive fluxes appear to be approximately zero in stable and neutral regimes, this makes it relatively easy for an analytical model to capture this behavior with a convex function for G_s.

G_e, however, exhibits significant difference between both optimization approaches in the unsta-

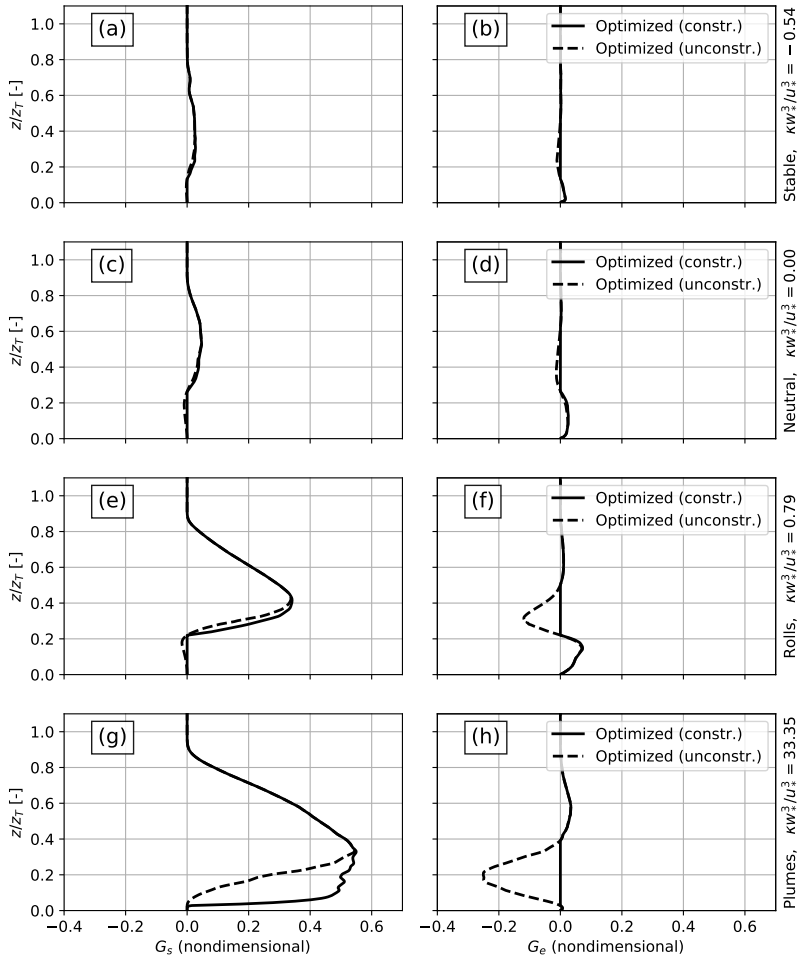

Figure 3.9: Shape functions G_s (left panels) and G_e (right panels). Different rows show results for different simulations, whose names are indicated on the right side of the figure. Solid black lines are results for the constrained optimizations and dashed back lines are results for the unconstrained optimization.

ble regimes (panels f and h). The unconstrained optimization results in significant negative values for G_e in the unstable simulations (especially for simulation Plumes), indicating counter-gradient fluxes performed by entrainment processes. The constraints for G_e avoid this behavior, resulting in a much smaller contribution of nondiffusive entrainment processes. This poses a challenge for modeling such components and indicates that using the constrained version of the optimization produces results that may be advantageous for modeling purposes. This issue will be further explored in Section 3.5. It should be noted that it is counter-intuitive that G_e, an entrainment-driven nondiffusive transport, makes corrections in the lower ABL, as opposed to the upper ABL.

It should also be noted that we expect $G_s \approx 0$ from the surface until $\approx \text{MIN}(0.1z_e, -L_o)$ according to MO similarity theory, indicating that SFT fluxes are fully diffusive in that region (Kaimal et al., 1994, Section 1.4.2). While all of the shapes respect that, G_s for simulation Plumes (panel g) is in approximate violation for the constrained optimization. Although it should also be noted that the upper limit for this range (in the Plumes case $L_o/z_T \approx 0.03$) comes from scale analysis and is therefore approximate. While some features of the constrained optimization allow for simplifications when modeling (see Section 3.5), this feature in particular is undesirable from a physical point of view. Note also that G_e does not need to respect this rule since it is associated with entrainment fluxes, rather than surface fluxes, and need not be subject to MO similarity theory restrictions.

Finally, we note that there are clear differences in the decomposition between the simulation in the rolls and plumes regimes. This is in contrast to the results of the local/nonlocal decomposition of Zhou et al. (2018), where the decompositions for both regimes are very similar (see their Fig. 5).

3.5 Overall tendencies and implications for modeling

Although three terms are necessary for all three plausibility criteria to be satisfied in decompositions, parameterizations are always approximations and can satisfy all criteria with only two terms. With that in mind, we proceed to analyze the results from the previous section in terms of bulk quantities and discuss them in the context of model development.

Note that since we only have four data points (one for each simulation) any interpolation to intermediate stability conditions other than the ones presented should be done with care. For this reason we make no attempt at creating a novel model based on our results, which would require a larger set of stability regimes to be investigated.

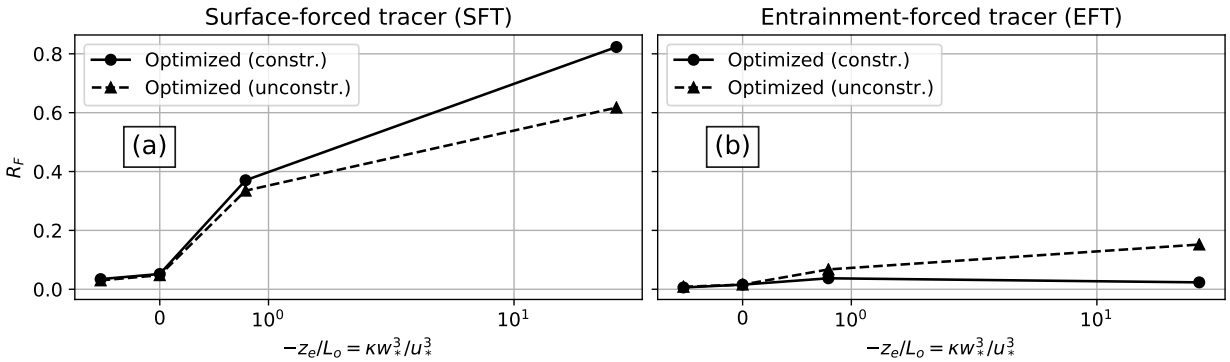

Figure 3.10: Ratio of nondiffusive to total fluxes R_F, defined in Equation (3.17). Solid black lines are results for the constrained optimization, dashed black lines are results for the constrained version, panel a shows results for SFTs and panel b shows results for EFTs. Note that the horizontal axis has a linear scale from -1 to 1 and a log scale everywhere else for convenience.

3.5.1 Bulk analysis of flux partition

We gain context by quantifying the importance of nondiffusive fluxes in different stability regimes. For that purpose we define a bulk measure R_F as

$$R_F = \left[\frac{\int_0^\infty F_{ND}^2 dz}{\int_0^\infty \left(F_D^2 + F_{ND}^2\right) dz} \right]^{1/2}. \tag{3.17}$$

Results for R_F are presented in Fig. 3.10 for SFTs (panel a) and EFTs (panel b). For SFTs we see a clear general tendency for nondiffusive fluxes to become more important as conditions become more unstable, regardless of the version of the optimization. It is interesting to note, however, that nondiffusive fluxes are important even for weakly unstable conditions. For example, simulation Rolls ($\kappa w_*^3/u_*^3 \approx 0.8$ in the figure) has $R_F \approx 0.4$, which indicates that about 40% of the flux is nondiffusive and the contribution of the nondiffusive fluxes reaches 80% for the constrained optimization in the most convective regime. It is worth noting that, due to possible cancellations among the flux components and an extra term in the denominator, interpreting R_F as a percentage of fluxes is not precisely correct. However, as cancellations between F_D and F_{ND} are usually small, we take this as a reasonable approximation for simplicity.

In Fig. 3.10b we see results for EFTs, where there is a similar monotonically increasing tendency for the unconstrained version of the optimization. Note that the values of R_F for this are much lower

than for SFTs, as expected. Constraining the optimization however, does appear to qualitatively change results for EFTs, since there is no monotonic increase with stability in this case.

3.5.2 Modeling considerations

We begin by considering the modeling of the diffusive component of the total flux and analyze our eddy diffusivity estimates by some bulk measure. Taking a bulk mixing-length argument (Davidson, 2004, Sec. 4.1.2) and ignoring any coefficients which might be present, one may approximate $K \sim z_e U_s$, where U_s is a velocity scale of the flow relevant to the mixing. We can estimate U_s for our optimization-based estimate using the peak of $K(z)$ in the ABL:

$$U_s^{\mathrm{OPT}} = \frac{\mathrm{MAX}(K^{\mathrm{OPT}}(z))}{z_e}, \tag{3.18}$$

where K^{OPT} refers to the eddy diffusivity results obtained with the optimization procedures. Introducing a similar bulk measure U^{TM86} for TM86's eddy diffusivities, we can create a measure R_U as

$$R_U = \frac{U_s^{\mathrm{OPT}}}{U_s^{\mathrm{TM86}}}. \tag{3.19}$$

Given that our optimization attempts to maximize $K(z)$ based on data (and thus can be seen as an upper bound for $K(z)$), a situation where $R_U < 1$ implies that the classic TM86 parameterization predicts larger eddy diffusivities than are supported by data.

Results for R_U can be seen in Fig. 3.11 as a function of stability. Note that, for all cases, $R_U \approx 1$ which indicates that TM86 curves do not overpredict $K(z)$, as expected. Moreover, TM86 estimates agree remarkably well with our optimized ones for the stable and neutral cases. In strongly convective conditions (simulation Plumes) the values for both optimizations are around $R_U \approx 2$, but since most of the flux is performed by F_{ND} (see Fig. 3.10) the precise value of $K(z)$ is less important in this case.

The largest ratio R_U happens for the weakly unstable regime, where $w_*/u_* = \mathcal{O}(1)$ and shear and buoyancy forcings are comparable. Although intermediate regimes are generally more challenging to capture, the large difference is somewhat surprising. Note that although we choose h in an *ad-hoc* manner, our value is always within 10% of the canonical estimate for h and, at maximum, we are

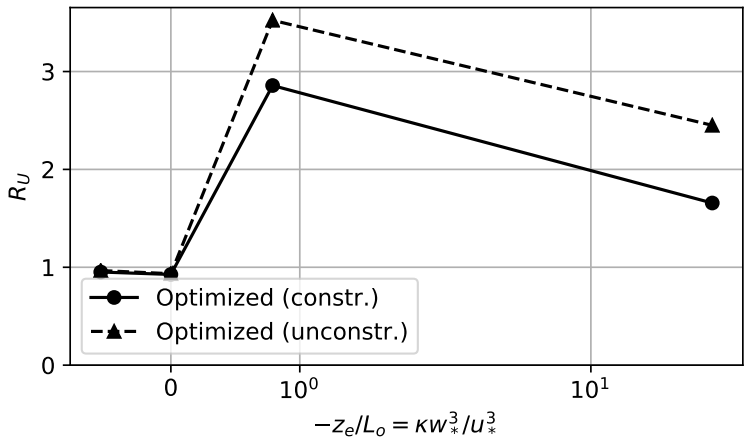

Figure 3.11: Results for R_U using both versions of the optimization algorithm. Solid line shows results for the constrained optimization and dashed lines show results for the unconstrained version. Note that the horizontal axis has a linear scale from -1 to 1 and a log scale everywhere else for convenience.

introducing a 10% error in U_s^{TM86} when compared to a more rigorous calculation of K^{TM86}.

In TM86's model U_s^{TM86} is associated with MO similarity theory due to the surface scaling (according to TM86, $\mathrm{MAX}(K) \approx 0.15\, u_* h/\phi$). Thus, this large value of R_U for simulation Rolls suggests that TM86's assumption that MO similarity theory determines $K(z)$ in the bulk of the ABL may not be appropriate for weakly unstable conditions. From a physical perspective, this points to the ABL being more diffusive than MO similarity theory would predict and further investigation would be helpful to clarify this issue. From a modeling perspective, there is an opportunity for improvement of TM86's model that could be implemented by making the bulk of the ABL independent from MO similarity theory and/or introducing a stability dependence on the shape function G.

Focusing now on the modeling of the nondiffusive component of the flux F_{ND}, we refer back to Figs. 3.9 and 3.10b. G_e profiles change between simulations Rolls and Plumes in a non-trivial way, making it challenging to model contributions from entrainment processes to F_{ND}. However, contributions from entrainment processes to nondiffusive fluxes are below 20% across the regimes considered in this work for EFTs and below 10% considering the constrained version of the optimization (Fig. 3.10b). This result justifies the community practice of neglecting nondiffusive contributions from entrainment processes (i.e., $G_e = 0$).

Furthermore, this motivates us to consider a truncated decomposition where G_e is neglected and we approximate $F_{ND} \approx \langle w'c' \rangle_s G_s$. Note that this is not the same as assuming $G_e = 0$ and only then calculating $K(z)$ and G_s. This latter approach is illustrated in Appendix C and it produces unrealistic results for G_s near the surface. In our approach G_e is calculated alongside $K(z)$ and G_s with our optimization procedure (thus using the same curves that were already presented) but is subsequently neglected, thus creating a truncated decomposition. This allows us to use the estimated shape for G_s (already shown in the left panels of Fig. 3.9) as a guide to modeling.

To that end, we consider the two main currently-used modeling approaches for G_s for qualitative comparison with our results: TM86's model and EDMF, whose profiles for G_s are calculated as $G_s = F_{ND_{\mathrm{SFT}}} / \langle w'c'_{\mathrm{SFT}} \rangle_s$. TM86's model is fully described by Equations (3.6)-(3.9). For EDMF's calculation of F_{ND} (given by Equation 3.10) we need expressions for the mass flux M and the tracer concentration in the updrafts $\langle C \rangle_u$. It is beyond the scope of the present work to compare different formulations for these quantities and we use Equations (7), (10), (17), (21), and (23) (along with respective constants) from Siebesma et al. (2007) to model M and $\langle C \rangle_u$. These equations are run diagnostically using LES profiles averaged over an hour as the environment average.

Figure 3.12 panels a and c show G_s for simulations Rolls and Plumes according to our constrained optimization, TM86's model, and EDMF. TM86's model is qualitatively similar to our optimized curve, especially in the strongly unstable regime (panel c). G_s from the EDMF model are unphysical in the sense that their magnitude is at times larger than unity in both simulations, indicating regions with larger fluxes than at the surface. This happens because we have performed a diagnostic analysis in which the EDMF calculations are carried out with averaged profiles from LES, rather than averaged profiles that are advanced in time using EDMF itself. This is due to the fact that our main goal is assessing the accuracy of modeling assumptions rather than model performance after implementation (akin to an *a priori* test in LES literature; see Pope (2000, Section 13.4.6) and Meneveau et al. (2000, Section 2.1)). Given that EDMF is built primarily as a prognostic tool, results are likely to improve if the averaged profiles used are also advanced in time using the EDMF model (Zhou et al., 2018), as is the case with most EDMF validations (Siebesma et al., 2007; Witek et al., 2011).

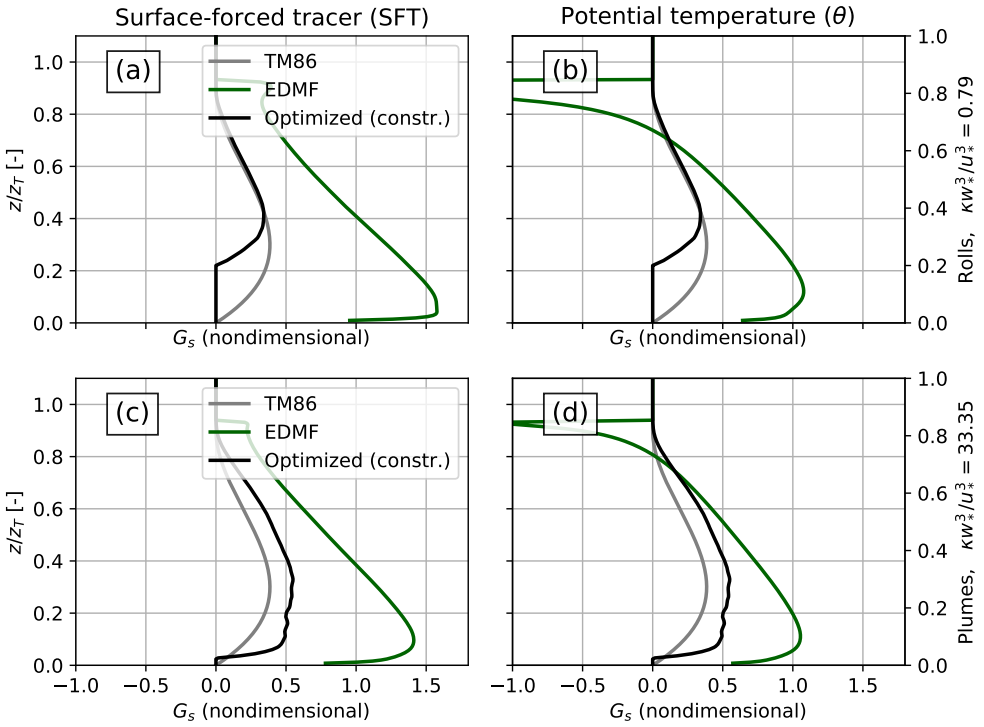

Figure 3.12: Comparison of G_s between our constrained optimization (black line), TM86's model (gray line) and EDMF (green) for both unstable simulations in this work. G_s is calculated for TM86 and EDMF as $F_{ND_{\mathrm{SFT}}} / \left\langle w' c'_{\mathrm{SFT}} \right\rangle_s$ and $F_{ND_\theta} / \left\langle w' \theta' \right\rangle_s$ for left and right columns, respectively.

3.5.3 Modeling of potential temperature fluxes

In order to further investigate results from EDMF, we calculate the shape of the nondiffusive contribution to the flux of potential temperature θ via EDMF equations for simulations Rolls and Plumes, which are plotted in Fig. 3.12, panels b and d. We also plot our optimized G_s (which is strictly only valid for passive scalars) in the same figure for comparison. Although there are regions where $G_s \gtrapprox 1$ for temperature according to EDMF, EDMF profiles for θ are more realistic than for SFTs. Furthermore, profiles are similar between simulations Rolls and Plumes, with the main difference being fluxes at entrainment, in which an unphysical result happens for simulation Rolls ($G_s < -1$). Note that in our optimized decompositions and in TM86's model entrainment fluxes are almost fully a diffusive process, but the opposite is true for EDMF.

Although results for SFTs and temperature may signal a systematic inability of EDMF to represent regimes other than a purely convective one (i.e. free of mean shear), this is in contrast to its use in global models such as the European Centre for Medium-range Weather Forecasts model (Köhler et al., 2011). This could be explained by the aforementioned differences between the diagnostic nature of our analyses and the prognostic nature of the implementations. Given the complexity of the EDMF model, further research is needed to evaluate these claims.

Although the obtained profiles for $K(z)$, G_s and G_e are only valid for passive tracers, we can assume their validity for potential temperature in order to assess the possible universality of such profiles. Note that there is no obvious reason to expect that the curves optimized for passive tracers should work well for temperature, however, such universality would be very convenient for modeling purposes and should be investigated. We examine this possibility by using $K(z)$, G_s and G_e profiles calculated from SFTs and EFTs with a constrained optimization to estimate potential temperature fluxes using Equation (3.12) along with averaged profiles of temperature, temperature flux at entrainment $\langle w'\theta' \rangle_e$ and at the surface $\langle w'\theta' \rangle_s$ from LES. Results are shown in Fig. 3.13 for simulations Stable, Rolls and Plumes. Each panel shows the measured flux from LES and three different modeling approaches with increasing number of terms. It is clear that the fluxes are better reproduced in the unstable simulations than in the Stable one. It is also clear that surface-driven nondiffusive fluxes are important to reconstruct the fluxes in the unstable cases,

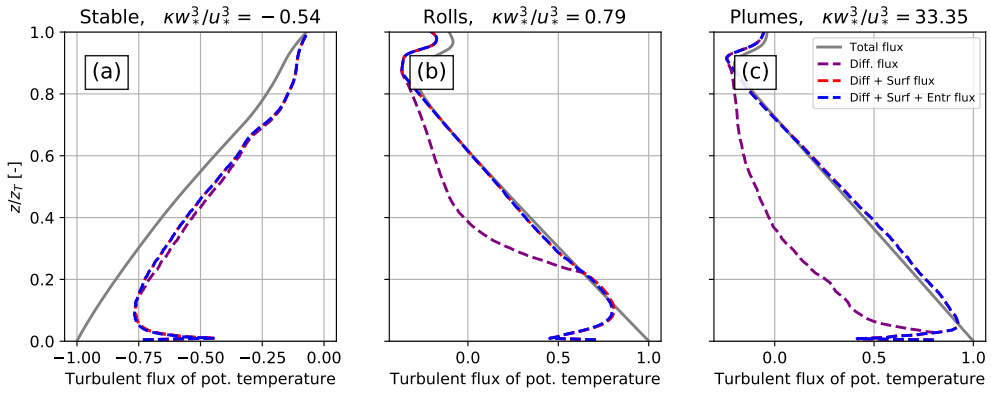

Figure 3.13: Fluxes of potential temperature modeled with $K(z)$, Gs and G_e originally obtained for passive tracers. Panels a, b and c show results for simulations Stable, Rolls and Plumes, respectively. Gray lines are average potential temperature fluxes from LES, purple lines are modeled fluxes using only a diffusive component, red lines include the diffusive component and the surface-driven nondiffusive component, and blue lines include all three components of Equation (3.12). Ratios of temperature at entrainment versus surface $\langle w'\theta' \rangle_e / \langle w'\theta' \rangle_s$ are 0.58, -0.18 and -0.14 for simulations Stable, Rolls and Plumes respectively.

but entrainment-driven nondiffusive fluxes are not (as expected given the results in Fig. 3.10). For unstable simulations results using all three terms are remarkably close in most of the ABL but appear to diverge at the surface. Note that all places where there are significant discrepancies between modeled and LES results (the whole Stable ABL and in the surface layer of unstable cases) are marked by a dominance of diffusive fluxes. This implies that the difference between model and LES-measured fluxes can be accounted for by Prandtl and Schmidt numbers.

3.6 Conclusions

In this work we have introduced a framework for decomposing turbulent fluxes of passive scalars into diffusive (F_D) and nondiffusive components (F_{ND}). Our approach is of diagnostic nature and is based on a partition of the total flux into three distinct terms and a subsequent optimization that estimates them simultaneously without any shape or scaling assumptions whatsoever. Our method requires two separate tracers to be present (a SFT and an EFT) and works in any stability regime. Its premise is to take as much advantage of diffusive fluxes as possible, thus maximizing the eddy diffusivity $K(z)$. Two versions of the method are introduced: while in the unconstrained

version there are no restrictions to F_{ND}, in the constrained version we require that there be no counter-gradient fluxes for tracers with monotonically-decreasing (or increasing) concentration profiles.

Application of our method to LESs reveals that, even when minimizing F_{ND}, nondiffusive fluxes are still important in ABLs that range from weakly to strongly unstable. Furthermore, in the constrained version of the optimization, the entrainment-forced nondiffusive transport (parameterized by G_e) can be neglected and most of the nondiffusive fluxes are due to surface processes (G_s). This justifies the widely-adopted modeling practice of attributing all nondiffusive fluxes to surface-emerging coherent structures (plumes and rolls). However, the constrained optimization has the disadvantage of producing nondiffusive fluxes that are significant close to the surface for strongly convective cases (see Fig. 3.9g) where, according to MO similarity theory, we would expect all the flux to be diffusive. An interesting result from our decomposition is that, despite there being evidence that most of the turbulent fluxes in the entrainment layer of convective ABLs is accomplished by coherent plumes (Zhou et al., 2018), our results suggest that they can be fully modeled as a diffusive process.

Furthermore, qualitative comparison with currently-used models showed that improvements are possible both in the calculation of F_D and of F_{ND}. Our results suggest that in weakly unstable regimes (where $u_* \approx w_*$) models based on TM86 predict $K(z)$ to be much smaller than our optimized $K(z)$, thus under-utilizing diffusive fluxes. This indicates that the middle of the ABL is significantly more diffusive than TM86 model it to be. The reason for this feature is that in TM86-based models the magnitude of $K(z)$ above the surface layer is set by MO similarity theory despite being outside its region of validity (see Equation (3.6)). Moreover, our results indicate that the shape of F_{ND} should vary with different stability conditions, which is currently not included in these models.

Finally, our optimization approach to estimate $K(z)$ and F_{ND} can be useful for model building and assessment. As an assessment tool, our method can be used to identify situations where existing parameterizations are unrealistic, since it gives upper bounds for $K(z)$ and lower bounds for F_{ND}. As a model-building tool, it can also be used to map $K(z)$ and F_{ND} over a large number of stability conditions, thus providing modeling-optimized profiles for $K(z)$, G_s and G_e that should be valid throughout a wide range of stability regimes. Although in principle these profiles are strictly valid

only for passive scalars, a reasonable modeling assumption would be that they can be extended for temperature, which was shown to produce reasonable results for unstable conditions (albeit with a possible need for Prandtl and Schmidt number considerations). Moreover, modifying our method by replacing the SFT with temperature yields very similar results, further building confidence in the extension for the temperature case. The extension for momentum may be more challenging since in many situations the vertical eddy viscosity has to be represented as a tensor.

CHAPTER 4

Modifications of the K-Profile parameterization with nondiffusive fluxes for wave effects

Authors: Tomas Chor, James C. McWilliams and Marcelo Chamecki

Abstract:

The K-profile parameterization (KPP) is a common method to model turbulent fluxes in coarse resolution models. Many versions of KPP exist in the oceanic sciences community and their main difference is how they take the effects of nonbreaking waves into account. Although there is qualitative consensus that nonbreaking waves enhance vertical mixing due to the ensuing Langmuir circulations, there is no consensus on the quantitative aspects and modeling approach. In this paper we use a recently-developed method to estimate both components of KPP (the diffusive term, usually called local, and the nondiffusive component, usually called nonlocal) based on numerically-simulated turbulent fluxes without any *a priori* assumptions about their scaling or their shape. Through this method we show that the cubic shape usually used in KPP is not optimal for wavy situation and propose new ones. Furthermore we show that the formulation for the nondiffusive fluxes, which currently only depend on the presence of surface buoyancy fluxes, should also take wave effects into account. In particular, we show that regimes that have no convection but have Langmuir circulations cannot be represented by KPP unless a Langmuir-driven nondiffusive flux is present. Finally, we investigate how the application of these changes to KPP improves the representation of turbulent fluxes when compared to previous models.

4.1 Introduction

Many state-of-the-art regional and global models parameterize vertical mixing in ocean surface boundary layers (OSBLs) with the K-profile parameterization (KPP; Large et al. (1994)), which can be written as

$$\left\langle w'c' \right\rangle = \underbrace{-K(z)\frac{\partial \langle C \rangle}{\partial z}}_{F_D(z)} + F_{ND}(z). \tag{4.1}$$

Here z is the vertical coordinate (negative for the ocean), F_D and F_{ND} are the diffusive and nondiffusive components of the turbulent flux, $K(z)$ is the eddy diffusivity for a passive scalar, w is the vertical velocity of the flow, $\langle C \rangle$ and c' are the average concentration of a passive scalar and its turbulent fluctuation, respectively. Throughout the paper a prime denotes a turbulent fluctuation and $\langle \cdot \rangle$ denotes a Reynolds average that is implemented in practice as a temporal and horizontal average. While KPP is a complete model (providing closure for buoyancy and momentum fluxes), we focus on passive scalars in this manuscript, with the general aim of investigating opportunities for improving KPP in wavy regimes.

Currently there exist many different versions of KPP and they mainly differ in their definition of $K(z)$. While both the shape of $K(z)$ and its modifications due to surface buoyancy fluxes are the same throughout versions (based on Monin-Obukhov similarity theory; MOST), the effect of nonbreaking waves on the magnitude of $K(z)$ varies from model to model (Li et al., 2019). While there is general consensus that the presence of nonbreaking waves (and therefore Langmuir cells (Thorpe, 2004)) should enhance the eddy diffusivity of the flow, there is disagreement on the quantitative aspects (Smyth et al., 2002; Takaya et al., 2010; Van Roekel et al., 2012; Li et al., 2019). The fact that many different studies cannot quantitatively agree on the Langmuir-driven enhancement could mean that merely enhancing $K(z)$ is not an appropriate strategy (Chamecki et al., 2019). With that in mind, we take an alternative approach that takes Langmuir effects into account in both $K(z)$ and F_{ND}.

In all previous versions of KPP F_{ND} is assumed to (i) have the same shape as $K(z)$ and (ii) to depend only on the surface buoyancy fluxes (implying that F_{ND} is designed to model the action of convective plumes specifically). We relax assumption (ii) since it has been shown that nondiffusive

fluxes are affected by Langmuir cells (Chen et al., 2016a; Chamecki et al., 2019) and relax assumption (i) based on recent results for the atmosphere that suggest that the optimal form for F_{ND} can be different from the cubic function that is commonly used in the literature (Chor et al., 2020b).

In order to investigate how to improve KPP in the presence of Langmuir circulation effects, we use the same method used in Chor et al. (2020b). This optimization-based method is capable of estimating profiles for F_D (therefore $K(z)$) and $F_{ND}(z)$ without any imposed shape or scaling. Therefore the main advantage of this method is that is has few assumptions and the shapes and magnitudes of $K(z)$ and $F_{ND}(z)$ are dictated by the data, as opposed to being a function of scalings chosen *a priori*. Furthermore, the optimization procedure is defined with modeling in mind, making its results optimized for modeling purposes by definition.

We use results for $K(z)$ and $F_{ND}(z)$ obtained with the optimization method to investigate the separation between nondiffusive and diffusive fluxes of passive scalars in several OSBL regimes ranging from waveless neutral to combinations of surface buoyancy fluxes and different types of waves. We then use the results to investigate modifications to the KPP formulation (both $K(z)$ and $F_{ND}(z)$ separately) in a way that is optimized for wavy regimes. We consider the main contribution of this work to be the systematic assessment that Langmuir effects are required to be considered in the formulation of nondiffusive fluxes. Furthermore we also propose different shapes for $K(z)$ and $F_{ND}(z)$, which differ noticeably from past versions. We note that our goal is not to introduce a full model (which would need to include formulations for buoyancy and momentum, as well a thorough investigation of stable regimes; both of which are outside the present scope), but to investigate how changes in the formulation of KPP can lead to a model for passive scalar mixing that is better suited for OSBL regimes in the presence of waves.

4.2 Theoretical aspects and definitions

4.2.1 Definitions

Throughout this work, the word “separation” is loosely used to indicate a conceptual partition of the total turbulent flux into different terms, each representing a different physical process. Conversely,

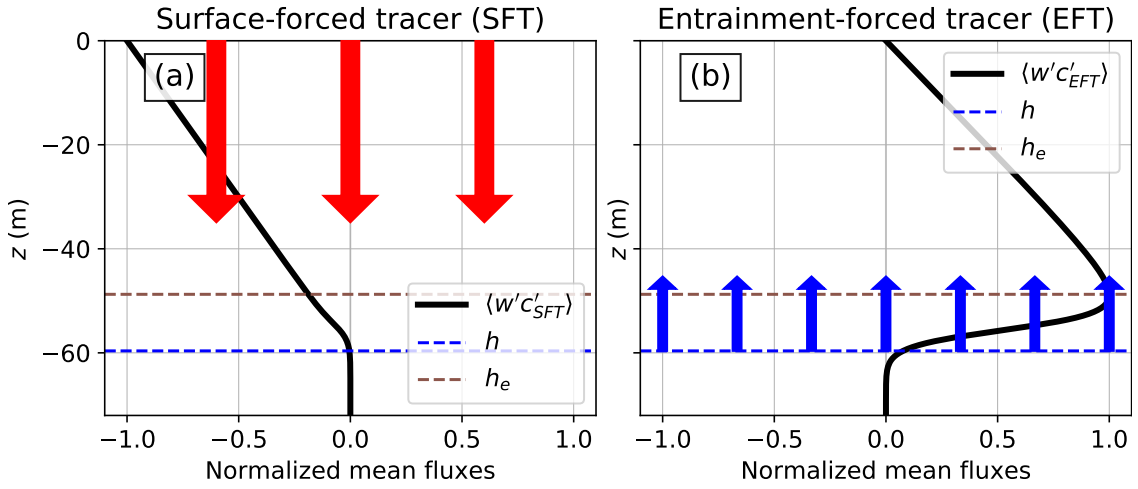

Figure 4.1: Mean turbulent flux profiles for a SFT (a) and an EFT (b). The data for this plot is taken from a convective simulation without surface wind shear or waves, to be described in Section 4.3. Both fluxes are normalized so that the maximum magnitude of the fluxes is unity. Sketched in the figure are also arrows for transport via coherent convective plumes (red arrows) and entrainment processes (blue arrows), and the boundary layer depth h.

we use the word "decomposition" in a more mathematical sense, indicating an exact decomposition of the total flux into different terms. Since it is up for debate whether F_D and F_{ND} represent the turbulent vertical fluxes due to local and nonlocal processes (Zhou et al., 2018), we refer to the first and second terms on the right-hand side of Equation (4.1) (namely F_D and F_{ND}) as diffusive and nondiffusive.

We start by defining two different passive tracers that will be useful in implementing the optimization method: a surface-forced tracer (SFT) and an entrainment-forced tracer (EFT) (Wyngaard et al., 1984; Chor et al., 2020b). A SFT is one which has a source at the surface and no other sources/sinks inside the domain. The subscript SFT is used throughout the paper to indicate quantities associated with this tracer. Figure 4.1a shows the normalized mean turbulent flux profile for a SFT from a convective regime which will be detailed in Section 4.3. SFTs are known to be effectively transported by large convective plumes (Kaimal et al., 1976; Wyngaard et al., 1984; Moeng et al., 1994), which is sketched in Figure 4.1a as red arrows. In the case of wavy oceanic regimes SFTs are also thought to be efficiently transported vertically by Langmuir circulations.

An EFT, on the other hand, is defined as a tracer whose flux into the mixed layer is performed

solely by entrainment processes (the subscript EFT is used to identify quantities associated with it). Vertical transport of this quantity is not as efficient as that of SFTs since there are no large coherent structures emerging from the entrainment layer. Figure 4.1b shows the mean turbulent flux profile for an EFT as a solid black line from the same convective simulation used in Figure 4.1a, where we see a flux maximum at around $z = -50$ m. In practice this flux occurs due to a change in concentration across the entrainment layer, and its mechanism is sketched in Figure 4.1b as blue arrows. It should be noted that, since the transport equations are linear for passive tracers, tracers that are linear combinations of SFTs and EFTs are also solutions of the flow. We also use EFTs to define the maximum entrainment depth h_e, which is the depth at which the turbulent flux of an EFT is at its maximum (depicted as a dashed brown line in Figure 4.1).

While there are many ways to define the boundary layer depth h, it is generally understood that it should represent the maximum depth that OSBL eddies can penetrate into the stratified fluid (Li et al., 2016). In the absence of other sources of instabilities (as is the case with our simulations, described in Section 4.3), OSBL eddies emerge from surface processes. Thus we define h as the depth at which $\left\langle w' c'_{\mathrm{SFT}} \right\rangle$ reaches roughly zero — a negative number for the ocean. We prefer this definition for the sake of simplicity and because it matches very closely to the maximum buoyancy gradient criterion used in Li et al. (2017) for convective conditions, which has its relations to other estimates mapped out (see Figure 1b of Li et al. (2017)). Furthermore, given that turbulent fluxes are linear in quasi steady state conditions, this definition ensures that SFT fluxes do not vary by more than 10% of their surface values in the range $0 \leq z \leq h$, which is generally an accepted definition of the surface layer. The boundary layer depth h can be seen in Figure 4.1 as a dashed blue line. Note that this definition leaves a very small part of the EFT turbulent flux outside of the OSBL, which we consider to be acceptable. From here on we prioritize using the normalized vertical coordinate $\sigma = z/h$ for depth, instead of using z.

We define the turbulent Langmuir number as

$$La = \left(\frac{u_*}{u_0^s} \right)^{1/2}, \tag{4.2}$$

where $u_* = \sqrt{|\left\langle u'w' \right\rangle_s|}$ is the friction velocity ($\left\langle u'w' \right\rangle_s$ is the average momentum flux at the surface) and u_0^s is the Stokes drift at the surface (McWilliams et al., 1997). We also define the stability

parameter Λ as

$$\Lambda = \kappa w_*^3 / u_*^3, \tag{4.3}$$

where κ is the von Karman constant, $w_* = (B_s|h|)^{1/3}$ is the turbulent convective velocity (Kaimal et al., 1976). Here B_s is the surface buoyancy flux and positive values imply a loss of buoyancy. Λ is equivalent to $-|h|/L_o$, where L_o is the Obukhov length, with negative values of Λ indicating stable conditions and positive values indicating unstable conditions. Finally, we define a Langmuir velocity scale as $w_L = (u_*^2 u_0^s)^{1/3}$ (Harcourt et al., 2008).

If we assume that u_0^s is sufficient to characterize the effects of waves (therefore ignoring the penetration of the Stokes drift for simplicity), La and Λ are sufficient to characterize any oceanic regime with only waves, surface wind stress and surface buoyancy fluxes as forcings. Based on this fact we use a modified version of the regime diagram (seen in Figure 4.2) introduced by Li et al. (2005) and Belcher et al. (2012) in which the axes are La and Λ. In previous versions of the diagram, convection was measured with $w_*^3/w_L^3 = La^2\Lambda/\kappa$, which contains an implicit dependence on the Langmuir number which we try to avoid. Furthermore, Λ is common in the atmospheric literature, making the transfer of knowledge between both fields more straightforward. Each of the three regions of the diagram delineate an area where one of the three forcings accounts for at least 25% of the TKE production. Overlapping areas and then dominated by more than one forcing, while non overlapping areas are dominated by only one forcing, as indicated by the labels "Wind" (gray area), "Convection" (pink area) and "Langmuir" (blue area). We also plot the joint probability density function (JPDF) for ocean regimes taken from the set of simulations in Li et al. (2019) as dashed white lines as a guide to assess representativeness of regimes.

4.2.2 Current KPP formulation

Several versions of KPP have been proposed, most of which with different formulations to include wave effects. A thorough review is outside the scope of this manuscript and the reader is directed to Li et al. (2019) for details. The focus of this manuscript is on the formulation of $K(\sigma)$ and $F_{ND}(\sigma)$, and we leave other aspects of KPP (e.g. the estimation of the OSBL depth) untouched.

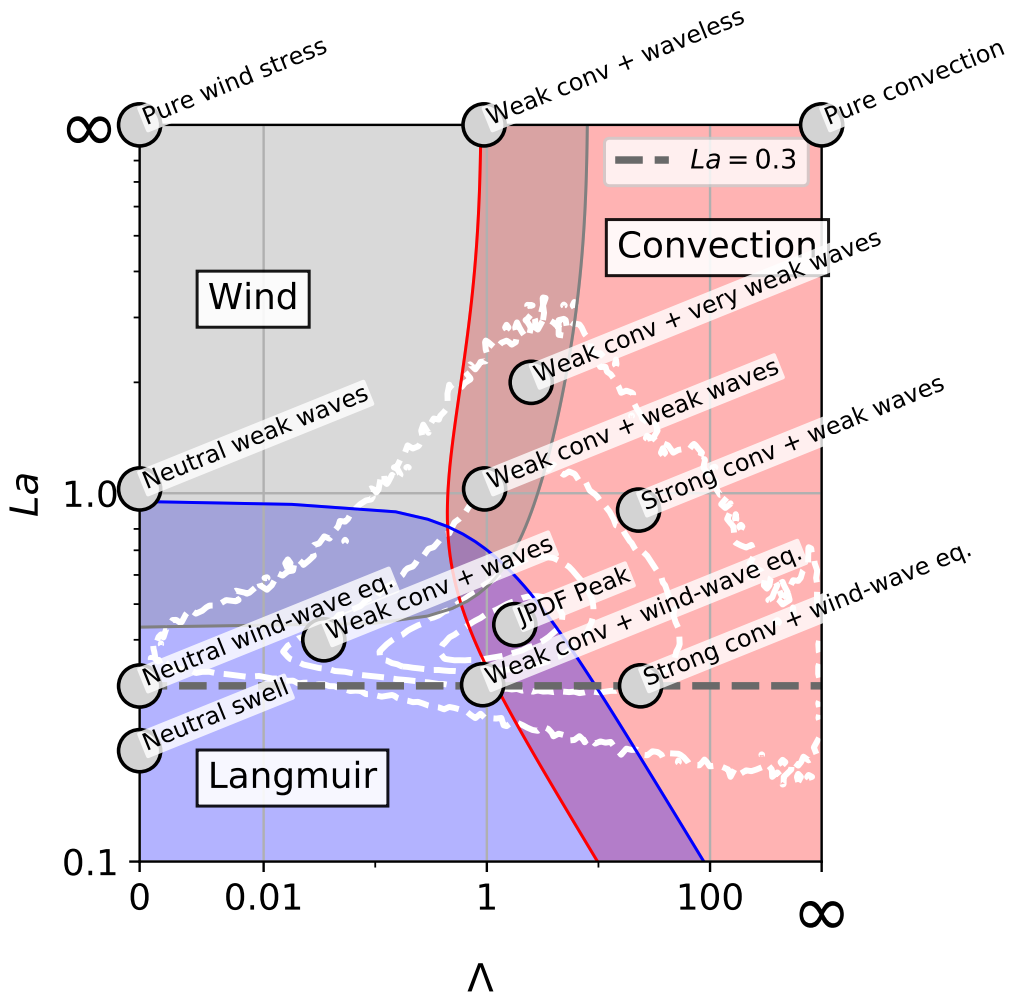

Figure 4.2: All simulations used in this manuscript as gray circles in a La-Λ parameter space. Solid blue, gray and red lines delineate regions where at least 25% of the TKE is produced by Langmuir, surface wind stress and buoyancy fluxes, respectively. Intersection areas are dominated by more than one forcing. Dashed white lines are the JPDF of oceanic regimes from Li et al. (2019) and the dashed gray line marks the line of wind-wave equilibrium. Note that most of the figure is in log-scale except the range $0 \leq \Lambda \leq 1 \times 10^{-2}$, and that the top and right edges represent infinity. Note also that a pure convection simulation (where $\Lambda \to \infty$ and La is not defined since $u_* = u_0^s = 0$) is plotted as if $La = \infty$.

Most formulations of KPP which include wave effects can be written generally as

$$K(\sigma) = u_s(\sigma)\,|h|\,G_k(\sigma), \tag{4.4}$$

$$u_s(\sigma) = \mathscr{E}(La)\,\frac{\kappa u_*}{\phi(z/L_o)}, \tag{4.5}$$

$$F_{ND} = G_s(\sigma)\left\langle w'c'\right\rangle_s H(\Lambda), \tag{4.6}$$

which we will also adopt in this manuscript except for the addition of a few extra dependencies. Here $\kappa = 0.4$ is the von Kármán constant, ϕ is the nondimensional gradient for a tracer in the surface layer according to MOST, $H(\cdot)$ is the Heaviside function, $G_k(\sigma)$ is a nondimensional shape function for $K(\sigma)$ and $G_s(\sigma)$ is a nondimensional shape function for the surface-driven nondiffusive flux. The velocity scale u_s is capped at its value at $\sigma = 0.1$ for unstable conditions according to most implementations (Large et al., 1994). $\mathscr{E}$ is a Langmuir enhancement parameter that depends at least on the Langmuir number La, but may depend on other variables (Smyth et al., 2002). (For example, in the face of the results in Section 4.4 and previous studies, we expect $\mathscr{E}(La,\Lambda)$ (Li et al., 2017).)

In previous versions of KPP, $G_k = G_s/C_* = G_n$, where C_* is a constant and $G_n(\sigma)$ is a cubic function that originated in the atmospheric boundary layer literature:

$$G_n(\sigma) = \sigma\,(1-\sigma)^2.$$

The reasons for a cubic shape are that (i) it is the lowest degree polynomial that can satisfy all four physically-motivated boundary conditions for $K(\sigma)$ (O'Brien, 1970); and that (ii) a cubic shape matches the estimated $K(\sigma)$ profile for a neutral and waveless simulation (Large et al., 1994; Marlatt et al., 2012).

Equations (4.4)-(4.6) indicate that the only adjustment to wavy conditions is a change in the magnitude of the eddy diffusivity $K(\sigma)$, which is given by $\mathscr{E}$, and the difference between different versions of KPP is generally confined to its formulation (vide Figure A1 of Li et al. (2019) for a visual comparison). In particular, previous models include no changes in the shape of $K(\sigma)$, which is given by the cubic profile $G_n(\sigma)$ in every regime, or the shape and magnitude of $G_s(\sigma)$, despite evidence indicating that Langmuir circulations affect nondiffusive vertical transport (Chen et al.,

2016a). Due to the limiting nature of these assumptions and the lack of evidence to support their necessity we relax them here, allowing $G_k(\sigma)$ and $G_s(\sigma)$ to be different from each other and from $G_n(\sigma)$. Furthermore we allow $G_s(\sigma)$ to also depend on Λ and La, for reasons that will become clearer in Section 4.4.

Note that Large et al. (2019) recently introduced a modified version of MOST for the ocean that includes alternative formulations for waveless regimes (different from the ones used for the atmosphere) and new formulations for wavy ones. However, we choose to not use their theory here since we believe that more data is needed in order to validate those results.

4.2.3 Introduction of a new flux partition

We base the analyses of this and the following section on the theory developed in Chor et al. (2020b). Sufficient information to follow the reasoning is given but the reader is directed to the original paper for more details. We consider a three-term flux decomposition without imposing any shape or scaling for $K(\sigma)$ as in Chor et al. (2020b):

$$\left\langle w'c' \right\rangle = -K(\sigma)\frac{\partial \langle C \rangle}{\partial \sigma} + \left\langle w'c' \right\rangle_s G_s(\sigma) + \left\langle w'c' \right\rangle_e G_e(\sigma), \tag{4.7}$$

where $\langle w'c' \rangle_s$ and $\langle w'c' \rangle_e$ are the values of the turbulent flux $\langle w'c' \rangle$ taken at the surface and at h_e, respectively. This is equivalent to setting $F_{ND} = \langle w'c' \rangle_s G_s(\sigma) + \langle w'c' \rangle_e G_e(\sigma)$ in Equation (4.1). Furthermore, $G_s(\sigma)$ and $G_e(\sigma)$ are (as of now) unspecified dimensionless shape functions. $K(\sigma)$, $G_s(\sigma)$ and $G_e(\sigma)$ are assumed to be a function of the flow alone, and knowledge of those three profiles is sufficient to reconstruct the total flux of any passive tracer provided that the fluxes at the vertical boundaries of the OSBL are known. Given our focus on diagnostic analyses, we obtain $\langle w'c' \rangle_s$ and $\langle w'c' \rangle_e$ from LES results.

The main difference between our flux separation (Equation (4.7)) and previous approaches (Equations (4.4)-(4.6)) lies in the fact that we separate the nondiffusive flux F_{ND} into two components: one due to surface fluxes and another due to entrainment processes, while previous approaches only consider surface fluxes. While we show in Section 4.4 that $G_e(\sigma)$ is likely not important in modeling applications, it is critical in decomposing the total flux (Chor et al., 2020b).

4.2.4 Estimating the model components

The goal in this section is to be able to estimate $K(\sigma)$, $G_s(\sigma)$ and $G_e(\sigma)$ assuming no *a priori* scaling or shape for either of them, which introduces the need for three equations. The first step is to consider a SFT and an EFT subjected to the same flow (and thus with the same $K(\sigma)$, $G_e(\sigma)$ and $G_s(\sigma)$). Application of Equation (4.7) to these tracers leads to the following system of equations:

$$\begin{aligned}\left\langle w'c'_{\mathrm{SFT}}\right\rangle = &-K(\sigma)\frac{\partial\langle C_{\mathrm{SFT}}\rangle}{\partial\sigma}+\left\langle w'c'_{\mathrm{SFT}}\right\rangle_e G_e(\sigma)+ \\ &+\left\langle w'c'_{\mathrm{SFT}}\right\rangle_s G_s(\sigma),\end{aligned} \tag{4.8}$$

$$\left\langle w'c'_{\mathrm{EFT}}\right\rangle = -K(\sigma)\frac{\partial\langle C_{\mathrm{EFT}}\rangle}{\partial\sigma}+\left\langle w'c'_{\mathrm{EFT}}\right\rangle_e G_e(\sigma). \tag{4.9}$$

Note that while a SFT has both components of the nondiffusive flux (since there may be a small flux of C_{SFT} through h_e), an EFT only has the entrainment-driven flux, since $\left\langle w'c'_{\mathrm{EFT}}\right\rangle_s = 0$ as a boundary condition.

In order to introduce a third and final equation, we follow Chor et al. (2020b) and use an optimization method that uses only fluxes and mean scalar gradients of SFTs and EFTs in order to close the system of equations. To that end, we introduce a cost function χ to be minimized in an optimization procedure:

$$\chi = G_s^2 + G_e^2. \tag{4.10}$$

This choice of χ is designed to minimize nondiffusive fluxes F_{ND}, which ensures that the flux is fully diffusive in regimes where most of the eddies tend to be small (e.g. in waveless stable or neutral conditions (Jayaraman et al., 2018)). Furthermore, diffusive operators are numerically well-behaved, easy to implement, and ubiquitous throughout the atmospheric community (Corrsin, 1975). Thus, trying to model as much of the flux as possible with a diffusive operator is also a modeling-motivated decision.

The constraint $K \geq 0$ is enforced in the optimization but G_e and G_s are left unconstrained and can become negative. Note that negative values of G_s and G_e imply counter-gradient fluxes, which can happen in OSBLs and so, *a priori*, negative values for the shape functions are plausible.

4.3 Numerical aspects

Table 4.1: Parameters for the simulations used in this paper. All simulations have 256 points in the horizontal direction and 400 points in the vertical direction, with 400 m horizontal and 150 m vertical domain. Note that in Simulation Pure convection the actual Langmuir number is undefined since $u_* = u_0^s = 0$, but we report it as $La \to \infty$ since this value represents waveless conditions and because it makes it possible to plot it in the La-Λ parameter space.

Simulation	u_* (m/s)	B_s (m^2/s^3)	Λ	La	h_e (m)	h (m)
Neutral swell	6.1×10^{-3}	0.00	0.00	0.2	-55.9	-68.2
Neutral wind-wave eq.	6.1×10^{-3}	0.00	0.00	0.3	-57.0	-69.4
Neutral weak waves	7.0×10^{-3}	0.00	0.00	1.03	-50.2	-61.9
Pure wind stress	1.0×10^{-2}	0.00	0.00	∞	-50.2	-61.5
Weak conv + waves	6.1×10^{-3}	5.20×10^{-9}	3.56×10^{-2}	0.4	-54.8	-68.6
Weak conv + wind-wave eq.	7.0×10^{-3}	2.24×10^{-7}	9.39×10^{-1}	0.3	-52.5	-63.4
Weak conv + waveless	7.0×10^{-3}	2.24×10^{-7}	9.67×10^{-1}	∞	-54.4	-65.2
Weak conv + weak waves	7.0×10^{-3}	2.24×10^{-7}	9.78×10^{-1}	1.03	-55.1	-66.0
JPDF Peak	7.0×10^{-3}	4.16×10^{-7}	1.82	0.44	-54.8	-66.4
Weak conv + very weak waves	7.0×10^{-3}	5.54×10^{-7}	2.55	2.0	-56.2	-69.8
Strong conv + weak waves	4.0×10^{-3}	1.04×10^{-6}	2.33×10^{1}	0.9	-52.9	-63.4
Strong conv + wind-wave eq.	4.0×10^{-3}	1.04×10^{-6}	2.41×10^{1}	0.3	-55.1	-65.6
Pure convection	0.0	1.63×10^{-6}	∞	∞	-48.8	-59.6

We use an LES model that was already used successfully in other studies (Chen et al., 2016a; Chor et al., 2018a) to apply the methods described in Section 4.2. The model solves the Craik-Leibovich equations (Craik et al., 1976) and employs a pseudo-spectral scheme in the horizontal directions and a centered finite differences in the vertical direction to solve the flow. The tracer advection is solved using a finite volume scheme with bounded advection (Chamecki et al., 2008). Horizontal boundary conditions are doubly-periodic, the bottom quarter of the domain has a sponge layer to mimic an open boundary, and we apply a rigid-lid approximation on the top boundary. The subgrid scale model used is the Lagrangian-Averaged Scale-Dependent model (Bou-Zeid et al., 2005), which has been shown to reach statistical convergence at coarser resolutions than different subgrid scale closures (Salesky et al., 2017).

We run 13 simulations in total, and each simulation can be characterized by a Langmuir number La and a stability parameter Λ. All simulations are plotted in the La-Λ parameter space in Figure 4.2 as gray circles and have their characteristics listed in Table 4.1. Although there are no simulations in the areas dominated by both wind stress and Langmuir, or dominated by all three forcings simultaneously, we do not consider this to be a problem since the limits of these areas are approximate. Note that for the Pure convection simulation, La is undefined since $u_* = u_0^s = 0$, but we report it as $La \to \infty$ for ease of analysis since this value represents simulations without waves.

In all cases the rotation frequency is $f_0 = 7 \times 10^{-5}\,\mathrm{s}^{-1}$, the domain is $400 \times 400 \times 150$ meters and the grid has 256 points in the horizontal directions and 400 in the vertical direction. The initial potential temperature (θ) profile is well-mixed until approximately $0.85h$ with a constant gradient of $2 \times 10^{-2}\,\mathrm{K\,m}^{-1}$ below it. For ease of the reader, each simulations has a specific name (that can be found in Table 4.1) that gives an approximated brief description of that simulation.

Wave effects were introduced by imposing a Stokes drift profile in each simulation. All simulations that have wave effects are listed in Table 4.2 along with their respective wave characteristics, otherwise the imposed Stokes profile is identically zero. For the sake of control over La and the Stokes profile in general, all waves in this manuscript are monochromatic and thus can be fully defined by setting a wave length L_w and a wave amplitude a (McWilliams et al., 1997). Furthermore the use of monochromatic waves avoids vertical resolution issues from having to resolve the super-exponential decay of broadband wave spectra near the surface.

We minimized the effects of inertial oscillations by setting the initial conditions for velocity to their average over one inertial period (taken from identical simulations on a coarser grid that were run over many inertial periods specifically for this purpose). All of the simulations had a spin-up period of at least 8 convective cycles T_* and the statistics were collected during the next $6T_*$ period or longer. Convective cycles are calculated as $T_* = |h|/\mathrm{MAX}(u_*, w_*, w_L)$.

All simulations also have a SFT and an EFT (both passively transported by the flow) with concentrations C_{SFT} and C_{EFT} which have different initial and boundary conditions. Entrainment fluxes are accomplished by imposing different initial concentrations for the mixed layer and above it. Thus, EFTs are initialized with zero concentration until approximately $0.9h$ and nonzero

Table 4.2: Wave parameters for simulations used in this paper that include wave effects. For all other simulations the Stokes drift is identically zero. D_{st} is the e-folding depth of the Stokes profile, given by $D_{st} = L_w/(4\pi)$ for monochromatic wave spectra.

Simulation	a (m)	L_w (m)	u_0^s (m/s)	D_{st} (m)
Neutral swell	2.0	1.2×10^2	1.5×10^{-1}	9.5
Neutral wind-wave eq.	8.0×10^{-1}	6.0×10^1	6.8×10^{-2}	4.8
Neutral weak waves	2.5×10^{-1}	6.0×10^1	6.6×10^{-3}	4.8
Weak conv + waves	6.0×10^{-1}	6.0×10^1	3.8×10^{-2}	4.8
Weak conv + wind-wave eq.	8.5×10^{-1}	6.0×10^1	7.7×10^{-2}	4.8
Weak conv + weak waves	2.5×10^{-1}	6.0×10^1	6.6×10^{-3}	4.8
JPDF Peak	5.8×10^{-1}	6.0×10^1	3.6×10^{-2}	4.8
Weak conv + very weak waves	1.3×10^{-1}	6.0×10^1	1.7×10^{-3}	4.8
Strong conv + weak waves	2.2×10^{-1}	6.0×10^1	4.9×10^{-3}	4.8
Strong conv + wind-wave eq.	6.5×10^{-1}	6.0×10^1	4.5×10^{-2}	4.8

concentration below. SFTs are initialized with a $C_{\mathrm{SFT}} = 0$ throughout the domain. EFTs have a zero-flux boundary condition at the surface, while we impose a nonzero surface mass flux into the OSBL for SFTs. Both tracers have horizontally periodic boundary conditions. Throughout this paper all tracer fluxes are normalized either by their value at the surface (for SFTs) or by their entrainment fluxes (for EFTs).

4.4 Results

After the method is applied and results are obtained for $K(\sigma)$, $G_s(\sigma)$ and $G_e(\sigma)$, F_D and F_{ND} can be calculated. In this section we present the results for F_D and F_{ND} based on our decomposition, and then move on to discuss the eddy diffusivity and shape function profiles.

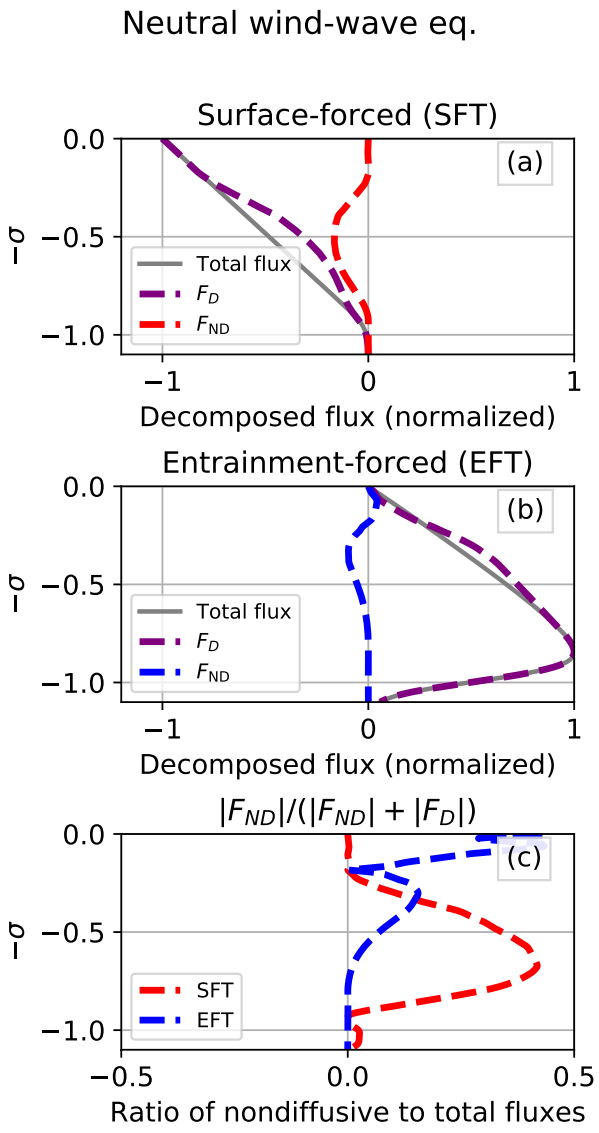

Figure 4.3: Flux decomposition for Simulation Wind-wave eq. Panels a and b show the decomposition for an SFT and an EFT, respectively. Panel c shows the metric $|F_{ND}|/(|F_{ND}|+|F_D|)$. The absolute value operators are used to account for the cancellations that occur for the EFT.

4.4.1 Diffusive/nondiffusive flux decompositions

Figure 4.3 shows the turbulent flux decomposition for Simulation Neutral Wind-wave eq., which is similar to the main simulation in McWilliams et al. (1997) but with $\Lambda = 0$. Panel a shows results for a SFT and it is evident that SFT nondiffusive fluxes are significant in this regime, accounting for around 40% of the total turbulent flux in the middle of the OSBL (see Figure 4.3c, which shows the metric $|F_{ND}|/(|F_{ND}| + |F_D|)$, which simplifies to the ratio of nondiffusive to total fluxes whenever F_{ND} and F_D are both positive). Although not shown for brevity, it is important to mention that our optimization method correctly captures the physical behavior in regimes known to not need nondiffusive fluxes (e.g. the Pure wind stress simulation, shown in Appendix D, and the neutral simulation of Chor et al. (2020b) are diagnosed by our method to have negligible nondiffusive fluxes). With that in mind, since there is no convection in this regime, the nondiffusive term visible in Figure 4.3a must be the product of Langmuir circulations. Since the calculation of these fluxes assumes a minimization of the nondiffusive fluxes (see discussion in Section 4.2.4), this is evidence that nondiffusive fluxes *must* be present when modeling regimes with nonbreaking waves. Furthermore, SFT fluxes in the surface layer are fully diffusive, as expected from MOST. Finally, EFTs have very little nondiffusive fluxes in this regime, indicating a lower importance of nondiffusive entrainment processes.

Throughout all simulations in this work (shown in Appendix D), repeated patterns are: (i) fully diffusive fluxes in the surface and entrainment layers for SFTs independent of the regime; (ii) significant nondiffusive SFT fluxes in the middle of the OSBL whenever large eddies are present (either due to convection or nonbreaking waves) with a peak close to the middle of the OSBL; and (iii) little contribution from nondiffusive fluxes for EFTs. Whenever present, the shapes of nondiffusive fluxes are also similar to those in Figure 4.3. Thus, in order to avoid analyzing all simulations with this level of detail, we take a bulk approach and define

$$R_F = \frac{\int_0^1 |F_{ND}|\, d\sigma}{\int_0^1 \left(|F_D| + |F_{ND}|\right) d\sigma} \tag{4.11}$$

which indicates the importance of nondiffusive fluxes relative to total turbulent fluxes. R_F is bounded between 0 (when fluxes are fully diffusive) and 1 (when fluxes are fully nondiffusive). It is worth

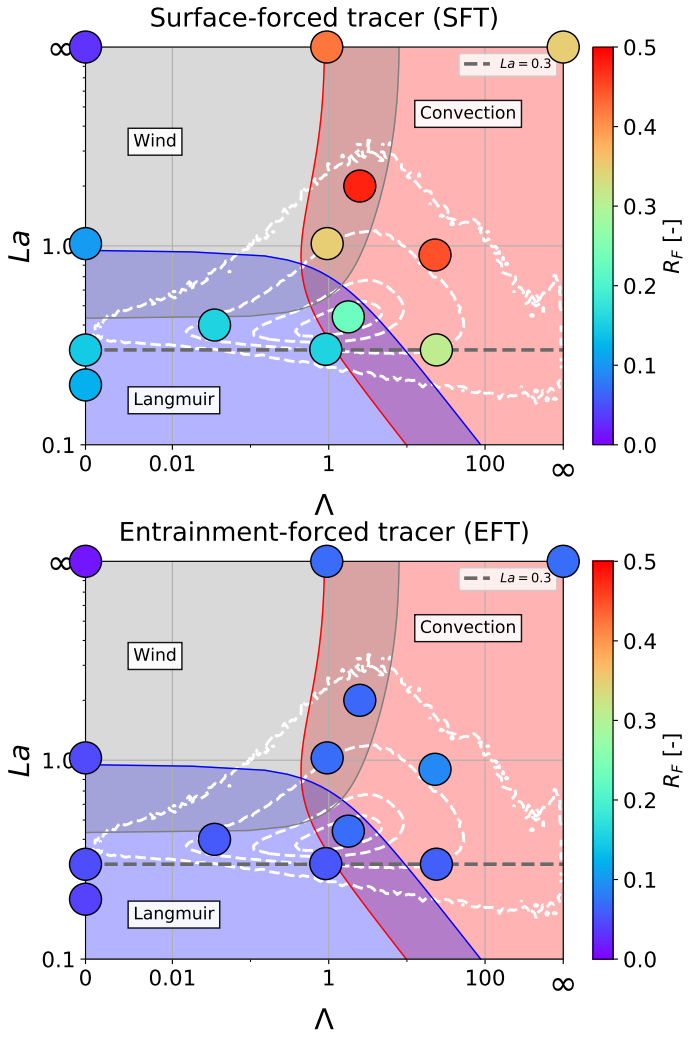

Figure 4.4: Ratio of nondiffusive to total fluxes R_F, defined in Equation (4.11). Note that the Λ axis has a linear scale from 0 to 0.01 and a log scale everywhere else for convenience.

noting that, due to the possibility of flux components to have opposite signs, interpreting R_F as a percentage of fluxes is not precisely correct. However, as this happens very rarely for SFTs and for small percentage of the OSBL for EFTs, this is a valid approximation.

Results for R_F are shown in Figure 4.4a for SFTs and Figure 4.4b for EFTs. It becomes immediately clear that R_F values for EFT are much lower than SFTs throughout the parameter space, with the pure wind stress case being the only exception. The magnitude of R_F for EFTs suggests that entrainment-drive nondiffusive transport is always smaller than 10% of the total flux (the maximum value of R_F for EFTs is 0.09).

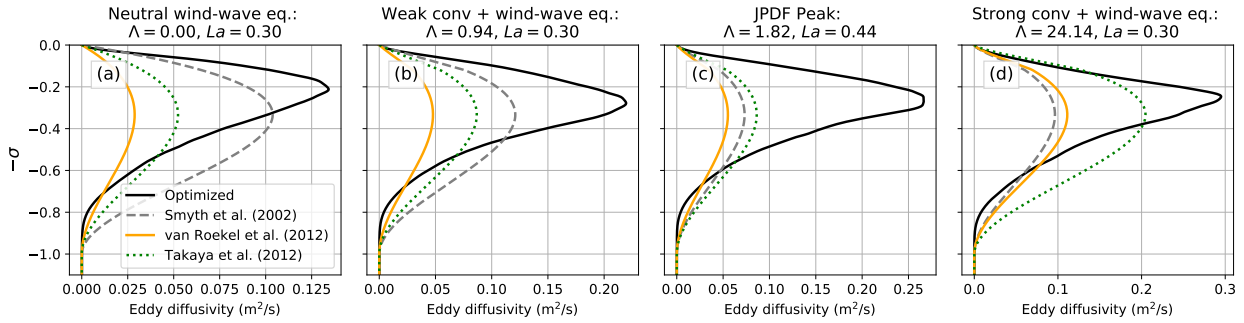

Figure 4.5: Eddy diffusivity profiles $K(\sigma)$ for some of the simulations in this manuscript. Black lines are results from our optimization method, gray lines represent the model by Smyth et al. (2002), green lines represent the model by Takaya et al. (2010) and orange lines represent the model by Van Roekel et al. (2012) with aligned wind and waves.

R_F values for SFTs, however, indicate that surface-driven nondiffusive transport can account for approximately 50% of the total flux (the maximum value is 48% for simulation Weak conv + very weak waves). In fact, every simulation that is not the Pure wind stress simulation ($La \to \infty$, $\Lambda = 0$) has more than 10% of nondiffusive fluxes. The fact that nondiffusive fluxes are important even when minimizing them points to their indispensability in KPP-like models. In particular, we see a significant presence of nondiffusive fluxes for neutral simulations with waves (corresponding to the line $\Lambda = 0$ on the left edge of the parameter space). As an example, F_{ND} accounts for 15% of the total flux in Simulation Neutral Wind-wave Eq. This value is not as large as R_F for the Pure Convection simulations (approximately 35%), but it is significant. Since our method minimizes F_{ND}, this is the lower bound for nondiffusive fluxes, which points to the need of considering waves in the formulation of F_{ND}.

Furthermore, it is interesting to see that the peak values of R_F for SFTs happen when there are weak waves and moderate convection, which has higher values of R_F than the Pure convection simulation. This points to some interaction between Langmuir circulations and convective plumes, even though the flux decomposition profiles show no qualitative difference from the other regimes (see Figure D.1 in Appendix D).

4.4.2 Eddy diffusivity shapes

Figure 4.5 shows $K(\sigma)$ for selected simulations obtained with our optimization method (black) along with estimates from different models in the literature for comparison (colored lines). The cases that are not shown follow similar patterns. Note that there are mismatches between different models whenever waves are significant, which is evidence of the lack of consensus on the enhancement term $\mathscr{E}$. Furthermore, model predictions differ from our optimized results. This is true for both magnitude and shape of $K(\sigma)$ in most cases, suggesting that improvements on these models are possible.

Considering the profiles shown in Figure 4.5 and the rest of our results (not shown) we see that the eddy diffusivity shapes are very similar to each other whenever waves are present, which does not happen for regimes without waves. This can be seen in Figure 4.6a where we show $K(\sigma)$ normalized by its integral over σ (in order to focus on the shapes as opposed to the magnitudes) for all regimes with waves. It is clear that all shapes in wavy regimes are similar to each other, and that they are different from the community-standard cubic function $G_n(\sigma)$. We also plot the same quantity for regimes without waves in Figure 4.6b for reference, where a clear mismatch between them is evident. (Although not labeled, Figure 4.6b shows results for the Pure wind stress Simulation, where $K(\sigma)$ from our method closely resembles the cubic shape that is known to represent fluxes well in this case.)

Results in Figure 4.6a-b indicate that the presence of waves changes the eddy diffusivity shapes in a way that does not depend on either the precise characteristics of the waves or the strength of the convection. This rough collapse into one predictable shape makes it possible to seek a universal fixed curve for KPP in wavy situations (as opposed to seeking curves that change shape with different regime characteristics) that should be different from the cubic shape. This is further explored in Section 4.6.

4.4.3 Nondiffusive shape functions

Results for the surface-driven nondiffusive shape functions $G_s(\sigma)$ are shown in Figure 4.7, where the line colors follow those of Figure 4.5. Our results indicate that the magnitude of $G_s(\sigma)$ can

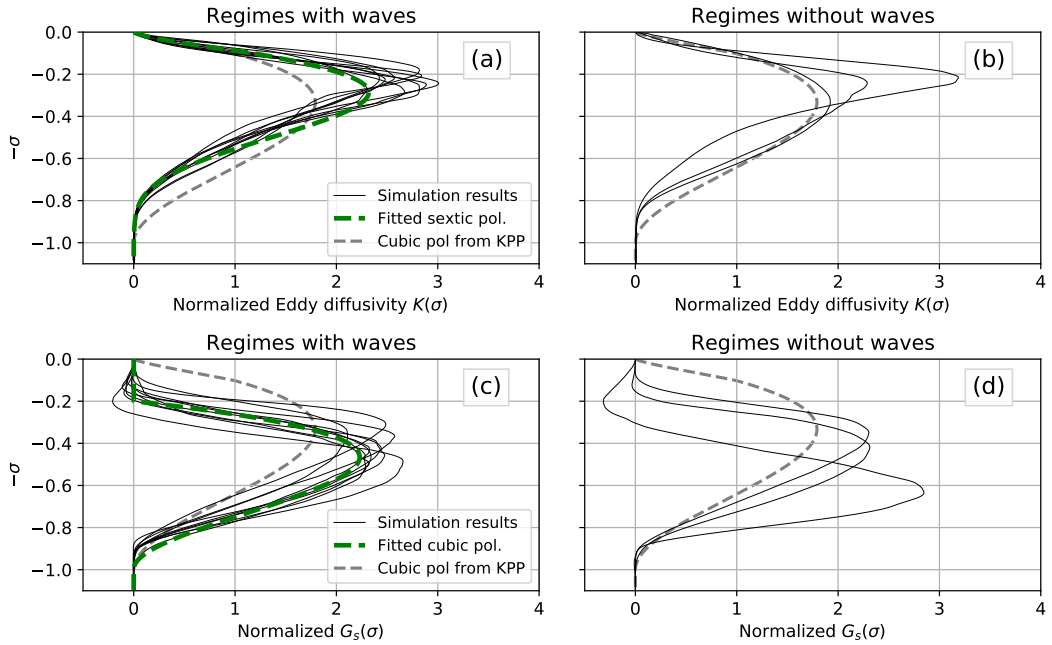

Figure 4.6: Eddy diffusivity $K(\sigma)$ (panels a and b) and nondiffusive surface shape functions $G_s(\sigma)$ (panels c and d) normalized by their integral over σ. Black lines are results from all regimes in this paper using our optimization method. Dashed gray lines are the cubic shape function $G_n(\sigma)$ for reference and dashed green lines represent the formulations introduced in Section 4.6.

change between regimes, which is something previous KPP versions do not consider. Figure 4.7a also indicates that the effect of Langmuir circulations on $G_s(\sigma)$ is also significant, which is expected given the flux partition of Figure 4.3.

Furthermore, it appears that the shapes of $G_s(\sigma)$ obtained from our method are also different from the commonly-used cubic shape in KPP-like models. In order to better explore that, we also plot $G_s(\sigma)$ for the wavy cases in Figure 4.6c where results are normalized by their integral over σ in order to focus on shapes. Gray lines are the currently-used cubic shape $G_n(\sigma)$ for reference. There is clearly significant difference between the model profile and our optimization results, especially close to the surface. While the cubic profile produces significant amount of nondiffusive fluxes in the surface layer, profiles from our method are approximately zero in that region, which is in accordance with MOST. Furthermore, the similarity of profiles in wavy regimes once again suggests that the presence of waves collapses profile shapes, creating a somewhat wave-universal shape that does not depend on other characteristics of the flow. We show $G_s(\sigma)$ for waveless regimes in Figure 4.6d for reference, where the mismatch between regimes is clear.

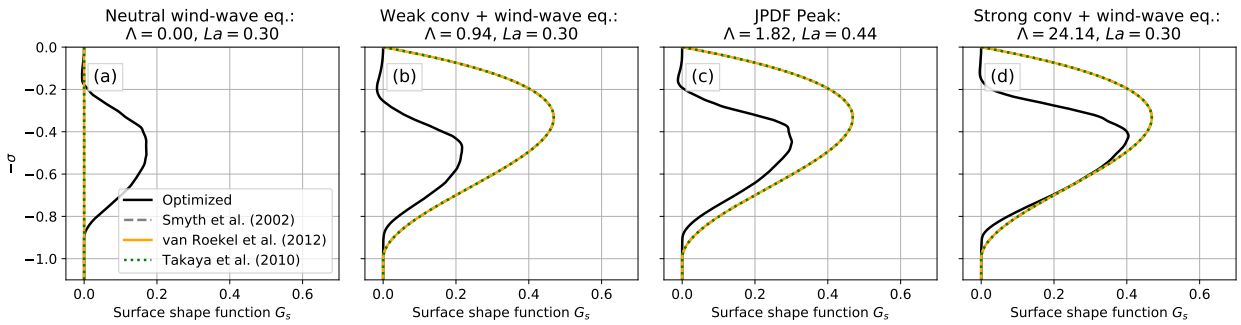

Figure 4.7: Nondiffusive surface shape functions $G_s(\sigma)$ for all simulations. Black lines are results from our optimization method and gray lines represent the cubic shape function used in previous models (in this case $G_s(\sigma) = C_* G_n(\sigma)$).

4.4.4 Eddy diffusivity magnitudes

It is useful to separate our eddy diffusivities in a shape and a scaling, according to previous models. We focus for now on wavy regimes and, based on Equations (4.4)–(4.5), write

$$\mathscr{G}_l^j(\sigma) = A^* \, \phi(z/L_o) \frac{K(\sigma)}{\kappa u_* |h|}, \tag{4.12}$$

where $\mathscr{G}_l^j(\sigma)$ is an empirical shape function for wavy regimes to be calculated for each simulation j, A^* is a constant that is used solely for the calculation of $\mathscr{G}_l^j(\sigma)$, described next, and the right-hand side is specific to each individual simulation j (the dependence on j of each variable is omitted for brevity). In this equation, $K(\sigma)$ is the eddy diffusivity estimated via our optimization procedure specifically.

A^* is calculated separately for each simulation so that $d\mathscr{G}_l^j(\sigma)/d(\sigma) = 1$ at the surface (calculated with a third order finite difference), which is a necessary condition for MOST. We then average the results to arrive at a final shape $G_l(\sigma)$ as

$$G_l(\sigma) = \frac{\sum_j \mathscr{W}^j(\sigma) \mathscr{G}_l^j(\sigma)}{\sum_j \mathscr{W}^j(\sigma)}, \tag{4.13}$$

where $\mathscr{W}^j(\sigma) = |dC^*_{\mathrm{SFT}}/d\sigma| + |dC^*_{\mathrm{EFT}}/d\sigma|$ is a weighting function ($dC_i^*/d\sigma$ is the mean gradient of the i-th scalar normalized such that the maximum gradient is unity in the OSBL for any given simulation). $\mathscr{W}^j(\sigma)$ depends both on the simulation and on the depth, and it generally gives more

weight for values close to the surface and close to $\sigma = 1$, since these regions generally exhibit larger gradients. The rationale is that the precise value of $K(\sigma)$ (and therefore $G_l(\sigma)$) is more important in regions with large gradients. Equation (4.13) only uses simulations j that have waves (finite La). With this decision $G_l(\sigma)$ will be particularly suitable for wavy simulations at expense of some accuracy for waveless ones. Since waveless regimes are uncommon in the ocean we believe this to be a well-founded choice, with the possible caveat of ice-covered regions.

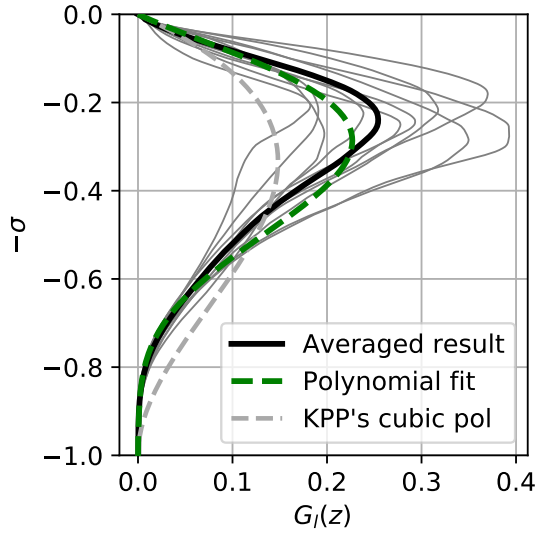

Figure 4.8: Eddy diffusivity shape functions for wavy conditions $G_l(\sigma)$. Diagnosed shapes for each individual wavy regime according to Equation (4.12) are shown in solid gray lines. Solid black line is the weighted average (using $\mathscr{W}$) of these shapes and dashed green line is a sixth-order polynomial fit of the weighted average. KPP's original cubic polynomial is shown as a dashed gray line for reference.

The normalized shapes for the wavy simulations (solid gray lines) and their average (solid black line) are shown in Figure 4.8. There is some difference in magnitude of the diagnosed curves between simulations due to our calculation of A^*. Given that our estimate of A^* is based on surface layer arguments (MOST), this may indicate a possible inconsistency between surface layer and bulk OSBL scalings (Chor et al., 2020b). However, a model that includes such an extra dependence on regimes in the shape functions is outside the scope of the present work as it is likely to add a significant level of complexity. In order to retain compliance with the canonical case of neutral waveless oceans (wind-stress-dominated regime) in the analyses to follow, we postulate an

alternative formulation for $G_k(\sigma)$ as

$$G_k(\sigma) = \begin{cases} G_n(\sigma) & \text{if } \Lambda < 1 \times 10^{-3} \text{ and } La > 10, \\ G_l(\sigma) & \text{otherwise.} \end{cases} \tag{4.14}$$

These thresholds for La and Λ are somewhat arbitrary and more simulations are needed to assess them (as well as potential impacts of sharp thresholds on prognostic models). However, since this region of the La-Λ parameter space is far from the bulk of the JPDF, we do not focus on precise values for now.

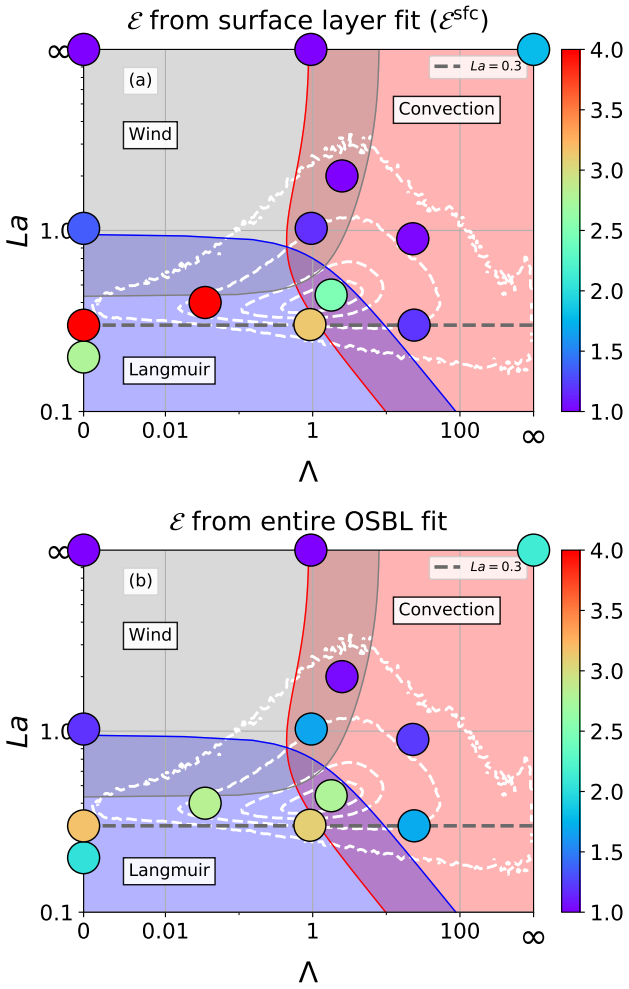

Figure 4.9: $\mathscr{E}$ estimated by fitting Equation (4.5) against $K(\sigma)$ obtained via the optimization method. Panel shows results for the fit using only the surface layer and panel b shows results for the fit using the entire OSBL.

With $G_k(\sigma)$ defined we can again base the next steps on Equation (4.5), of which the only unknown is $\mathscr{E}$. We set out to estimate $\mathscr{E}$ by fitting Equation (4.5) with the shape function $G_k(\sigma)$ as defined in Equation (4.14) against the eddy diffusivity calculated via our optimization method (shown for selected cases in Figure 4.5). We do this in two different ways: (i) we fit $\mathscr{E}$ based only on data for the surface layer and (ii) we fit $\mathscr{E}$ based on the entire OSBL. The rationale behind (i) is to focus on the modification of MOST relations by $\mathscr{E}$ which acts to decrease vertical gradients near the surface (given in nondimensional form by $\phi(z/L_o)$) through stronger vertical mixing. The reasoning behind (ii) is to focus on the enhanced vertical mixing due to large eddies that span approximately the entire OSBL. Note that $\mathscr{E}$ estimated with approach (i) does not relate to A^*, which was estimated simply to impose that $G_l(\sigma)$ obey the boundary condition at the surface required by MOST.

Results for approaches (i) and (ii) are shown in Figure 4.9 panels a and b, respectively. In both cases the largest enhancements to the eddy diffusivity happen for regimes that fall in the Langmuir-dominated region, as expected. Larger magnitudes are found when focusing on the surface layer for fitting (approach (i)), coinciding with the region where the Stokes drift has the largest shear. Our results (especially in Figure 4.9a) indicate that $\mathscr{E}$ depends on the stability given by Λ. This feature had already been noticed by Li et al. (2017) and the only implemented model that takes this into account is the one by Smyth et al. (2002). Furthermore, note that clearly $\mathscr{E} > 1$ for the Pure convection regime in both panels ($\Lambda \to \infty$, $La \to \infty$), which indicates a possible inconsistency of MOST scaling (which is derived from atmospheric measurements) with OSBL results under strongly convective conditions.

Note that in both cases there is a general trend of $\mathscr{E}$ to increase with decreasing La, which is expected given that this indicates stronger Langmuir circulations. However, in both cases the trend is broken for the Neutral swell case. This may be due to the fact that in this case the Stokes drift penetration is larger than in other regimes (by approximately a factor of two; see Table 4.2) which translates to a smaller shear at the surface. However, nonmonotonic dependence on La has been observed before for swell cases, albeit for eddy viscosity (McWilliams et al., 2014). It is possible that the use of the surface layer Langmuir number (Harcourt et al., 2008) would mitigate this effect, but this investigation is left for future studies.

In the rest of the paper we focus on $\mathscr{E}$ obtained using only the surface layer, hereafter referred

to as $\mathscr{E}^{\text{sfc}}$, since we would like surface fluxes to be better represented. Furthermore, it is easier to compare $\mathscr{E}^{\text{sfc}}$ from this method with results from the literature since, given our constraint on $G_l(\sigma)$ to have unit derivative at the surface, $G_l(\sigma)$ and $G_n(\sigma)$ do not differ by much in that region (see for example Figure 4.6). Differences in the enhancement using the entire OSBL between our results and previous literature might simply be due to the change in shape.

4.5 Implications for modeling

A few key differences become clear when comparing our results to the curves used by models. The first being that eddy diffusivity magnitudes from models generally underestimate the magnitudes from our method (see Figure 4.5). Since our method is based on the minimization of nondiffusive fluxes (and thus maximization of diffusive ones) this does not constitute a violation in any way, but it does mean that models could take more advantage of diffusive fluxes. Much of the difference in $K(\sigma)$ between models and our results appear in the middle of the OSBL and seem to be related to a difference in shape that occurs between different regimes. In particular, whenever waves are present $K(\sigma)$ assumes a shape that is clearly different from a cubic polynomial (see Figure 4.6a, which shows that our shapes have a more pronounced peak that is closer to the surface when compared to a cubic polynomial). This implies that much of the discrepancies between our results and models can be reduced in a straightforward way simply by considering an alternative shape in wavy regimes. Note that, while the eddy diffusivity shape for the pure wind stress regime is well established (and well reproduced by our optimization method), shapes for other waveless regimes appear to be inherently different (see Figure 4.6b), making the problem of modeling $K(\sigma)$ in these cases more difficult. However, given that such regimes are usually not found in the ocean, with the possible exception of ice-covered regions (see JPDF in regime diagram in Figure 4.2), we need not worry about these regimes for immediate modeling purposes.

Our results also suggest that the magnitude of $G_s(\sigma)$ should depend on the magnitude of surface buoyancy fluxes, and not just its presence, as is common with previous models (see Equation 4.6 and Figure 4.7). Furthermore, based on the regimes on the $\Lambda = 0$ line in Figure 4.4, $G_s(\sigma)$ should also depend on whether or not the ocean has waves. Some studies have identified influences on

nondiffusive transport in KPP-like models whenever Langmuir circulations are present (Yang et al., 2015; Chamecki et al., 2019) and our results confirm that in a more systematic manner since profiles for $G_s(\sigma)$ are, through the definition of our optimization method, as small as they can be. Thus, the fact that $G_s(\sigma)$ is significant even without destabilizing buoyancy fluxes (e.g. Figure 4.7a) indicates that nondiffusive fluxes *must* be present in order to fully model the effects of Langmuir circulations.

Moreover, $G_s(\sigma)$ shapes obtained by our method are clearly different from the cubic shape used by previous models, especially in the surface layer. This is no surprise since the assumption of a cubic shape for $G_s(\sigma)$ does not follow any physical arguments and our results further indicate that the shapes of $K(\sigma)$ and $G_s(\sigma)$ need not be the same. Finally, our results point to $G_e(\sigma)$ contributions being small throughout the parameter space (see Figure 4.4), which justifies the community practice of neglecting that flux component in KPP.

In summary, these results indicate that (i) a change in the function $G_k(\sigma)$ for another shape in wavy regimes may be beneficial, (ii) $G_s(\sigma)$ should change magnitude depending on La and Λ, (iii) $G_s(\sigma)$ should also have a different shape than the cubic shape $G_n(\sigma)$ and (iv) $G_e(\sigma)$ may be neglected for now. We will explore these modifications in the next Section 4.6.

4.6 Implementing changes to KPP for passive tracers

Based on the discussion from the previous section we consider modifications to existing wave-aware KPP formulations and explore their impact on modeled fluxes.

4.6.1 Modeling the eddy diffusivity

For the purposes of implementation we fit the averaged $G_k(\sigma)$ with a polynomial. The lowest degree polynomial that produces reasonable results is a sextic polynomial, which has 3 extra degrees of freedom in comparison with the commonly used cubic function $G_n(\sigma)$. The polynomial fit satisfies the usual constraints for KPP, namely $G_k(\sigma = 0) = G_k(\sigma = 1) = 0$, $dG_k/d\sigma = 1$ at the surface and $dG_k/d\sigma = 0$ at $\sigma = 1$ (O'Brien, 1970). The result of the fit can be seen in Figure 4.8 as a dashed

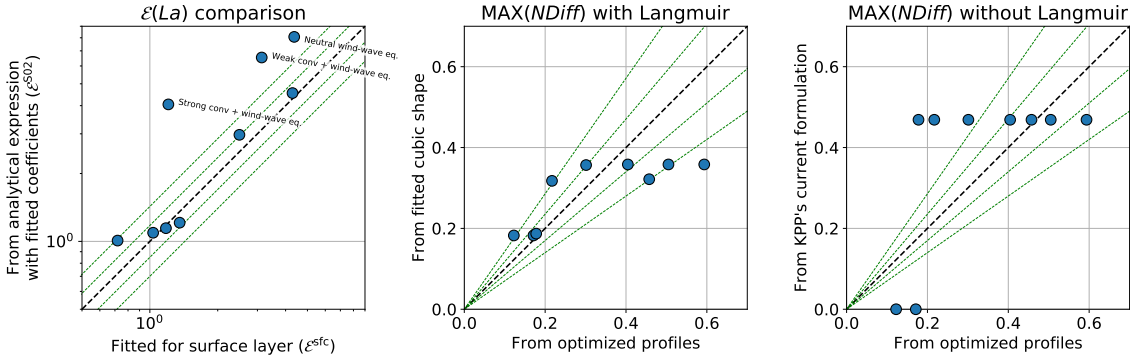

Figure 4.10: Fits for the enhancement factor $\mathscr{E}$ (panel a) and nondiffusive component shape function $G_s(\sigma)$ as quantified by their maximum value in the OSBL (panel b). A comparison with the current formulation used by KPP is shown in panel c for reference. Also shown are the 1:1 line (dashed black) and lines corresponding to 15 and 30% error (dashed green).

green line and its formula is

$$G_l(\sigma) = \sigma(1-\sigma)^2\left[1 + c_4\sigma + c_5(\sigma+\sigma^2) + \right. \tag{4.15}$$

$$\left. c_6(3\sigma + 2\sigma^2 + \sigma^3)\right], \tag{4.16}$$

with the fitted coefficients $c_4 = 47$, $c_5 = -35$ and $c_6 = 9$.

It is useful to have a model for $\mathscr{E}$. Based on our discussions we choose the formulation by Smyth et al. (2002) since it is the only one that includes the observed dependence on Λ:

$$\mathscr{E}^{\mathrm{S02}} = \left[1 + \frac{C_{w0}}{La^{2\alpha}}\left(\frac{1}{1+\frac{\beta}{\kappa}\Lambda}\right)^{l}\right]^{1/\alpha}. \tag{4.17}$$

In the original formulation $\alpha = l = 2$, $C_{w0} = 0.15$ and $\beta = 0.6$[1]. In this manuscript we fit the coefficients to match the enhancement factors reported in Figure 4.9a ($\mathscr{E}^{\mathrm{sfc}}$). We use only wavy simulations excluding the swell case, since its nonmonotonic behavior cannot be captured by this simple formulation. Our fitted values are $\alpha = 1/2$, $C_{w0} = 0.36$, $l = 0.9$ and $\beta = 0.21$ which will be used from here on.

Results for this fit can be seen in Figure 4.10a, which shows $\mathscr{E}$ fitted for the surface in the

[1]In Smyth et al. (2002) the convective velocity w_* is defined differently from Equation (4.17), which would make β have a different value than what we report here. However this appears to be a typo since none of the other equations in their manuscript reflect that alternative definition and we maintain the values as reported. In any case, this difference does not affect our results since Equation (4.17) is only used here with fitted coefficients.

horizontal axis and its estimate using Equation (4.17) in the vertical axis along with reference lines for no error (1:1 line), 15 and 30% error. Only simulations with waves are shown. While most of the simulations fall within the 15% error region, there are simulations with larger error. In particular simulation Strong conv + wind-wave eq. is especially far from the 1:1 line, along with the two other regimes with $La = 0.3$. Given the level of complexity of the variation in Figure 4.9a it is not surprising that there are such errors in the analytical formulation, but most of the regimes have an agreement reasonable enough to allow us to move forward.

4.6.2 Modeling the surface nondiffusive shape function

According to the previous discussions, the nondiffusive shape function should have a dependence on waves and surface buoyancy fluxes (characterized by La and Λ, respectively). This dependence can be introduced in a simple way as

$$G_s(\sigma) = [\text{Langmuir} + \text{Convection}]\, g_s(\sigma) \tag{4.18}$$

$$\text{Langmuir} = \mathscr{L}_1\ [1 - H(La - La_c)] \tag{4.19}$$

$$\text{Convection} = \mathscr{C}_1\ \text{erf}\,[\mathscr{C}_2(\Lambda - \Lambda_c)]\,, \tag{4.20}$$

where we impose beforehand that $\Lambda_c = \kappa$ (which is when $u_* = w_*$). Furthermore, since we do not have enough information about the transition between no waves and weak waves, we somewhat arbitrarily choose a step transition which happens for $La_c = 10$ ($u_* = 100\,u_0^s$). Based on $G_s(\sigma)$ profiles for wavy regimes (see Figure 4.6c), we choose g_s as being a piecewise function that can be written with the aid of a Heaviside function as

$$g_s(\sigma) = (\sigma - 0.2)(1-\sigma)^2 H(\sigma - 0.2), \tag{4.21}$$

valid for $0 \leq \sigma \leq 1$. The curve can be seen normalized in Figure 4.6c (dashed green line).

A fit of Equations (4.18)-(4.21) using all wave regimes yields the values $\mathscr{L}_1 = 1.70$, $\mathscr{C}_1 = 3.06$ and $\mathscr{C}_2 = 1.27$. A comparison between diagnosed $G_s(\sigma)$ from our optimization method and from Equations (4.18)-(4.21) is shown in Figure 4.10b, where the chosen measure is the maximum value of $G_s(\sigma)$ in the OSBL (which in our formulation happens at around $\sigma \approx 1/2$). Roughly half of the

regimes fall within the 15% error lines. In particular our formulation severely underpredicts $G_s(\sigma)$ for Simulation Weak conv + very weak waves, which has significant nondiffusive turbulent flux even with weak waves and convection.

The values of $\mathscr{L}_1$ and $\mathscr{C}_1$ suggest that waves can have an impact on nondiffusive fluxes that is approximately half of that for strong convection. For a representative oceanic regime (say Simulation JPDF Peak, where Equations (4.18)-(4.21) and our optimization differ by only 16% on their estimate of $G_s(\sigma)$), these values predict that almost 40% of the nondiffusive fluxes are due to Langmuir circulations, pointing to the need to include this effect in KPP.

For the sake of reference we also compare our optimized profiles with the currently-used KPP formulation in Figure 4.10c. The horizontal axis shows the maximum $G_s(\sigma)$ from our optimized profiles and the vertical axis shows the same measure for KPP. A comparison between panels b and c reveals that including Langmuir effects in the formulation for $G_s(\sigma)$ (panel b) significantly improves results, further indicating importance of Langmuir circulations for nondiffusive fluxes.

4.6.3 Comparisons between different formulations

We show results for the turbulent flux using the KPP formulation with the fitted coefficients $\mathscr{E}^{\text{sfc}}$ in Figure 4.11 for Simulation JPDF Peak. Left panels show results with our modified formulations for $G_k(\sigma)$ and $G_s(\sigma)$, while right panels show results using the original formulation for these profiles, as used in Smyth et al. (2002). Also shown are the results from LES using our optimized decomposition. Top panels show fluxes for SFTs, where it is clear that much of the error happens in the surface layer due to the parameterization of the diffusive fluxes. The diffusive term also artificially produces a bump in the entrainment layer that is small using our proposed formulation but quite significant when using the original KPP formulation. It is challenging to represent diffusive fluxes in these regions due to the large gradients, which enhances small errors in the eddy diffusivity. However, the middle of OSBL is generally well-represented by the diffusive term in both formulations, although the alternative formulation proposed here is more accurate. The nondiffusive terms match quite well using our new formulation that takes Langmuir into account (panel a), but there is significant mismatch using the original KPP formulation (panel b), especially in the surface

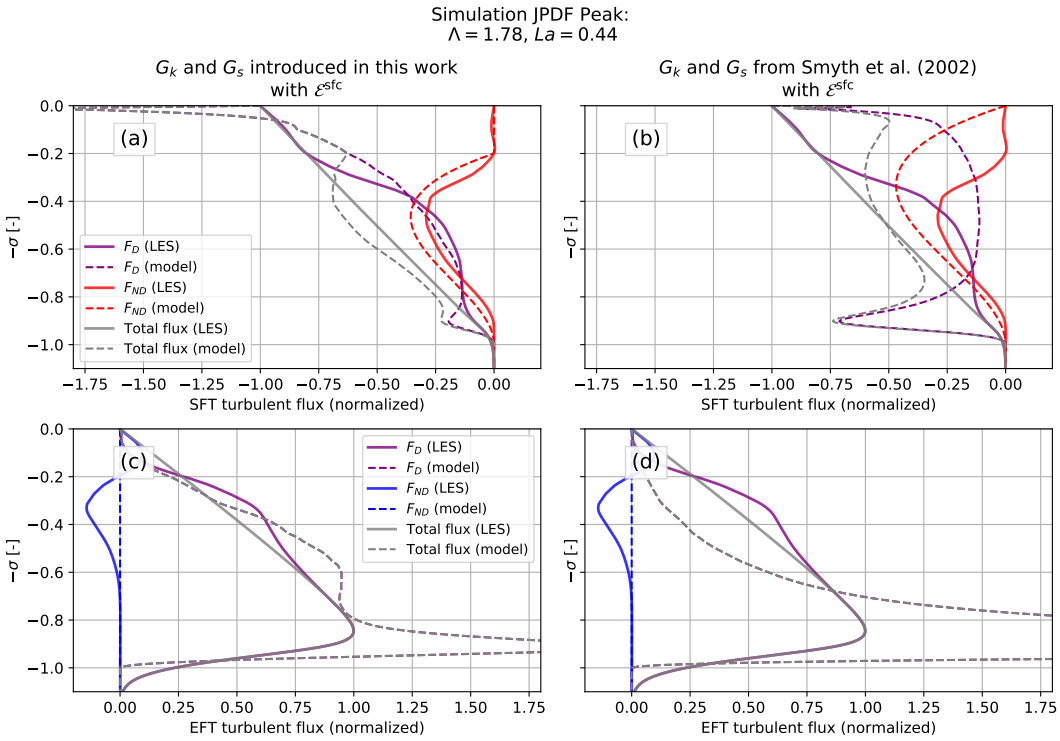

Figure 4.11: Turbulent fluxes for SFTs (top panels) and EFTs (bottom panels) for simulation JPDF Peak. Solid lines are LES results and dashed lines are results from the KPP formulation defined in Section 4.6.3. Model results from left column panels were obtained using the formulation for $G_k(\sigma)$ and $G_s(\sigma)$ proposed here, while right panels use the original KPP formulation for those quantities, as in Smyth et al. (2002). Gray lines are the full turbulent flux, red lines are nondiffusive fluxes due to surface processes and blue lines are nondiffusive fluxes due to entrainment processes.

layer.

The bottom panels of Figure 4.11 show results for the same simulation but for EFTs. Fluxes using our proposed formulation (panel c) are well represented in the middle of the OSBL (even considering the error introduced in neglecting $G_e(\sigma)$; dashed blue line). Model results using the original KPP formulation (panel d) underdiagnose the flux in the same region. The diffusive flux is poorly represented in both cases in the entrainment due again to the very large gradients in this region, however, results are significantly worse using the original KPP formulation (panel d).

Figure 4.11 is predominantly representative of the other simulations studied here: most of the error happens in regions of large gradients (i.e. the surface and entrainment layers) while the middle of the OSBL is better represented. This is true for our KPP formulation using the fitted coefficients $\mathscr{E}$ or Equation (4.17), and for the original KPP formulation using the cubic function for $G_k(\sigma)$.

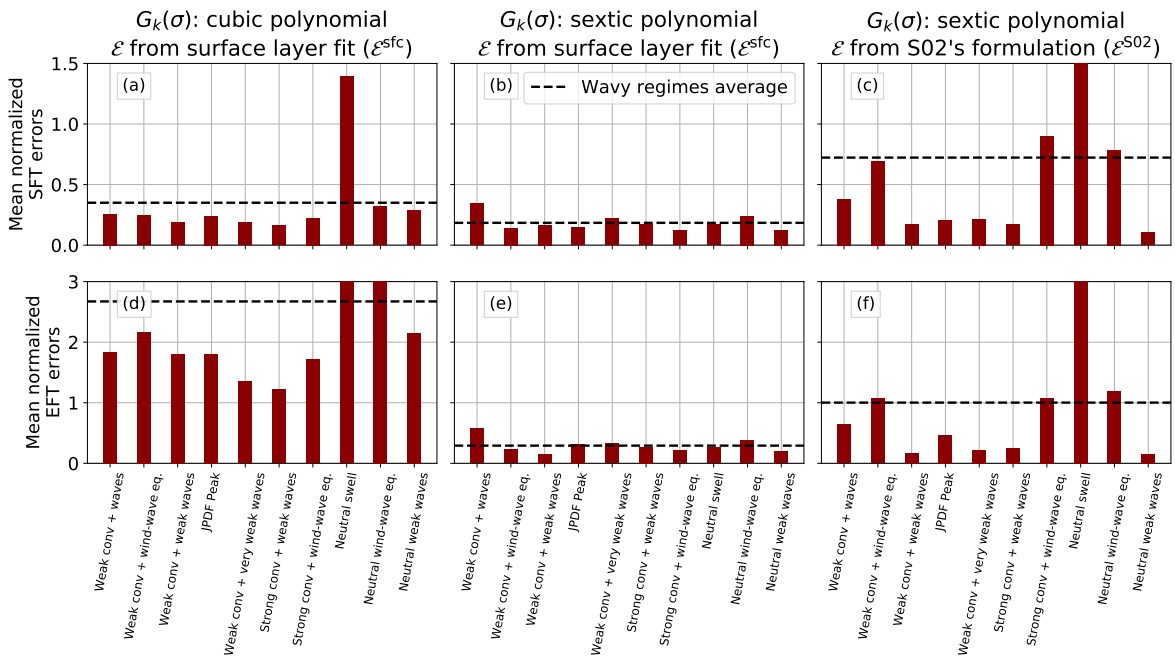

Figure 4.12: Mean normalized error δF for each simulation with waves. Upper panels (a, b, c) show results for SFTs and lower panels (c, e, f) show results for EFTs. Each column shows results for F_{KPP} calculated using a different formulation which change in the shape of $G_k(\sigma)$ and in the magnitude of $\mathscr{E}$, as indicated at the top of each column.

With that in mind we avoid analyzing each simulation in detail by calculating the mean normalized error in the OSBL δF defined as

$$\delta F = \frac{1}{\langle w'c' \rangle_b} \left[\int_0^1 (F_{\mathrm{LES}} - F_{\mathrm{KPP}})^2 \, d\sigma \right]^{1/2}, \tag{4.22}$$

where F is the total flux and $\langle w'c' \rangle_b$ is a normalization factor equal to the total surface flux for SFTs and for the entrainment flux for EFTs.

We apply Equation 4.22 for three KPP formulations. (a) Assuming $G_k(\sigma) = G_n(\sigma) = G_s(\sigma)/C_*$ and using $\mathscr{E}^{\mathrm{sfc}}$, which is similar to previous KPP versions and tests the assumption of a universal shape for K and G_s that is cubic. (b) Using Equations (4.14) and (4.18) with $\mathscr{E}^{\mathrm{sfc}}$. This formulation tests the assumption of a universal shape for wavy regimes that is given by our proposed curves (septic for $K(\sigma)$ and cubic for $G_s(\sigma)$). (c) Using Equations (4.14) and (4.18) with $\mathscr{E}$ from Equation (4.17). This case has an extra assumption compared to formulation b that $\mathscr{E}$ can be given by a simple formula.

Results for δF can be seen in Figure 4.12 for formulations a (left panels), b (middle panels) and c (right panels). Top rows show δF for SFTs and bottom rows show δF for ETFs. Only wavy simulations are shown and the average δF among all simulations is given by a dashed black line. From comparing panels a and b (whose only differences are the eddy diffusive shape and $G_s(\sigma)$) we can see that replacing the commonly used cubic function for the proposed formulations somewhat improves the representation of SFT fluxes, with the main difference happening for the swell regime. However, the improvement for EFT fluxes is much more significant (note the difference in the vertical range between the top and bottom rows). Such a discrepancy in the errors between SFT and EFT fluxes using the cubic function points to an inconsistency between surface and entrainment layer scalings (since $K(\sigma)$ is optimized for the surface layer). Such a large discrepancy does not happen using the shape functions proposed in this manuscript (although there is an increase in δF from around 0.2 for SFTs to 0.3 in EFTs).

Analyzing the transition between the middle panels of Figure 4.12 (formulation b) and the right panels (formulation c) we see that δF more than doubles for both SFTs and EFTs. This indicates that modeling the enhancement factor $\mathscr{E}$ with a simple formulation may be the greatest source of error in wave-aware versions KPP. This fact is not surprising, given the added complexity from Langmuir circulations, and calls for a more data-centric systematic approach to estimate this coefficient in the future.

4.7 Conclusions

In this work we have explored the implementation of Langmuir-motivated modifications to the KPP framework using a recently-introduced optimized approach to estimate KPP components without a priori assumptions (Chor et al., 2020b). In particular, this work investigated the question of how should KPP be modified to account for the effects on Langmuir turbulence. In previous works the only modification considered was an enhancement of the eddy diffusivity (Li et al., 2019), with few authors considering other alternatives (Large et al., 2019). The main conclusion of this work is that two other modifications are likely needed in addition to the eddy-diffusivity enhancement.

First, the formulation of the nondiffusive fluxes F_{ND} should be changed to account for Langmuir

circulations. In previous KPP versions the nondiffusive flux formulation mimics that of the atmosphere and depends solely on the presence of a surface destabilizing buoyancy flux (Large et al., 1994; Sullivan et al., 2010; Smyth et al., 2002). However, by minimizing nondiffusive fluxes for two separate tracers, we showed that the smallest F_{ND} necessary to reproduce observed fluxes using KPP in wavy regimes without buoyancy fluxes is still significant. As an example, in a neutral regime in wind-wave equilibrium ($La = 0.3$) where large flow structures are likely to come from Langmuir circulations, F_{ND} accounts for at least 15% of the total flux and approximately 40% of the flux in the middle of the OSBL (see Figure 4.3). Given that result, we proposed an alternative modulation for $G_s(\sigma)$ (given by Equations (4.18)-(4.20)) in which the effects of Langmuir circulations and convection are additive. A fit of the coefficients to LES data suggest that that waves can account for approximately half the magnitude of nondiffusive fluxes even in the presence of strong convection.

Second, changing the shapes of both the eddy diffusivity and the nondiffusive fluxes is likely to be beneficial. Our results show that the eddy diffusivities assume a shape that appears to be universal as long as waves are present in the flow. This shape is different from the commonly-used cubic polynomial (O'Brien, 1970; Large et al., 1994) and can be represented using a sixth-order function (Equation (4.16)) that is compliant with MOST requirements at the surface. Furthermore, the shape of F_{ND} in our results is also different from currently-used cubic shape, especially at the surface. While previous versions of KPP included a significant amount of nondiffusive flux in the surface layer, our results point to nondiffusive fluxes being negligible in that region, which is more in agreement with MOST. We then propose an alternative shape (given by Equation (4.21)) which successfully captures the shape produced by our results (see Figure 4.6c).

Furthermore, while changes to the eddy diffusivity shape are likely to improve results, it appears that most of the errors in representing turbulent fluxes come from modeling its magnitude in wavy conditions. This magnitude currently depends on MOST scaling and on a multiplicative enhancement factor $\mathscr{E}$. While there is evidence that $\mathscr{E}$ is smaller in convective conditions (see Li et al. (2017) and Figure 4.9), most formulations do not take this effect into account (Takaya et al., 2010; Van Roekel et al., 2012). Given this dependence on the stability Λ, it is possible that nonlinear effects due to the interaction of Langmuir circulations and convective plumes are important in estimating $\mathscr{E}$. This calls for more data-centric systematic studies in order to map out $\mathscr{E}$ for different

regimes in hopes of capturing its behavior with simple analytic formulations.

Moreover, it should be noted that we performed a diagnostic analysis of OSBL turbulent fluxes in which KPP calculations are carried out with averaged profiles from LES, which assesses the accuracy of modeling assumptions rather than model performance. While diagnostic studies are important, our results should also be assessed in the future with prognostic studies (Pope, 2000, Section 13.4.6), in which KPP is tested by using it to advance average profiles in time.

Finally, our simulations are idealized and do not contain several effects that could complicate analyses. These include wind-wave misalignment (Van Roekel et al., 2012) and swell effects on wind-wave equilibrium and broadband wave spectra (McWilliams et al., 2014). Furthermore, we have not considered changes in the Stokes penetration depth in our analysis, which can be taken into account explicitly or implicitly (e.g. by using the surface layer Langmuir number (Harcourt et al., 2008) as opposed to the turbulent Langmuir number). However, these extra complexities were beyond the scope of the present paper and are left for future studies.

CHAPTER 5

Conclusions

5.1 Summary

In this dissertation we have explored the effects of OSBL dynamics on the vertical mixing and transport of passive scalars, along with implications for their horizontal transport. Of the many processes present in the real ocean we focused on the three that seem to be the most relevant for OSBL dynamics: surface wind stress, surface buoyancy fluxes, and nonbreaking waves (Belcher et al., 2012). Contrary to most studies, which tend to focus on a small subset of possible regimes, we have made efforts to explore as much of the parameter space as possible.

In Chapter 2 we focused on buoyant materials and introduced a fully predictive model for horizontal transport of buoyant materials based on a fully diffusive KPP. Results from both LES and the model suggest that even small changes on the buoyancy of materials can lead to large differences in the direction and speed of horizontal transport. This result is aided by field experiment data, which show a small region with large shear near the surface. This chapter effectively accomplishes Objective 3 of this dissertation.

Chapter 3 is an investigation of the atmosphere, but whose conclusions can extend to a waveless ocean (as confirmed by results in Chapter 4). We have analyzed regimes ranging from weakly stable to strongly unstable and showed that the cubic shape that is common in eddy diffusivity models is inappropriate for regimes with some level of convection. Furthermore, we have showed that nondiffusive fluxes are necessary to close the turbulent flux budget even in weakly unstable regimes.

Results of Chapter 3 were only made possible due to a method we developed that allows one to estimate both $K(z)$ and the nondiffusive fluxes using two separate scalars. This novel optimization method makes very few *a priori* assumptions about the flow and works in any ocean regime. Its

main purpose is to inform model development by providing estimates of relevant quantities without scaling and shape biases and by optimizing the estimations for modeling applications. This method effectively accomplishes Objective 2 of the present dissertation.

In Chapter 4 we applied the optimization method introduced in Chapter 3 to OSBLs by carrying out several LES experiments that explore a wide range of forcing combinations and canonical cases. The main conclusion of this research is that Langmuir circulations affect not only the eddy diffusivity, but also the nondiffusive fluxes. Although there have been studies that found evidence of this effect (Chen et al., 2016a), ours may be the first one to provide systematic verification of this fact and to provide a formulation to account for such effects. We showed that our modified formulation for nondiffusive fluxes matches optimized results significantly better than the original formulation which only depends on the presence of destabilizing surface buoyancy fluxes. Our preliminary analyses estimate that nondiffusive fluxes due to Langmuir circulations are comparable in magnitude to nondiffusive fluxes due to convection (e.g. about 40% of nondiffusive fluxes being due to Langmuir circulations for common ocean regimes), underscoring the need for including those effects in future versions of KPP.

Furthermore, a rather surprising result is that the presence of Langmuir cells organizes the flow such that the shapes of both the eddy diffusivity and the nondiffusive fluxes collapse into a function that is different from the commonly used cubic polynomial (but is also independent of other characteristics of the flow). We showed that simply plugging this optimized wave-aware shape function into an already existing wave-aware KPP formulation (Smyth et al., 2002) improved results for passive scalars. This counter-intuitive result suggests that KPP-like models for the OSBL may be more straightforward to formulate than KPP-like models for waveless oceans and ABLs given the ubiquity of waves in the upper ocean (Thorpe, 2004).

Finally, we have used our optimization method to estimate the Langmuir-driven enhancement ($\mathscr{E}$) on the vertical mixing. While many other studies have done so without reaching a consensus, our method is the only one so far that is capable of doing so without imposing shapes to $K(z)$ or F_{ND} and allowing part of that enhancement to act on the nondiffusive fluxes, which gives us hope of producing more accurate estimates. These analyses effectively accomplish Objective 1 of the present dissertation.

5.2 Future work

In Chapter 4 we explored the possibility of beneficial modifications to KPP and results were encouraging enough to motivate the creation of a full KPP-based model for the OSBL, which we see as the main path for future research. This would require formulations for both temperature and momentum, which we have not explored. The case of momentum is particularly complicated since the possibility of the eddy viscosity to be a tensor needs to be taken into account (Wirth, 2010). Thus, the first step moving forward is to investigate how the derived model could be adapted for these two quantities.

Furthermore, we have focused on diagnostic tests in this dissertation — which only apply the model to averaged quantities from LES data. This type of testing is valid in first investigations since it tests the accuracy of a modeling assumption (Pope, 2000, Section 13.4.6), however, in order to gain confidence in a new model, future developments should also be tested prognostically — where average quantities are evolved using the new KPP version that is being tested.

Moreover, despite our efforts to investigate a wide range of ocean regimes in this dissertation, there are still biases that need to be addressed by future studies. The number of regimes explored is still relatively small and no stable oceanic regimes were explored. Our results for the atmosphere (Chapter 3) seem to indicate that stable boundary layers seem to behave similarly to neutral boundary layers but with smaller depth and adjusted according to MOST (and there has been at least one similar report for the ocean (Pearson et al., 2015)). However, since our results show that Langmuir circulations require nondiffusive fluxes to be well represented, it is likely that nondiffusive flux components will play some role in stable regimes as well. This should be investigated since the magnitude of such flux will probably depend on some competition between Langmuir circulations acting to mix the flow and buoyancy fluxes acting against that effect that is yet to be quantified.

Finally, the optimization method we have introduced has proved useful in OSBLs and ABLs that are horizontally periodic and homogeneous. However, the method is general enough that it can also produce results in horizontally heterogeneous conditions; the only change necessary would be in the averaging procedure. This opens up the possibility to investigate the diffusive-nondiffusive flux separation (and eddy diffusivity profiles) in the presence of submesoscale phenomena. It has

been shown that the eddy diffusivity of passive scalars changes across fronts, partly owing to the suppression of Langmuir circulations along the front (Smith et al., 2016; Taylor, 2018). Results also indicate that nondiffusive flux components are necessary in regions with submesoscale activity in order to avoid counter-gradient fluxes (Smith et al., 2016). Thus, there clearly are important dynamics at play due to submesoscales and a more quantitative analysis is desired which can be provided by our optimization method.

APPENDIX A

Preferential concentration of non-inertial buoyant particles in the ocean mixed-layer under free-convection

Authors: Tomas Chor, Di Yang, Charles Meneveau and Marcelo Chamecki.

Abstract:

In this work we investigate buoyant particle dynamics in the Ocean Mixed Layer (OML) under a purely convective regime. We focus on non-inertial, particles that are lighter than the surrounding seawater (thus, buoyant), which is a useful configuration when representing oil, microplastic debris, and other buoyant materials that do not necessarily exhibit strong inertial effects. Our main goal is to understand and describe the physical mechanisms that control the buoyant particles' surface concentration under such conditions, specifically the preferential concentration effects that arise independently of inertia (rather than the well-known centrifuging mechanism for heavy particles). In our investigation we use Large Eddy Simulation to model the particle dispersion in the OML in which the evolution of the particle field is simulated using an Eulerian approach. We find that in addition to the preferential concentration effect that clusters particles into convergence regions on the surface (which is a well-known and straightforward effect on free surfaces), there is a secondary effect for highly buoyant particles that drives them into vorticity-dominated regions. We explain this effect as the advection of buoyant particles by persistent vortices in the flow, which turns out to be the dominating mechanism controlling the surface particle distribution. Highly buoyant particles are trapped in the interior of the vortices (at the surface), which favors clustering in vorticity-dominated regions, while for particles with low buoyancy this effect is negligible.

A.1 Introduction

The near-surface portion of the ocean, namely the ocean mixed layer (OML), is strongly influenced by the dynamic processes induced by the atmospheric forcing and is generally weakly stratified and well-mixed (Pedlosky, 1987). It is also usually the final fate of positively buoyant particles, often with the particles being trapped in it until some other process takes place. This makes the evolution of buoyant particles in the OML an important subject, with various relevant applications such as transport of ocean debris (Kukulka et al., 2015; Brunner et al., 2015; Kukulka et al., 2016), oil spills (Yang et al., 2014; Chen et al., 2016a) and bubble dynamics (Liang et al., 2011). Considering, as an example, the case of oil spills, a thorough understanding of the basic physics and underlying dynamics is vital, since the fate of oil plumes in the ocean surface must be often rapidly predicted using physics-based models. The present work focuses on the dynamics of buoyant particles in the OML under purely convective conditions, and focusing on small-scale three-dimensional turbulence in the absence of mesoscale and sub-mesoscale features. Despite its importance and despite there have being several recent investigations focusing on small scale turbulence effects (Noh et al., 2006; Noh et al., 2010; Yang et al., 2014; Mensa et al., 2015; Yang et al., 2015; Chen et al., 2016a; Kukulka et al., 2016) and sub-mesoscale phenomena (Ozgokmen et al., 2011; Smith et al., 2016), the evolution of buoyant particles in the OML under such conditions has not been addressed in detail up to date.

In order to illustrate the precise scope of this work, consider the approximate particle velocity equation (Ferry et al., 2001; Yang et al., 2016)

$$\boldsymbol{v} = \boldsymbol{u} + w_r \boldsymbol{e}_3 + \frac{w_r}{g}\frac{d\boldsymbol{v}}{dt}, \tag{A.1}$$

where $\boldsymbol{v}$ is the total particle velocity, $\boldsymbol{u}$ is the flow velocity, w_r is the particle terminal rise velocity (we assume $w_r > 0$, i.e., the particles are less dense than the carrier fluid), g is the gravitational acceleration, t is the time and $\boldsymbol{e}_3$ is the unit vector in the vertical upward-pointing direction (more details on the approximations that lead to this simplified equation are discussed in Section A.3). The first two terms on the right-hand side (RHS) are the particle advection by the flow and the terminal rise velocity that comes from the balance between buoyancy and drag forces. The third

term corresponds to inertial effects and can generally be approximated by $w_r g^{-1} D\boldsymbol{u}/Dt$ after an expansion in particle time-scale (Ferry et al., 2001; Yang et al., 2016), where $D(.)/Dt$ is the material derivative. We are interested in flows for which the third term on the RHS of Eq. (A.1) is small compared to w_r, i.e., cases in which the condition $g^{-1} d\boldsymbol{v}/dt \ll 1$ is satisfied. These are particles whose velocity is dominated by flow advection and buoyancy effects, but with comparably weak inertial effects. In the OML this often includes oil droplets, microplastic debris, bubbles, among others.

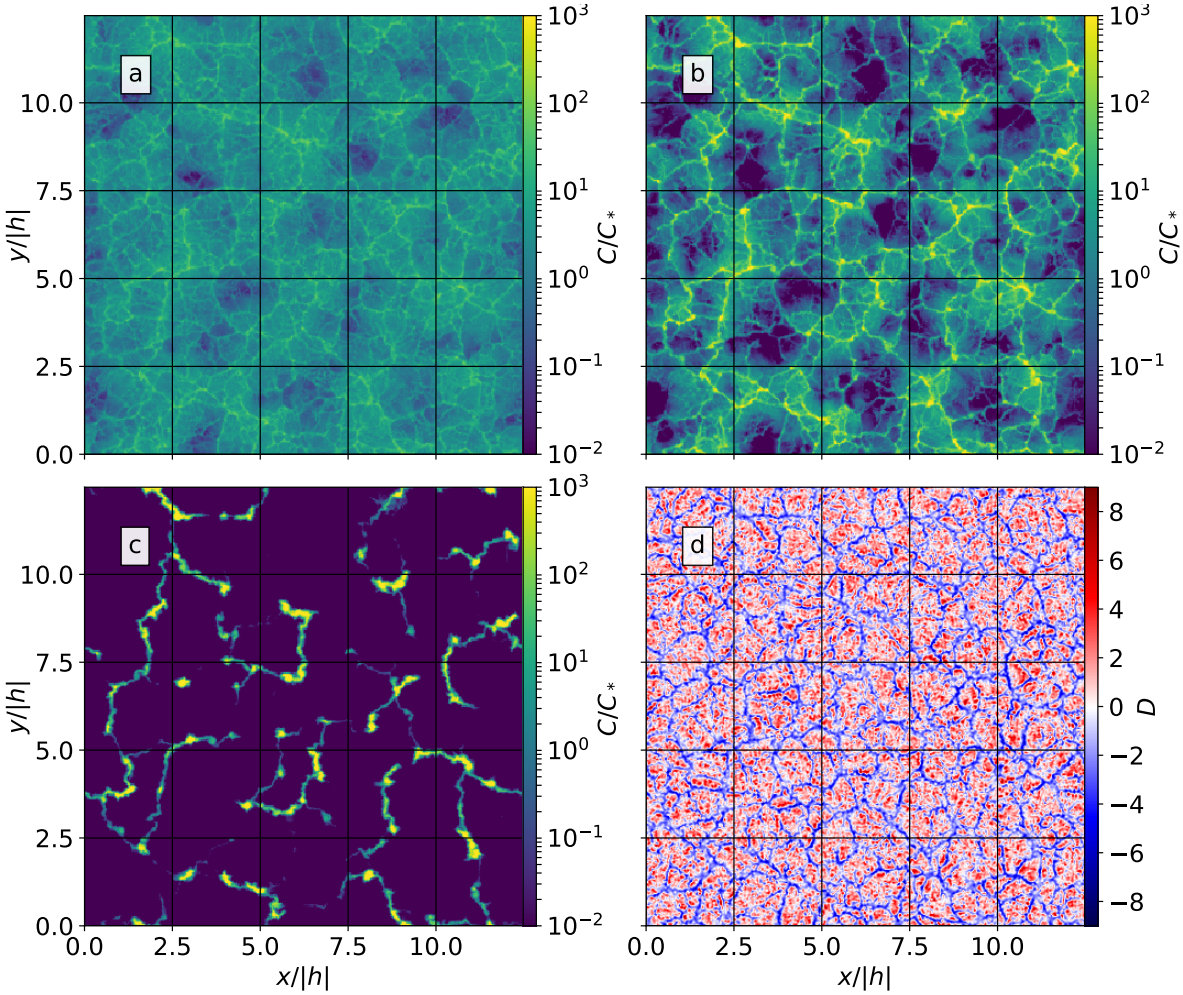

Figure A.1: Normalized surface concentrations for particles C210, C340, C710 (panels a, b and c, in order of increasing buoyancy) and horizontal divergence D at the surface (panel d). h is the OML depth and all panels correspond to the same instant in time. C_* is a concentration scale, whose details will be given in Section A.3.

The omission of the inertial term allows us to focus our attention on a form of preferential

concentration that arises independently of particle inertia. This effect is illustrated in the case of a purely convective flow represented in Fig. A.1(a,b,c), which shows the particle concentration field C obtained via LES using an Eulerian approach (whose details will be given in Section A.3). In all cases displayed we use non-inertial particles with increasing buoyancy from Fig. A.1(a to c). It is clear from the figure that there is preferential concentration of particles in zones of horizontal convergence, seen on Fig. A.1(d) by regions of negative normalized divergence D, defined as

$$D = \frac{1}{\langle |\boldsymbol{S}| \rangle_{\mathrm{vt}}} \left(\frac{\partial u}{\partial x} + \frac{\partial v}{\partial y} \right) \Bigg|_{z=0}, \tag{A.2}$$

while there is significantly low concentration in divergence regions where D is positive. In Eq. A.2, $\boldsymbol{S} = \frac{1}{2}\left[\nabla \boldsymbol{u} + (\nabla \boldsymbol{u})^T\right]$ is the three-dimensional strain rate tensor and $\langle . \rangle_{\mathrm{vt}}$ denotes a Reynolds average which is approximated for practical purposes as a volume and time average. This particular effect (referred to here as the primary preferential concentration effect) is expected and qualitatively simple to understand as the result of downwelling plumes. Particles with very low or no buoyancy get easily submerged in the surface convergence regions due to downwelling and thus can re-surface in the divergent upwelling regions. This tends to homogenize the surface particle distribution since this process effectively provides a communication channel between areas of convergence and divergence at the surface. Particles with higher buoyancy are not as easily submerged and thus do not experience as effectively this communication between downwelling and upwelling zones. Therefore, the main effect of the flow on particles with high buoyancy is to expel them out of the divergence zones and into the convergence zones, where they tend to remain "trapped" for the most part while more particles are collected into the same convergent region.

There is an additional preferential concentration effect (referred to here as secondary) which can be noted by analysing the horizontal scales of the surface particle distributions in Fig. A.1. Notice that, because of the mechanism just described above, particles in Figs. A.1(a,b) are arranged following the convective cells shown in Fig. A.1(d), making the horizontal scales of the distributions seen in Figs. A.1(a,b) and Fig. A.1(d) similar. Conversely, the highly buoyant particles in Fig. A.1(c) are organized in a significantly larger horizontal scale than both the convective cells and the particles with lower buoyancy, being mostly concentrated in much smaller regions. This is exactly the secondary preferential concentration effect, which is not as straightforward to explain as the

primary one, and which becomes evident only for particles with "high buoyancy" and after being advected by the flow after a "certain time" (the precise definition of these terms will become clear in Section A.4.2). We later argue that this is the effect of small-scale vertical vortices, which tend to collect particles in convergent regions of high vorticity. Since inertial effects would introduce a similar preferential concentration behavior (centrifuging (Maxey, 1987)), inertia was disconsidered in order to fully isolate this effect. Note that for both preferential concentration effects, the resulting behavior is for tracer-like particles to be mostly homogenized in the OML while floater-like particles are clustered together in isolated regions on the surface.

To this date, most studies that dealt with particles in the OML considered either neutrally buoyant particles — which we refer to as tracers — or purely 2D surface-moving particles — which we refer to as floaters (e.g., Mensa et al. (2015)). Although many scalars of interest may be approximated by one of those limiting cases, there are many instances for which such an approximation is not possible. In fact, earlier works that explored the range in between tracers and floaters showed that particle distributions in the OML strongly depend on the particle's terminal rise velocity (Yang et al., 2014; Yang et al., 2015; Chen et al., 2016a; Kukulka et al., 2016). The precise dependence, however, appears to have to be investigated in a case-by-case approach for different flow configurations given that the dominating flow structures depend on the forcing mechanisms that drive the flow (e.g., convective plumes produce significantly different patterns from Langmuir cells, which themselves are different from patterns in wind-shear-driven flows). In this work we focus on particle dispersion in a convection-driven OML, which is a regime that has been somewhat unexplored by recent literature (an exception is the work by Mensa et al. (2015)).

We proceed to define the goals of this work. The first one is to quantify both the primary and secondary preferential concentrations under a free-convection regime for particles with different buoyancies. The second objective is to use these quantifications to understand and describe the mechanisms that lead to the secondary preferential concentration of particles (the primary preferential concentration is fairly straightforward to understand so there is no need to focus on it).

The manuscript is organized as follows. In Section A.2 we review the basic physics that govern the dispersion on buoyant particles in the OML. In Section A.3 we describe the numerical model used to obtain our results. In Section A.4 the results are presented and discussed in detail. Flow

characteristics are described in Section A.4.1 and the mechanism responsible for the secondary preferential concentration effect is described in Section A.4.2. We present our concluding remarks in Section A.5.

A.2 Analytic considerations

In this section we briefly review some basic physical properties and analytical results that will aid us in the following sections. Throughout the manuscript we adopt the usual notation that a variable A can be separated into a Reynolds average $\langle A \rangle$ and a turbulent fluctuation A'. For practical purposes $\langle . \rangle$ is calculated as a horizontal and time average unless otherwise noted with a subscript and a comment. As mentioned, we neglect the inertial effects on the particles, which is justified in Section A.3.2. Thus, we can re-write Eq. (A.1) without the inertial term as

$$\boldsymbol{v} = \boldsymbol{u} + w_r \boldsymbol{e}_3. \tag{A.3}$$

Both Eqs. (A.1) and (A.3) are the result of several other assumptions about the nature of the particles' interaction with the flow. First, we assume that the particle volume fraction is always small enough to make particle feedback on the flow negligible, but large enough to make an Eulerian approach valid (Ferry et al., 2001). Furthermore, we consider that the size of the particles is smaller than the Kolmogorov scales of the flow, which allows us to neglect several effects that would be costly to model (Yang et al., 2016). We use x and y for horizontal planes and set $z = 0$ at the ocean surface with z decreasing to negative values below the surface. Given these assumptions, we neglect effects such as Brownian motion, history force, thermophoresis, SGS fluid stress force, Faxen effects, lift force and virtual-mass effects, similar to simplifications made in several other studies (Liang et al., 2011; Yang et al., 2016). Thus, the only effects that we assume to be important and that are included in Eq. (A.3) are gravity, drag and buoyancy, which are accounted for by the parameter w_r.

Now we consider the surface particle concentrations described for Fig. A.1. Since both the primary and secondary preferential concentration effects happen even when the initial condition is a uniform concentration in the OML, we can understand them as the effect of a divergence introduced in the particle velocity field, given that preferential concentration of a scalar that is initially well

mixed only happens when its velocity field is divergent (Mensa et al., 2015). Given that the flow is solenoidal at all points and that the terminal rise velocity is zero at $z = 0$ (which can be taken into account by using the Heaviside step function along with w_r), one can obtain a measure of the divergence of the particle velocity field by applying the divergence operator on Eq. (A.3) as

$$\nabla \cdot \boldsymbol{v} = \nabla \cdot \boldsymbol{u} + w_r \frac{\partial}{\partial z} H(-z) = w_r \, \delta(-z) \tag{A.4}$$

where $H(-z)$ and $\delta(-z)$ are the Heaviside function and the Dirac delta function, respectively (note that $\delta(-z)$ has units of m^{-1} and that we use $-z$ instead of z as the arguments so that the Heaviside function is 1 for negative z). Hence, while passive tracers follow a 3D divergence-free velocity field and floaters follow a 2D divergent velocity field, buoyant particles in general are somewhere in between these two extreme cases. Thus, for the boundary conditions considered here, the particle velocity field has a divergence "source" at the surface which is proportional to w_r, which itself can be regarded as a measure of the continuous space between the purely solenoidal 3D and divergent 2D particle velocity fields.

At this point, it is important to make a clear distinction between the preferential concentration mechanism identified here and the well-known case for inertial particles (Maxey, 1987; Eaton et al., 1994; Noh et al., 2006). In both cases, the preferential concentration arises from a divergence in the particle velocity field. However, while in the case for inertial particles this divergence source arises from an inertial term in $\boldsymbol{v}$, in our case it comes solely from the discontinuity in the terminal rise velocity w_r at the free surface. Thus, the mechanism in our case is not connected to any inertial effects and the only necessary conditions for it to take place are that the particles must have buoyancy, the flow must have a free surface where the particle terminal rise velocity is zero and this surface should have a free-slip condition.

Based on the fact that w_r dictates the divergence of the particle velocity field, we introduce the floatability parameter β, which is an estimate of the physical balance between w_r (a tendency of particles to rise to the surface) and w_* (the eddies' tendency to submerge particles). β is defined as

$$\beta = \frac{w_r}{w_*}, \tag{A.5}$$

where w_* is the Deardorff convective velocity (Kaimal et al., 1976)

$$w_* = \left(g\alpha \left\langle w'\theta' \right\rangle_s |h|\right)^{1/3} = \left(B_0 |h|\right)^{1/3}, \tag{A.6}$$

α is the thermal expansion coefficient, w' is the vertical velocity fluctuation, θ' is the temperature fluctuation, h is the OML depth, B_0 is the outward buoyancy flux at the surface and $\langle . \rangle_s$ denotes a Reynolds average at the surface (approximated for practical purposes as a horizontal and time average). Throughout this work we focus on interpreting the results in terms of β, rather than w_r, in order to render the results more general and scalable amongst different free-convection conditions.

A.3 Simulations

A.3.1 LES description

We use LES to numerically investigate the phenomena introduced in the preceding sections with a code has been applied successfully in other works (Yang et al., 2014; Chen et al., 2016a). The main equations are the filtered three-dimensional incompressible Navier-Stokes equations with the Lilly-Smagorinsky eddy viscosity model for the subgrid-scale (SGS) closure (Smagorinsky, 1963; Lilly, 1967). In our equations Coriolis effects and particle feedbacks on the flow are excluded (see Section A.3.2). The Smagorinsky coefficient is determined dynamically during the simulation using the Lagrangian-averaged scale-dependent dynamic (LASD) SGS model (Bou-Zeid et al., 2005). The seawater density is assumed to have a linear dependence on the temperature θ, and the SGS heat flux closure is achieved by specifying a turbulent SGS Prandtl number (here taken as $Pr_{\text{sgs}} = 0.4$). For more details about the equations and the code used, the reader is directed to Section 2 of Yang et al. (2016), keeping in mind the fact that in this work we ignore the Stokes vortex force, the Coriolis acceleration and particle-induced forces on the flow (i.e., the particle field is transported passively).

The particle mass concentration is described by an Eulerian scalar field whose evolution is governed by (here, a tilde denotes a grid-resolved variable)

$$\frac{\partial \tilde{C}}{\partial t} + \nabla \cdot \left(\tilde{v}\tilde{C}\right) = -\nabla \cdot \boldsymbol{\pi}_C, \tag{A.7}$$

where $\boldsymbol{\pi}_C = \widetilde{\boldsymbol{u}C} - \widetilde{u}\widetilde{C}$ is the SGS flux of particle concentration, molecular diffusion is neglected owing to the dominant effects of turbulence at the scales of the LES, and $\widetilde{v}$ is the resolved velocity of the particle field, given by

$$\widetilde{v} = \widetilde{u} + w_r \boldsymbol{e}_3, \tag{A.8}$$

which is the grid-filtered version of Eq. (A.3).

The flow and temperature fields are solved on a collocated grid in the horizontal direction and a staggered grid in the vertical direction. A pseudo-spectral method is used in the horizontal and a second-order central finite difference method is used for the vertical derivatives. We use a finite-volume method to solve the eulerian particle evolution (Chamecki et al., 2008). The scheme is advanced in time using a second-order Adams-Bashforth scheme along with a projection method (by constructing and solving a pressure Poisson equation) to enforce the no-divergence condition. More details of the basic LES solver can be found in Yang et al. (2014), Yang et al. (2015), and Yang et al. (2016).

A.3.2 Simulation set-up

We focus on a simplified case of an OML flow in a free-convection scenario. Surface wind stress, Coriolis and wave effects are not considered and the only forcing is an upward heat flux (ocean cooling) at the surface. It is worth noting that a test case was run including the Coriolis acceleration which produced virtually no difference in the bulk characteristics of the resulting flow (which we attribute to the fact that there is no mean flow, only fast-changing turbulent flow). Given this test result we proceeded only with the simulation without Coriolis force for simplicity.

Simulations were run on a $320 \times 320 \times 150$ grid spanning $1000\,\mathrm{m} \times 1000\,\mathrm{m} \times 120\,\mathrm{m}$ with a time step of 0.4 seconds. An initial mixed layer depth $h = -80\,\mathrm{m}$ was imposed at the beginning and was enforced by a two-step temperature gradient in the thermocline characterized by $\partial\langle\tilde{\theta}\rangle/\partial z = 0, 0.1$ and $0.02\,\mathrm{K\,m^{-1}}$ in the ranges $z/h < 0.95$, $0.95 \leq z/h \leq 1.05$ and $1.05 < z/h$, respectively. The depth of the thermocline was monitored and verified to not change significantly during the statistical sampling period. In all the statistical steady-state results presented, the calculated OML depth (inferred by the location of the negative peak of $\langle w'\theta'\rangle$) was approximately $h \approx -79\,\mathrm{m}$. Table A.1

Table A.1: Simulation parameters used in this work for the primary simulation. A smaller, secondary simulation was briefly used in Section A.4 that is identical to this one, but with B_0 halved, $L_y = L_x = 400\,\mathrm{m}$ and $h = -50\,\mathrm{m}$. The eddy turnover time is defined as $T_* = |h|/w_*$, where the convective velocity w_* is defined in Eq. (A.6).

Name (notation)	Values
Dimensions ($L_x \times L_y \times L_z$)	$1000\,\mathrm{m} \times 1000\,\mathrm{m} \times 120\,\mathrm{m}$
Grid points ($N_x \times N_y \times N_z$)	$320 \times 320 \times 150$
Spatial resolution ($\Delta_x \times \Delta_y \times \Delta_z$)	$3.125\,\mathrm{m} \times 3.125\,\mathrm{m} \times 0.8\,\mathrm{m}$
Time step (Δ_t)	$0.4\,\mathrm{s}$
Surface heat flux (Q_0)	$150\,\mathrm{W\,m^{-2}}$
Mixed layer depth (h)	$-80\,\mathrm{m}$
Convective velocity (w_*)	$1.778 \times 10^{-2}\,\mathrm{m\,s^{-1}}$
Eddy turnover time (T_*)	$1.25\,\mathrm{h}$

presents a summary of the simulation parameters.

In terms of grid convergence we observe that simulations that use a Lagrangian scale-dependent dynamic model have been shown to converge at coarser resolutions than simulations using a constant-coefficient Smagorinsky model (Sullivan et al., 2011-10; Salesky et al., 2017). In the case of Salesky et al. (2017), who used a modified version of the same code used here, convergence was achieved with $|h|/\Delta_f = 43$ (see the appendix in Salesky et al. (2017)), where $\Delta_f = (\Delta_x \Delta_y \Delta_z)^{1/3}$. In our simulation $|h|/\Delta_f = 40$, which is close enough to the value by Salesky et al. (2017) so that grid convergence can be safely assumed.

We also note that our previous assumption that inertial effects can be neglected is supported by our estimate of the Stokes number $St_\Delta \approx 10^{-4}$, which is based on the smallest resolved eddies of the LES. Here, the Stokes number is defined as the ratio between the characteristic time scale of the particles to the characteristic time scale of the flow. When obtaining these scales, the flow time scale was estimated using the magnitude of the strain-rate tensor (which is similar to the magnitude of the vorticity vector), and the particle time-scale was estimated using Eq. (A5) from Yang et al. (2016).

The simulation was allowed to spin-up for approximately 45 eddy turnover times, after which the flow was verified to be in statistical steady-state before the particle concentration field was initialized. Here, an eddy turnover time is defined as $T_* = |h|/w_*$. Although rigorously there is no steady-state for penetrative convective flows due to the constant entrainment of thermocline water,

Table A.2: Particle terminal rise velocities and their associated droplet sizes considering oil as the particle. The association with diameter is done within 5 microns of accuracy.

	C0	C50	C100	C210	C270	C340	C410	C500	C710	C950	C1000
w_r ($\mathrm{mm\,s^{-1}}$)	0	0.216	0.864	3.45	5.40	7.77	10.58	13.82	21.59	31.09	55.27
β (–)	0	0.0121	0.0486	0.194	0.304	0.437	0.595	0.777	1.21	1.75	3.11
Equivalent oil droplet diameter (μm)	0	50	100	210	270	340	410	500	710	950	1000

we found that for the total simulation time the entrainment rate was small enough that steady-state could be assumed for statistical analysis as long as the averaging period was not much longer than around 4 eddy turnover times.

The particle concentration field was initialized with a uniform unit-valued concentration in the OML. For the sake of readability, we name each particle case by connecting their terminal velocities with those for oil droplets, which we take as having density $\rho_d \approx 859.87\,\mathrm{kg\,m^{-3}}$, (thus, in seawater, a higher value of the rise velocity w_r necessarily implies a larger droplet). This is done using the empirical correlations presented in Zheng et al. (2000) and Clift et al. (2005, p. 113), which take into account the fact that both the Reynolds number and the drag coefficient change as the droplet size changes. We use 11 different droplet sizes which are given in Table A.2 up to 5 μm of accuracy for readability purposes (more accurate droplet sizes can be obtained from the rise velocities also presented in Table A.2). Each simulated case is then denoted by CX, where X is the approximate particle diameter in micrometers (up to 5 μm of accuracy). Using this nomenclature the cases are C0, C50, C100, C210, C270, C340, C410, C500, C710, C950, C1000.

It is worth mentioning that although it is common for oil from spills to have a significant fraction of its mass in droplets with diameter d larger than 1 mm (Lehr et al., 2010; Adams et al., 2013), droplet C1000 is already well into a floater regime for our flow configurations, so having extra droplets with higher rise velocity would not impact the results presented here. Thus, the range of our rise velocities does not limit the application of our results for the case of oil spills, making it possible for some of the results presented to be extended to such cases.

After the particle concentration initialization the simulation with the particle concentration field was run for approximately 26 eddy turnover times. We considered the particle distribution to

be in statistical steady-state after about 20 eddy turnover times (approximately one day), and all steady-state particle-related statistics were computed for the period consisting of approximately the last 4.5 eddy turnover times. It is important to note that the duration of our simulation is within reasonably expected ocean time scales. Since long periods dominated by convection are not uncommon in the ocean (Brainerd et al., 1993; Large et al., 1994), we believe that our simulation of the flow can be representative of real oceanic conditions.

A.4 Results and discussion

For the sake of readability we omit the tilde to indicate grid-resolved variables from now on and define the normalized time as $t_* = t/T_*$ with $t_* = 0$ at the moment of particle concentration initialization. We start by first characterizing relevant flow characteristics and then proceed to particle-specific results.

A.4.1 Characterization of the flow

In this section we characterize the topology of the surface flow, which will be important when analyzing the horizontal buoyant particles' distribution in steady-state. We leave the characterization of statistical variables in Appendix B. In Fig. A.2 we show the joint probability density function of the normalized horizontal velocity divergence D and the normalized Okubo parameter Q, defined as (Okubo, 1970)

$$Q = \frac{1}{\langle |\boldsymbol{S}|^2 \rangle} \left[\underbrace{\left(\frac{\partial u}{\partial x} - \frac{\partial v}{\partial y} \right)^2}_{\text{Stretching}} + \underbrace{\left(\frac{\partial u}{\partial y} + \frac{\partial v}{\partial x} \right)^2}_{\text{Shearing}} - \underbrace{\left(\frac{\partial v}{\partial x} - \frac{\partial u}{\partial y} \right)^2}_{\text{Vorticity}} \right]_{z=0} \tag{A.9}$$

for the surface flow in steady-state, where only the horizontal components are taken into account. We refer to Q as the Okubo parameter to make the explicit distinction from the Okubo-Weiss parameter, which is obtained through the same reasoning (and has a similar physical meaning and formulation) but is generally used in incompressible flows (Weiss, 1991). Since the surface horizontal divergence D is an important parameter for our analysis, it is not feasible to use the

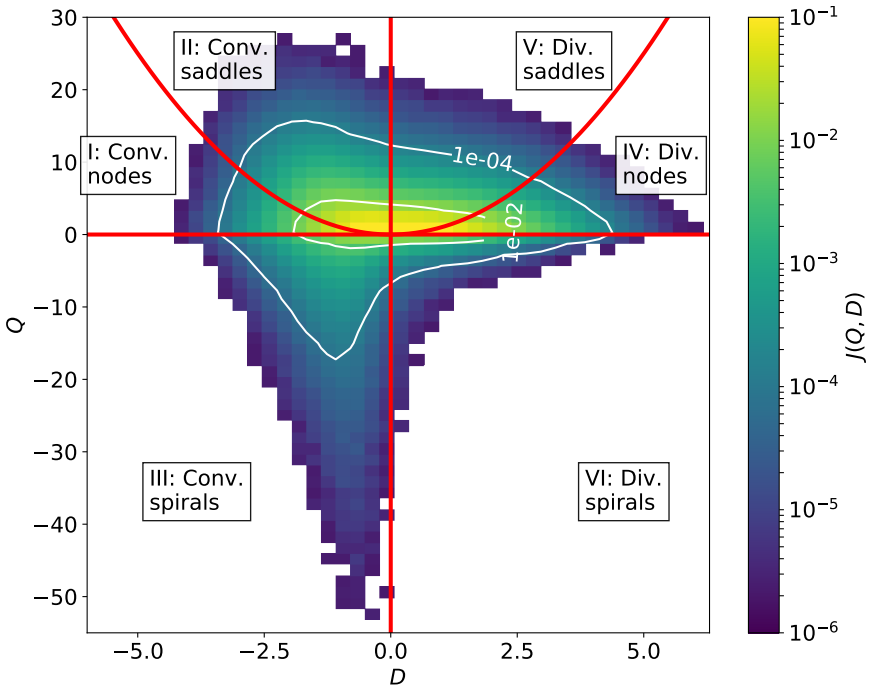

Figure A.2: Joint probability density function of the horizontal divergence D (see Eq. (A.2)) and the Okubo parameter Q (see Eq. (A.9)) for the flow field at the surface. The labels in each of the quadrants defined by the red lines are the flow classifications according to Okubo (1970).

incompressible 2D Okubo-Weiss parameter. We limit ourselves at this point to noting that regions of $Q > 0$ can be understood as being strain-dominated, while regions of $Q < 0$ are equivalent to vorticity-dominated areas, which we call "spirals" following the nomenclature of Okubo (1970).

The red lines in Fig. A.2 are the curves $Q = 0$, $D = 0$ and $Q = D^2$, which define the major flow types according to Okubo (1970): convergent nodes, saddles and spirals, and divergent nodes, saddles and spirals as indicated in their respective regions in Fig. A.2. We formalize this classification by denoting different regions by a set of symbols collectively denoted as P, where P can assume values $P = \text{I, II, } \ldots \text{ VI}$, respectively, depending on the values of D and Q at any given point $\boldsymbol{x}$ and time t. The meaning of I, II, ... VI is listed in Fig. A.2. In his original paper, Okubo (1970) presented other classifications that happen when the (Q, D) pair falls exactly on the red lines in Fig. A.2. Since this virtually never happens numerically, we omit those from our analysis. More details regarding this classification of points can be obtained in Okubo (1970).

When analyzing Fig. A.2, it is clear that points that have small values of both Q and D are significantly more common than points in the extreme (note that the color bar is in a log-scale).

Furthermore, we see that points that are strain-dominated ($Q > 0$) have higher probability density than their vorticity-dominated counterparts. Finally, while there are some cases of convergent vorticity-dominated areas (III; convergent spirals), there are significantly less cases of divergent vortical regions (VI). This is due to vortex-stretching, which amplifies vorticity in the downwelling (convergent) regions and has an opposite effect for upwelling. It is worth noting that convergent regions are colder with respect to their vicinity, which corresponds to a negative buoyancy anomaly, thus producing the downwelling.

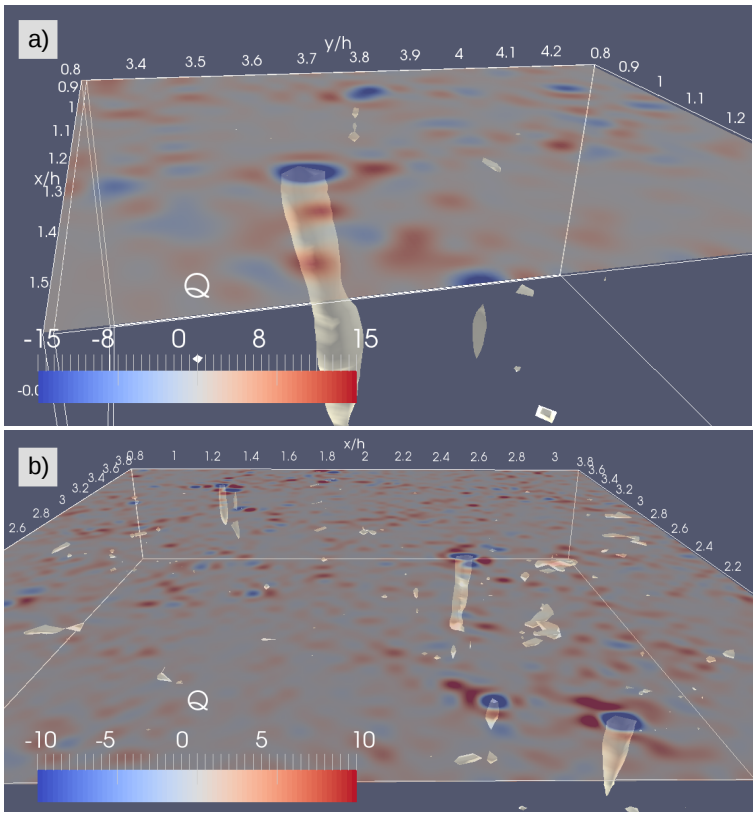

Figure A.3: Detail of a strong vertical vortex (a) and several vertical vortices in a small region of the simulation domain (b). The color contours shown at the top surface are the 2D Okubo parameter Q and the isosurface is a surface of constant 3D Okubo-Weiss parameter Q_{3D}.

Furthermore, although convergent spirals are significantly less common than strain-dominated zones, their persistence time is much longer than types of surface flow structures, which was verified to be true for our case by visual inspection (but is a well-known behavior in 2D turbulence (Perlekar et al., 2011; Kadoch et al., 2011)). This can be understood by noting that the great majority of convergent spirals at the surface (negative peaks in Q) are actually one end of a 3D vortex tube that

extends downwards from the surface. One example can be seen in Fig. A.3(a), in which the surface colormap is the Okubo parameter Q (Eq. (A.9)) and the isosurfaces shown are surfaces of constant Q_{3D}. Here, Q_{3D} is one of the three-dimensional tensor invariants of the flow (Martín et al., 1998) normalized by the strain rate:

$$Q_{3D} = \frac{1}{\langle |\boldsymbol{S}|^2 \rangle} \left(|\boldsymbol{S}|^2 - |\boldsymbol{\Omega}|^2 \right), \tag{A.10}$$

where $\boldsymbol{\Omega} = \frac{1}{2}\left[\nabla \boldsymbol{u} - (\nabla \boldsymbol{u})^T\right]$ is the rotation tensor. Note that Q_{3D} is the three-dimensional analogue of the Okubo (1970) parameter Q, and it is defined here with the opposite sign as it is generally used in the 3D turbulence literature (Martín et al., 1998; Meneveau, 2011) in order to agree with Eq. (A.9) in a 2D special case. Vortices such as the one in Fig. A.3(a) are known to be resilient features in the flow (Batchelor, 1973, Sec. 5.3) (Davidson, 2004, Sec. 2.3.3), in our case often persisting over one eddy turnover time ($T_* = |h|/w_*$), even though their scale is considerably smaller than the mixed layer depth. They are also a common feature at any given time, as can be seen in Fig. A.3(b), which shows a small part of the domain with several such examples. Their persistence and frequency of occurrence allows for many vortex merging events, both destructive (when the vortices have opposite-sign circulations) and constructive (when vortices have same-sign circulations). Since negative peaks in Q at the surface are one end of these vortices, they are also persistent, have frequent merging events and, as a consequence, will turn out to have a key effect on surface particle distribution, as will be shown in Sec. A.4.2.

A.4.2 Surface particle distribution

In this section we focus on the horizontal distribution of the particles on the surface, with the goal of understanding the mechanisms that act to produce the structures like the one depicted in Fig. A.1, specifically the preferential concentration effects already introduced. The particle initial condition is $C(\boldsymbol{x},t)/C_* = 1$ in every point in the domain that has near-zero temperature gradient, where C_* is a particle concentration scale. In this simulation this corresponded to having roughly the first 70 m of the OML start with unit normalized concentration. This specific initial condition ensures that particles will be easily mixed in OML and that the particle distribution will reach statistical

steady-state within a short period of time.

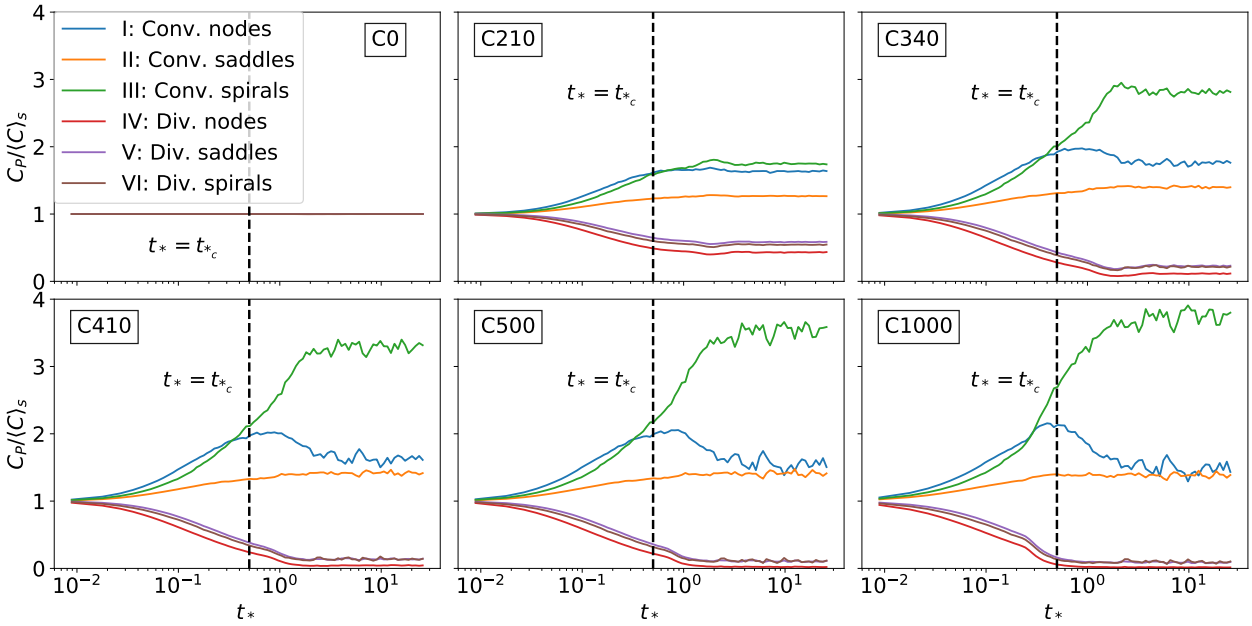

Figure A.4: Time evolution of normalized P-conditioned average particle concentration $C_P(P,t_*)$ for C0, C210, C340, C410, C500 and C1000. $\langle C\rangle_s$ is the average of particle concentration at the surface. Data is smoothed by averaging over log-spaced bins.

As previously discussed, Fig. A.1 shows the surface concentrations for cases C210, C340 and C710 (panels a, b and c, with floatabilities $\beta = 0.194$, 0.473 and 1.21, respectively), with the divergence D in Fig. A.1(d). A closer look at the figure reveals that, while the largest values of the particle concentration field (in all three cases) are concentrated in convergence zones (due to the primary preferential concentration effect), particles with higher buoyancy have a preference for certain parts of the convergent regions as opposed to others (due to the secondary preferential concentration effect). We quantify and explain this by performing a flow topology analysis based on Okubo (1970) following the previously mentioned classification of points in types P (see Fig. A.2). We first introduce the P-conditioned average particle concentration at the surface, $C_P(P,t_*)$, defined as

$$C_P(P,t_*) = \langle C(\boldsymbol{x},t_*)\,|\,P\rangle\,\Big|_{z=0}, \tag{A.11}$$

where $P = \text{I, II, } \ldots \text{ VI}$ is the flow classification based on (Okubo, 1970). We plot the evolution of C_P (normalized by the average particle concentration at the surface $\langle C\rangle_s$) in Fig. A.4 for six different

cases (C0, C210, C340, C410, C500 and C1000). It is clear that for early times ($t_* \lesssim 0.5$) the immediate general behavior for buoyant particles is for concentrations to rise in convergent regions (I, II, III), and to decrease in divergent regions (IV, V, VI). This primary preferential concentration effect was explained in Section A.1 as a straightforward consequence of downwelling plumes and that is now being quantified. After this initial behavior, we can see in cases C340 to C1000 that the particle concentration in convergent nodes (I) begins to decrease, while the concentration in convergent spirals (III) continues to increase, until they reach equilibrium roughly after $t_* \approx 5$. The decrease in concentrations in convergent nodes and increase in convergent spirals (which is more accentuated the larger the floatability β) is caused by the secondary preferential concentration effect. Thus, while the primary preferential concentration effect appears immediately after the initial particle release, the secondary effect only becomes evident after a certain time. We then infer the existence of a critical time scale $t_{*_c} = t_c/T_*$ after which the secondary preferential concentration mechanism becomes important, and visually estimate it using the curve for the concentration in convergent nodes (I), which shows a very clear inflexion point. In our case we estimate it as roughly $t_{*_c} \approx 0.5$, and mark it in Fig. A.4 with vertical dashed lines. t_{*_c} is later shown to be a consequence of the vortices collecting particles at the surface.

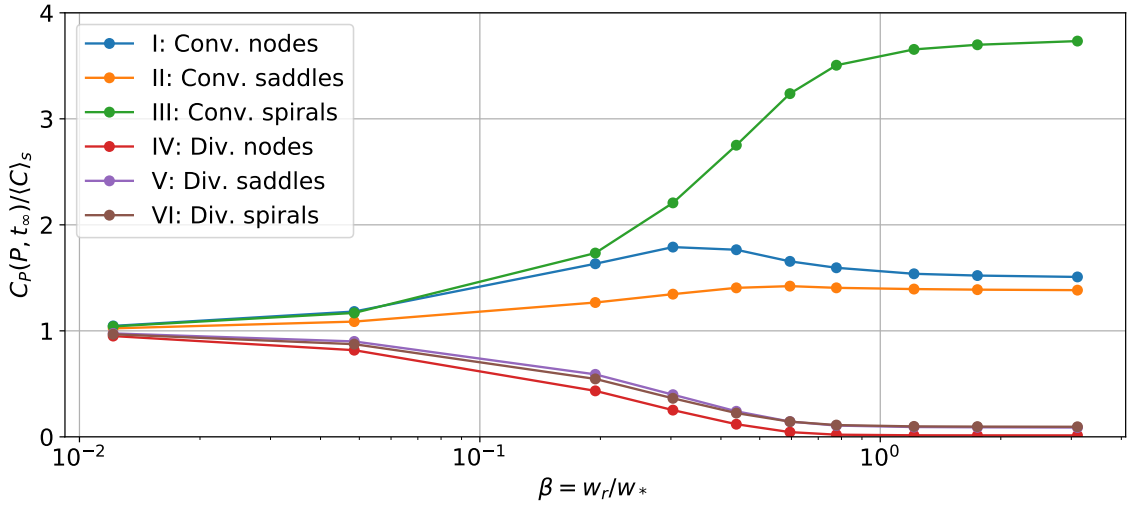

Figure A.5: Steady-state for P-conditioned surface concentrations (normalized by average surface concentration) for different types of surface flow structures and different particle cases (plotted as β),

We now plot the equilibrium (steady-state) values as shown in Fig. A.4 (which we take as

estimates of $C_P(P,t_\infty)$, with t_∞ being an estimate for $t_* \to \infty$) in Fig. A.5 as a function of the floatability β. Note that most curves appear to be monotonic with respect to β, with the exception of convergent nodes (I). Despite this exception, the general behavior is clear: the larger the floatability β for a particle, the higher the concentration in convergent spirals (III) in comparison with convergent nodes (I). Furthermore, as β increases, divergent regions become less and less populated, while the only regions that do not have a significant evolution with β are convergent saddles. Moreover, from Fig. A.5 we see that when $0.1 < \beta < 1$ there is a transition behavior from a tracer regime to a floater regime. This is strong indication that the particles in cases C710, C950 and C1000 ($\beta \gtrsim 1$) are already in a buoyancy-dominated regime (floater-like behavior). It is worth noting that, since there are significantly more convergent saddles than convergent spirals in the current convection-driven flow (see Fig. A.2), the total mass of particles in regions II and III are very close (not shown), even though region III dominated the magnitude of particle concentration.

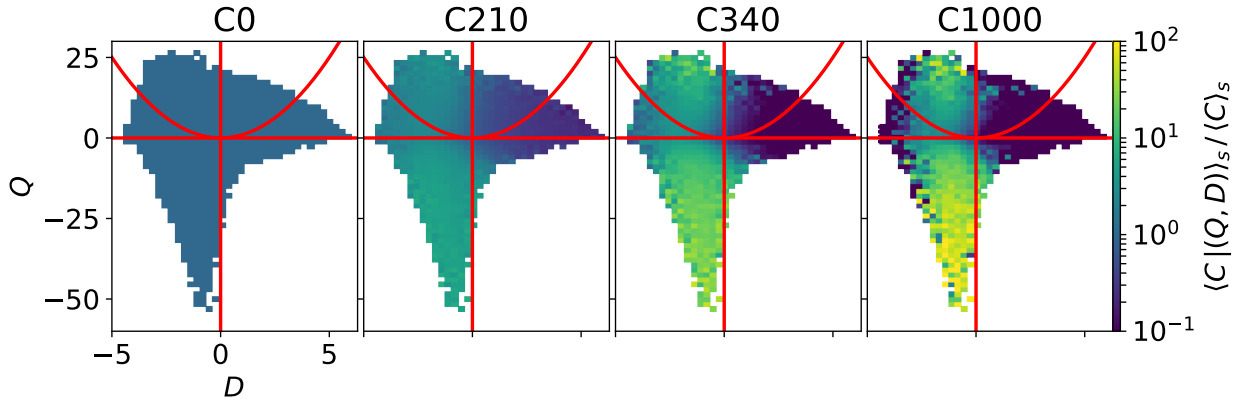

Figure A.6: Concentration map of the conditioned average surface concentration $\langle C\,|(Q,D)\rangle_s$ normalized by surface concentration for particles C0, C210, C340 and C100 in steady-state.

A more detailed view of the steady-state regime can be obtained when analyzing the average particle concentration conditioned to (Q,D) pairs, which we denote as $\langle C\,|(Q,D)\rangle_s$, as shown in Fig. A.6 for cases C0, C210, C340 and C1000. The preference for particles to be concentrated in convergent regions (and "diluted" in divergent regions) is evident for all cases except the non-buoyant case C0, as was expected because of the primary preferential concentration effect. Furthermore, we see that cases with large β, e.g. C1000, particles tend to concentrate in the extreme values of $|Q|$. The high concentrations in negative Q peaks can be easily understood, since preference for particles

to cluster in convergent spiral regions increases as Q becomes more negative (i.e. the local flow is more dominated by vorticity). Thus, these high concentrations at the bottom of Fig. A.6 are another indication of the secondary preferential concentration effect.

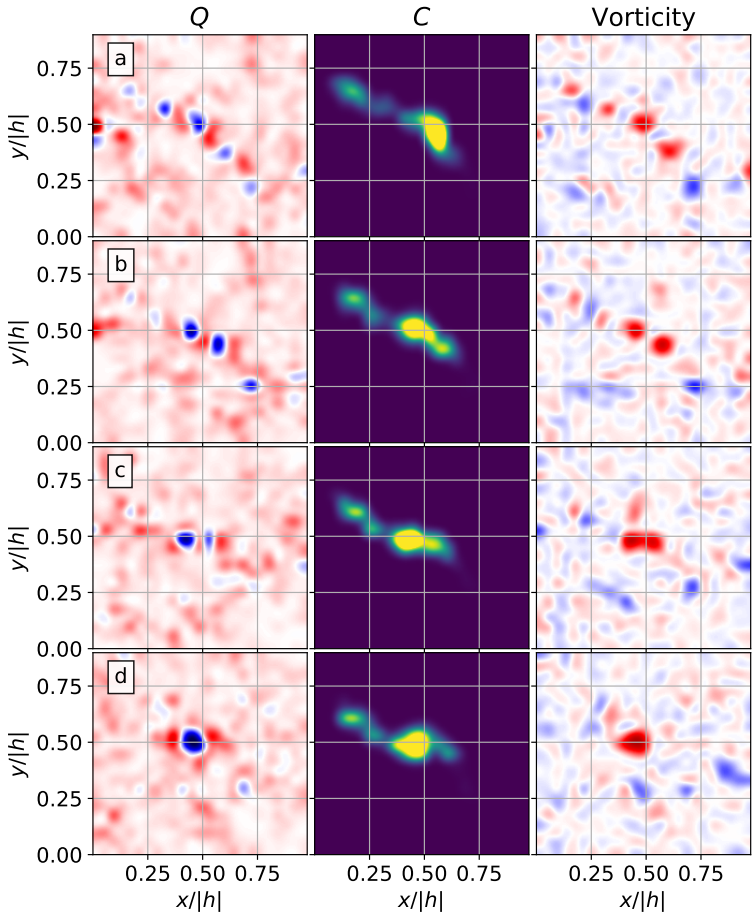

Figure A.7: Sequence of snapshots at increasing time (from top to bottom) of the Okubo parameter Q, particle mass concentration C and vorticity on the surface. The sequence shows a constructive interaction and the colormaps are the same as Fig. A.1.

The high particle concentrations in regions with positive peaks in Q can be explained only after the mechanism driving the secondary preferential concentration effect is explained. We do that by first noting that strongly vortical convergent regions not only tend to attract particles, but they also have large persistence times (compared to other features of the flow), as was already discussed in the end of Section A.4.1 (recall that surface regions with strong negative Q are one end of a vertical vortex). Their effect on tracer-like particles is small, since soon after the particles are attracted to these vortices they are submerged and resurface in divergent regions, which is the reason

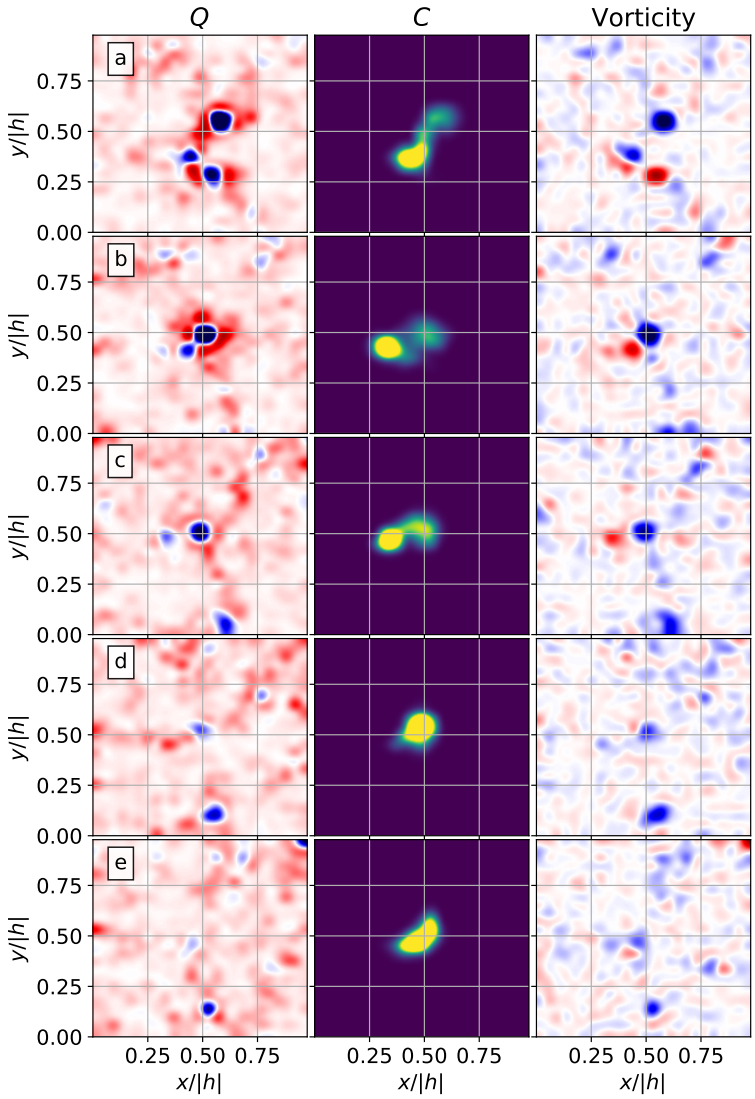

Figure A.8: Sequence of snapshots at increasing time (from top to bottom) of the Okubo parameter Q, particle mass concentration C and vorticity on the surface. The sequence illustrates a destructive vortex interaction and the colormaps are the same as Fig. A.1.

the secondary preferential concentration effect is not evident for particles in cases C0 and C210 ($\beta < 0.2$) in Fig. A.6. However, particles with large floatability remain on the surface after being attracted to these highly vortical regions, where they get horizontally advected with the vortices themselves (since there is little exchange of particle mass between the vortex and the outside flow) as the vortices collect more particles, thus creating small regions with high concentrations. Hence, vortical regions act as particle collectors and carriers.

This behavior is illustrated in Figs. A.7 and A.8, which show sequences of snapshots depicting

the Okubo parameter Q, particle mass concentration C, and vorticity. The snapshots in both figures advance in time from top to bottom, with an interval between panels of approximately $0.15T_*$ and $0.22T_*$ for Figs. A.7 and A.8, respectively. In Fig. A.7 we see a constructive vortex interaction in which the evolution of the concentration seen in the middle-column panels is dominated by two vortices of positive circulation that interact and merge into a stronger vortex. This type of interaction contributes to produce the peaks in concentration for the strongly negative values of Q seen in Fig. A.6. In Fig. A.8 we see a destructive vortex interaction in which vortices with opposite-sign circulations weaken each other until finally there is no vortex (Fig. A.8(e)). It is also clear in this case that the vortex dynamics completely dominate the high particle concentration region seen in the middle-column panels. Furthermore, this interaction illustrates that destructive mergers leave behind a cluster of "orphan" particles: i.e., particles that were previously inside vortices that got broken apart by the flow.

The vortex interactions just described can also explain the high concentration peaks for large positive values of Q seen in Fig. A.6. Notice that positive peaks in Q (which are saddle points and appear as dark red shades in Figs. A.7 and A.8) are more common at the borders of the vortices that are interacting than anywhere else in the flow. Consider, for example, Fig. A.8(a,b), which shows high values of Q (dark red) around the three interacting vortices (dark blue). We see in those panels that while some particles move in-between different vortices (which is a process virtually exclusive to interacting vortices), they transition through high Q regions, which are saddle points with strong straining motion. This suggests that the high particle concentrations in regions with large values of Q seen in Fig. A.6 are a consequence of the movement of particles that are caught up in vortex interactions.

These types of vortex interactions (as particle advection mechanisms) are very common and are seen throughout the simulation, thus it is not surprising that they play an important role affecting in the surface particle distribution in steady-state. As a final remark, we note that they also explain why the secondary preferential concentration effect becomes evident only after some time t_c. Since the concentration is homogenized in the beginning of the simulation, it takes the flow approximately $0.5T_*$ after the initial condition for a significant amount of particles to be collected by the vortices. Before this time, both nodes and spirals (both of which have strong downwelling motion) attract

particles somewhat equally. After approximately half of an eddy turnover time (or $t_{*_c} \approx 0.5$) nodes start to break (by straining action of the flow) while spirals persist and continue collecting particles. Thus, the time t_{*_c} is when the persistence of spirals starts to become important as to make a significant change in the evolution of surface particle concentrations.

A.5 Conclusion

In this work we have studied the mechanisms controlling surface particle distribution in the ocean mixed layer (OML) in a free convection regime. A large eddy simulation was used to simulate the evolution of the particle concentration for 11 different cases with different levels of buoyancy, which translate into 11 different values for the terminal rise velocity, that were assumed to have no inertia.

A primary and a secondary preferential concentration effects were identified and quantified by analysing the concentration in different surface regions according to a flow topology analysis based on Okubo (1970). We found that the primary preferential concentration effect, in which particles are "expelled" from horizontally divergent regions on the flow's surface, happens immediately after initialization, as already expected (Mensa et al., 2015). We also found that the secondary preferential concentration effect, in which particles are attracted to highly vortical convergent regions of the flow, only becomes evident after about 0.5 eddy turnover times and for highly buoyant particles ($\beta \gtrsim 0.5$). This secondary effect was explained as the consequence of resilient surface vortices acting as particles collectors that "trap" highly buoyant particles in vortical regions. While the particles are trapped, the vortices continue being advected by the flow and collecting more particles until eventually they get weaker and are broken up by the flow. Once again we note that, although the final result is qualitatively similar to preferential concentration of inertial particles (where light particles also concentrate in vortical regions (Eaton et al., 1994)), the mechanism that drives this behavior does not rely on any inertial effects.

Finally, the significant effect of floatability on particle preferential concentration may have important implications for parameterization of subgrid scale transport in regional and global models. The preferential concentration effects described here (especially the secondary effect) can be

understood as anti-diffusion, which is a process by which initially separated particles cluster into small regions, instead of spreading out, as time progresses. Anti-diffusive behavior of floaters has been observed in larger scales in the ocean, often in connection to spiraling flows (Munk et al., 2000; D'Asaro et al., 2018). Currently, subgrid scale transport of scalars in regional and global circulation models is parameterized as a diffusive process without any dependence on the buoyancy of the scalar. Although it is hard to assess the impacts that the preferential concentration effects described here may have on larger scale transport of buoyant particles, it is possible that they are significant enough to make it necessary to include some anti-diffusive component linked to a measure of the floatability in the parameterization schemes.

APPENDIX B

Characterization of flow statistics

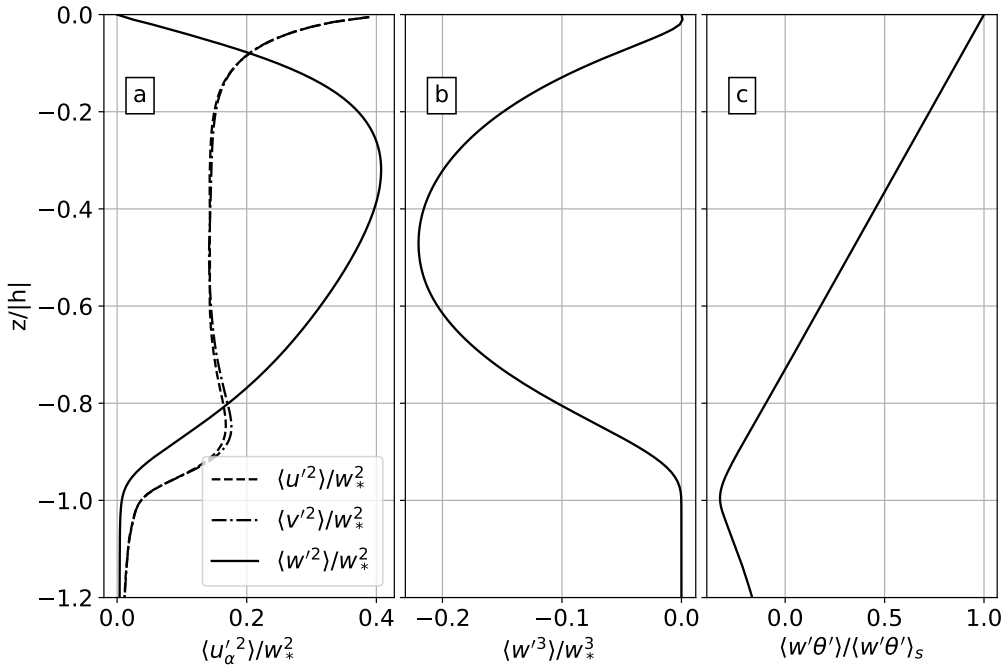

Figure B.1: Profiles of u_α (u, v and w) variances (a), vertical velocity skewness (b) and heat flux (c) for steady-state.

Here we briefly describe the statistical profiles of our simulation, mainly for the sake of completeness. Fig. B.1 shows some mean flow profiles in steady-state. The variance profiles for the horizontal velocities (Fig. B.1(a)) have a shape typically expected for free convection, with a maximum at the surface and a smaller peak in the entrainment zone, which is consistent with previous results (Denbo et al., 1996; Wang, 2006). The variance of the vertical velocity w (Fig. B.1(a)) peaks at $z/|h| \approx -0.3$, as is expected (Denbo et al., 1996; Wang, 2006), while its skewness (Fig. B.1(b)) peaks at approximately the middle-depth of the OML, also in agreement with previous results (Wang, 2006). The negative values of the skewness, which is an important parameter in boundary-layer dynamics (Sullivan et al., 2011-10), indicate strong downwelling

plumes counterbalanced by weak upwelling regions, which we anticipate to have strong influence on the distribution of the particles in the OML. The heat flux profile (seen in Fig. B.1(d)) indicates an upwards heat flux that decreases linearly from the surface and has a second (negative) peak in the entrainment layer, consistent with previous results (Wang, 2006).

APPENDIX C

Alternative closures to Equations (3.13)-(3.15)

In this appendix we show why both currently-used flux decompositions fail one of more of the plausibility criteria introduced in Section 3.2, motivating the need for the broader decomposition given by Equation (3.12).

The fully-diffusive separation (and therefore WB84's model) violates criterion 1 since $K(z)$ is different for SFTs and EFTs in convective ABLs (see Fig. 3.8) and can violate criterion 2 depending on the ratio $\langle w'c' \rangle_e / \langle w'c' \rangle_s$ (Holtslag et al., 1991). Two-term separations can be arrived at by adding an extra equation to Equations (3.13)–(3.14). The most logical option is to assume $G_e = 0$, which makes physical sense and is in line with D66's model but violates criterion 3. Due to this violation, the G_s profile produced by this option exhibits a region close to the surface where $G_s < 0$ (as shown in Fig. C.1) where we would expect $G_s \approx 0$ according to MO similarity theory. These negative values of G_s are large enough that they are understood as a qualitative deficiency of this approach.

Two other obvious alternatives exist, but are not appealing from a physical perspective and have no analogous in the literature. Assuming $G_s = 0$ produces a situation where the only the nondiffusive fluxes are entrainment-driven and, while this does not violate any of our criteria, it is an undesirable characteristic for a decomposition. Finally, one can set $G_s = G_e$, which produces determined linear system of equation, but the results violate Criterion 2 (not shown).

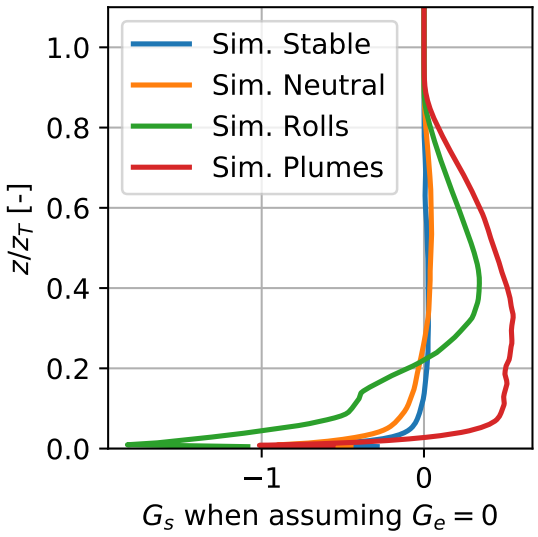

Figure C.1: Profiles for G_s when performing a two-term decomposition by assuming $G_e = 0$.

APPENDIX D

Detailed turbulent fluxes decompositions

In this section we show turbulent flux decomposition results using the optimized method for all 13 simulations used. Decompositions for SFTs are shown in Figure D.1, while EFTs results are shown in Figure D.2. Each panel shows a different simulation. It is worth noting that simulation Pure Wind stress (panel e in both figures) exhibits a fully diffusive turbulent flux according to our method. This is the expected physical behavior and it builds confidence in the approach. Furthermore, the shapes of the flux components are very similar, albeit with different magnitudes for different regimes.

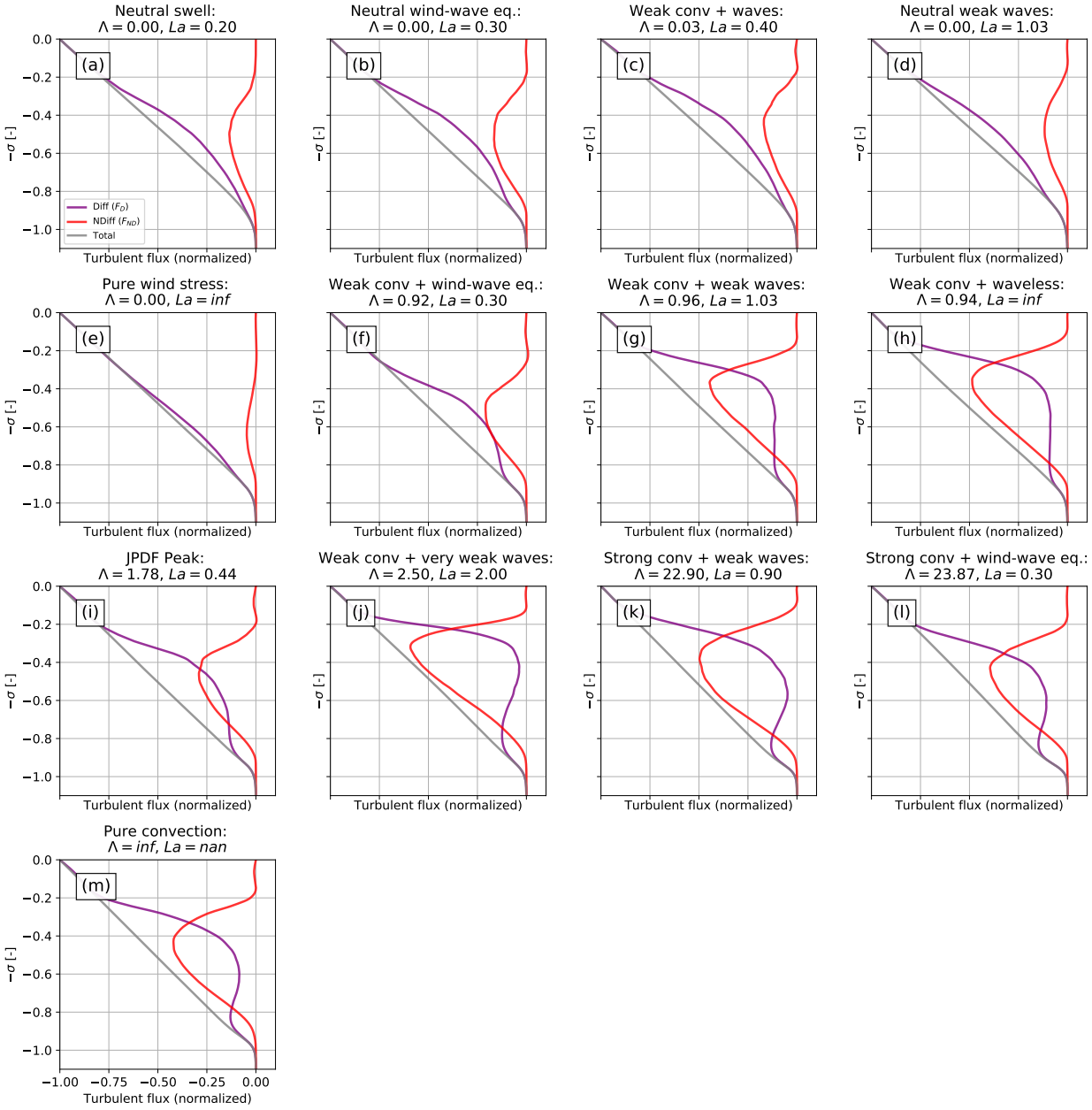

Figure D.1: SFT flux decompositions using the optimization method for all 13 simulations. Diffusive fluxes are shown in purple, nondiffusive fluxes are shown in red and total fluxes are shown in gray.

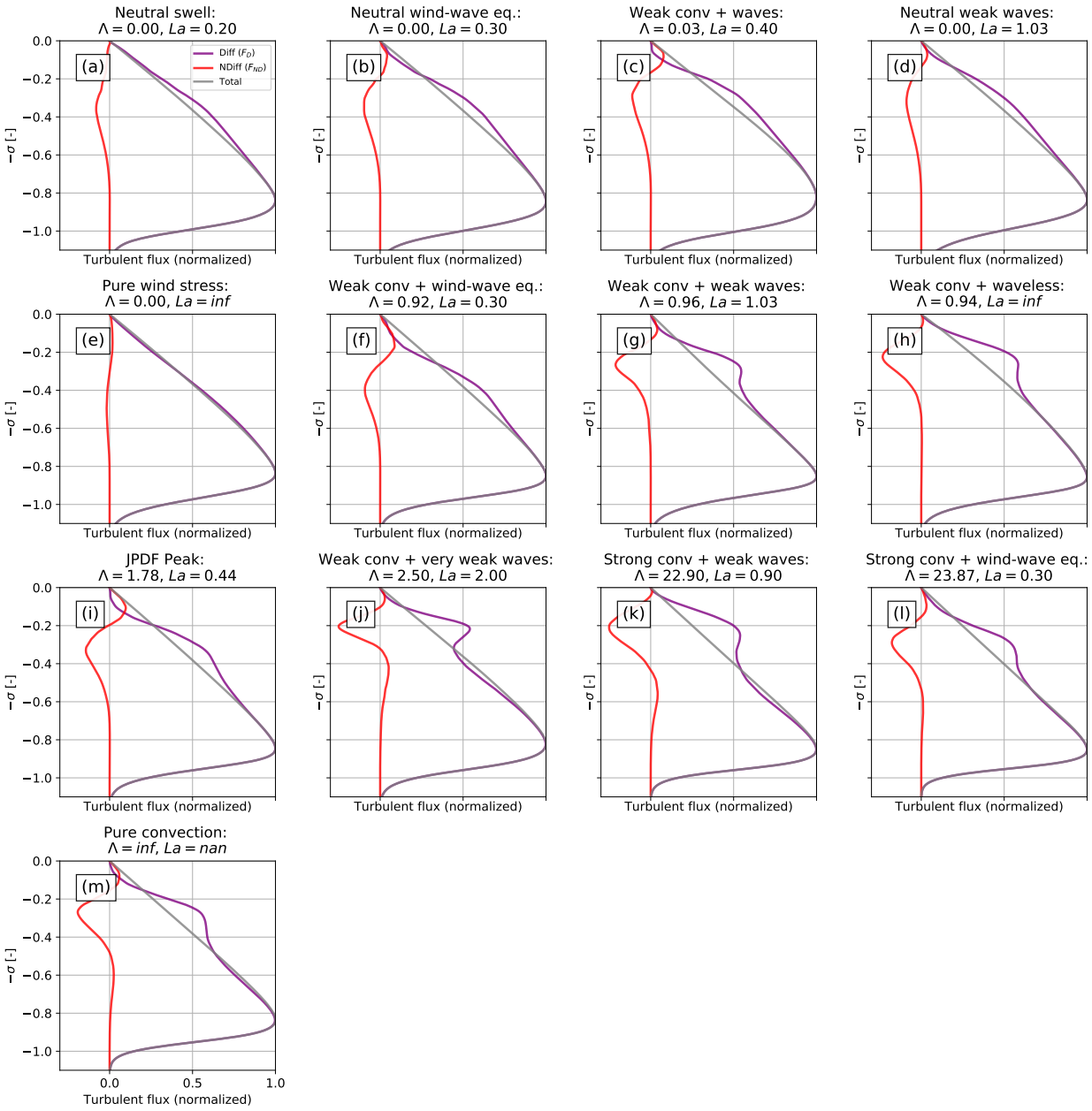

Figure D.2: EFT flux decompositions using the optimization method for all 13 simulations. Diffusive fluxes are shown in purple, nondiffusive fluxes are shown in blue and total fluxes are shown in gray.

Bibliography

[1] E. Eric Adams, Scott A. Socolofsky, and Michel Boufadel. “Comment on “Evolution of the Macondo Well Blowout: Simulating the Effects of the Circulation and Synthetic Dispersants on the Subsea Oil Transport””. In: *Environmental Science & Technology* 47.20 (2013). PMID: 24025026, pp. 11905–11905. DOI: 10.1021/es4034099.

[2] G.K. Batchelor. *An Introduction to Fluid Dynamics*. Cambridge University Press, 1973. ISBN: 9780521098175.

[3] Stephen E. Belcher, Alan L. M. Grant, Kirsty E. Hanley, Baylor Fox-Kemper, Luke Van Roekel, Peter P. Sullivan, William G. Large, Andy Brown, Adrian Hines, Daley Calvert, Anna Rutgersson, Heidi Pettersson, Jean-Raymond Bidlot, Peter A. E. M. Janssen, and Jeff A. Polton. “A global perspective on Langmuir turbulence in the ocean surface boundary layer: FRONTIER”. In: *Geophysical Research Letters* 39.18 (2012). DOI: 10.1029/2012GL052932.

[4] Elie Bou-Zeid, Charles Meneveau, and Marc Parlange. “A scale-dependent Lagrangian dynamic model for large eddy simulation of complex turbulent flows”. In: *Physics of Fluids* 17.2 (2005), p. 025105. DOI: 10.1063/1.1839152.

[5] K. E. Brainerd and M. C. Gregg. “Diurnal restratification and turbulence in the oceanic surface mixed layer: 1. Observations”. In: *Journal of Geophysical Research: Oceans* 98.C12 (1993), pp. 22645–22656. DOI: 10.1029/93JC02297.

[6] James G. Brasseur and Tie Wei. “Designing large-eddy simulation of the turbulent boundary layer to capture law-of-the-wall scaling”. In: *Physics of Fluids* 22.2 (2010), p. 021303. DOI: 10.1063/1.3319073.

[7] K. Brunner, T. Kukulka, G. Proskurowski, and K. L. Law. “Passive buoyant tracers in the ocean surface boundary layer: 2. Observations and simulations of microplastic marine debris”. In: *Journal of Geophysical Research: Oceans* 120.11 (2015), pp. 7559–7573. DOI: 10.1002/2015JC010840.

[8] Marcelo Chamecki, Tomas Chor, Di Yang, and Charles Meneveau. “Material transport in the ocean mixed layer: recent developments enabled by large eddy simulations”. In: *Reviews of Geophysics* 57.4 (2019), pp. 1338–1371. DOI: 10.1029/2019RG000655.

[9] Marcelo Chamecki, Charles Meneveau, and Marc B. Parlange. “A Hybrid Spectral/Finite-Volume Algorithm for Large-Eddy Simulation of Scalars in the Atmospheric Boundary Layer”. In: *Boundary-Layer Meteorology* 128.3 (2008), pp. 473–484. DOI: 10.1007/s10546-008-9302-1.

[10] Bicheng Chen, Di Yang, Charles Meneveau, and Marcelo Chamecki. “Effects of swell on transport and dispersion of oil plumes within the ocean mixed layer”. In: *Journal of Geophysical Research: Oceans* 121.5 (2016), pp. 3564–3578. DOI: 10.1002/2015JC011380.

[11] Bicheng Chen, Di Yang, Charles Meneveau, and Marcelo Chamecki. “ENDLESS: An extended nonperiodic domain large-eddy simulation approach for scalar plumes”. In: *Ocean Modelling* 101 (2016), pp. 121–132. DOI: 10.1016/j.ocemod.2016.04.003.

[12] Bicheng Chen, Di Yang, Charles Meneveau, and Marcelo Chamecki. “Numerical study of the effects of chemical dispersant on oil transport from an idealized underwater blowout”. In: *Phys. Rev. Fluids* 3 (8 2018), p. 083801. DOI: 10.1103/PhysRevFluids.3.083801.

[13] C T A Chen and E T Drake. “Carbon Dioxide Increase in the Atmosphere and Oceans and Possible Effects on Climate”. In: *Annual Review of Earth and Planetary Sciences* 14.1 (1986), pp. 201–235. DOI: 10.1146/annurev.ea.14.050186.001221.

[14] Katie E Cherry, Bethany A Lyon, Loren D Marks, Pam F Nezat, Rachel Adamek, S Devon Walsh, Kristina B Fitzgerald, Dina R Anbinder, and Claire V Bernacchio. “After the BP Deepwater Horizon oil spill: financial and health concerns among coastal residents and commercial fishers”. In: *Current Psychology* 34.3 (2015), pp. 576–586. DOI: 10.1007/s12144-015-9372-4.

[15] Maria J. Chinita, Georgios Matheou, and João Teixeira. “A Joint Probability Density–Based Decomposition of Turbulence in the Atmospheric Boundary Layer”. In: *Monthly Weather Review* 146.2 (2018), pp. 503–523. DOI: 10.1175/MWR-D-17-0166.1.

[16] Tomas Chor, James McWilliams, and Marcelo Chamecki. “On modifications to the K-Profile Parameterization for wave effects”. In: *Journal of Physical Oceanography* (2020), In preparation.

[17] Tomas Chor, James C. McWilliams, and Marcelo Chamecki. “Diffusive-nondiffusive flux decompositions in atmospheric boundary layers”. In: *Journal of the Atmospheric Sciences* (2020), pp. 1–55. DOI: 10.1175/JAS-D-20-0093.1.

[18] Tomas Chor, Di Yang, Charles Meneveau, and Marcelo Chamecki. “A Turbulence Velocity Scale for Predicting the Fate of Buoyant Materials in the Oceanic Mixed Layer”. In: *Geophysical Research Letters* 45.21 (2018), pp. 11–817. DOI: 10.1029/2018GL080296.

[19] Tomás Chor, Di Yang, Charles Meneveau, and Marcelo Chamecki. “Preferential concentration of noninertial buoyant particles in the ocean mixed layer under free convection”. In: *Phys. Rev. Fluids* 3 (2018), p. 064501. DOI: 10.1103/PhysRevFluids.3.064501.

[20] Jeff C. Clements and Thierry Chopin. “Ocean acidification and marine aquaculture in North America: potential impacts and mitigation strategies”. In: *Reviews in Aquaculture* 9.4 (2017), pp. 326–341. DOI: 10.1111/raq.12140.

[21] R. Clift, J.R. Grace, and M.E. Weber. *Bubbles, Drops, and Particles*. Dover Civil and Mechanical Engineering Series. Dover Publications, 2005. ISBN: 9780486445809.

[22] Stanley Corrsin. “Limitations of Gradient Transport Models in Random Walks and in Turbulence”. In: *Turbulent Diffusion in Environmental Pollution*. Ed. by F.N. Frenkiel and R.E. Munn. Vol. 18. Advances in Geophysics. Elsevier, 1975, pp. 25–60. DOI: 10.1016/S0065-2687(08)60451-3.

[23] A. D. D. Craik and S. Leibovich. “A rational model for Langmuir circulations”. In: *Journal of Fluid Mechanics* 73.3 (1976), pp. 401–426. DOI: 10.1017/S0022112076001420.

[24] Eric A D’Asaro. “Turbulence in the upper-ocean mixed layer”. In: *Annual review of marine science* 6 (2014), pp. 101–115. DOI: 10.1146/annurev-marine-010213-135138.

[25] Eric A. D'Asaro, Andrey Y. Shcherbina, Jody M. Klymak, Jeroen Molemaker, Guillaume Novelli, Cédric M. Guigand, Angelique C. Haza, Brian K. Haus, Edward H. Ryan, Gregg A. Jacobs, Helga S. Huntley, Nathan J. M. Laxague, Shuyi Chen, Falco Judt, James C. McWilliams, Roy Barkan, A. D. Kirwan, Andrew C. Poje, and Tamay M. Özgökmen. "Ocean convergence and the dispersion of flotsam". In: *Proceedings of the National Academy of Sciences* (2018). DOI: 10.1073/pnas.1718453115.

[26] Daniel P Dauhajre, James C McWilliams, and Yusuke Uchiyama. "Submesoscale coherent structures on the continental shelf". In: *Journal of Physical Oceanography* 47.12 (2017), pp. 2949–2976. DOI: 10.1175/JPO-D-16-0270.1.

[27] P.A. Davidson. *Turbulence: An Introduction for Scientists and Engineers*. Oxford University Press, 2004. ISBN: 9780191589850.

[28] H. A. R. De Bruin and N. J. Bink. "The use of σ T as a temperature scale in the atmospheric surface layer". In: *Boundary-Layer Meteorology* 70.1 (1994), pp. 79–93. DOI: 10.1007/BF00712524.

[29] JW Deardorff. "The counter-gradient heat flux in the lower atmosphere and in the laboratory". In: *Journal of the Atmospheric Sciences* 23.5 (1966), pp. 503–506. DOI: 10.1175/1520-0469(1966)023⟨0503:TCGHFI⟩2.0.CO;2.

[30] Donald W. Denbo and Eric D. Skyllingstad. "An ocean large-eddy simulation model with application to deep convection in the Greenland Sea". In: *Journal of Geophysical Research: Oceans* 101.C1 (1996), pp. 1095–1110. DOI: 10.1029/95JC02828.

[31] KL Denman and AE Gargett. "Biological-physical interactions in the upper ocean: the role of vertical and small scale transport processes". In: *Oceanographic Literature Review* 8.42 (1995), pp. 662–663. DOI: 10.1146/annurev.fl.27.010195.001301.

[32] M. A. Donelan and W. J. Pierson. "Radar scattering and equilibrium ranges in wind-generated waves with application to scatterometry". In: *Journal of Geophysical Research: Oceans* 92.C5 (1987), pp. 4971–5029. DOI: 10.1029/JC092iC05p04971.

[33] Han van Dop and Gé Verver. “Countergradient transport revisited”. In: *Journal of the atmospheric sciences* 58.15 (2001), pp. 2240–2247. DOI: 10.1175/1520-0469(2001)058⟨2240:CTR⟩2.0.CO;2.

[34] J.K. Eaton and J.R. Fessler. “Preferential concentration of particles by turbulence”. In: *International Journal of Multiphase Flow* 20.Supplement 1 (1994), pp. 169–209. DOI: 10.1016/0301-9322(94)90072-8.

[35] Zachary A. Elliott and Subhas K. Venayagamoorthy. “Evaluation of turbulent Prandtl (Schmidt) number parameterizations for stably stratified environmental flows”. In: *Dynamics of Atmospheres and Oceans* 51.3 (2011), pp. 137–150. DOI: 10.1016/j.dynatmoce.2011.02.003.

[36] J. G. Esler and H. M. Ramli. “Shear dispersion in the turbulent atmospheric boundary layer”. In: *Quarterly Journal of the Royal Meteorological Society* 143.705 (2017), pp. 1721–1733. DOI: 10.1002/qj.3039.

[37] Jim Ferry and S. Balachandar. “A fast Eulerian method for disperse two-phase flow”. In: *International Journal of Multiphase Flow* 27.7 (2001), pp. 1199–1226. DOI: 10.1016/S0301-9322(00)00069-0.

[38] Brian H. Fiedler. “An Integral Closure Model for the Vertical Turbulent Flux of a Scalar in a Mixed Layer”. In: *Journal of the Atmospheric Sciences* 41.4 (1984), pp. 674–680. DOI: 10.1175/1520-0469(1984)041⟨0674:AICMFT⟩2.0.CO;2.

[39] A E Gargett. “Ocean Turbulence”. In: *Annual Review of Fluid Mechanics* 21.1 (1989), pp. 419–451. DOI: 10.1146/annurev.fl.21.010189.002223.

[40] Khaled Ghannam, Tomer Duman, Scott T. Salesky, Marcelo Chamecki, and Gabriel Katul. “The non-local character of turbulence asymmetry in the convective atmospheric boundary layer”. In: *Quarterly Journal of the Royal Meteorological Society* 143.702 (2017), pp. 494–507. DOI: 10.1002/qj.2937.

[41] Fujihiro Hamba. “A modified first-order model for scalar diffusion in the convective boundary layer”. In: *Journal of the atmospheric sciences* 50.16 (1993), pp. 2800–2810. DOI: 10.1175/1520-0469(1993)050⟨2800:AMFOMF⟩2.0.CO;2.

[42] Peter E. Hamlington, Luke P. Van Roekel, Baylor Fox-Kemper, Keith Julien, and Gregory P. Chini. “Langmuir–Submesoscale Interactions: Descriptive Analysis of Multiscale Frontal Spindown Simulations”. In: *Journal of Physical Oceanography* 44.9 (2014), pp. 2249–2272. DOI: 10.1175/JPO-D-13-0139.1.

[43] Ramsey R Harcourt and Eric A D’Asaro. “Large-eddy simulation of Langmuir turbulence in pure wind seas”. In: *Journal of Physical Oceanography* 38.7 (2008), pp. 1542–1562. DOI: 10.1175/2007JPO3842.1.

[44] AAM Holtslag and Chin-Hoh Moeng. “Eddy diffusivity and countergradient transport in the convective atmospheric boundary layer”. In: *Journal of the Atmospheric Sciences* 48.14 (1991), pp. 1690–1698. DOI: 10.1175/1520-0469(1991)048⟨1690:EDACTI⟩2.0.CO;2.

[45] R.A. Houghton. “Balancing the Global Carbon Budget”. In: *Annual Review of Earth and Planetary Sciences* 35.1 (2007), pp. 313–347. DOI: 10.1146/annurev.earth.35.031306.140057.

[46] J. C. R. Hunt, J. C. Kaimal, and J. E. Gaynor. “Eddy structure in the convective boundary layer—new measurements and new concepts”. In: *Quarterly Journal of the Royal Meteorological Society* 114.482 (1988), pp. 827–858. DOI: 10.1002/qj.49711448202.

[47] Balaji Jayaraman and James G Brasseur. “The surprising transition in atmospheric boundary layer turbulence structure from neutral to moderately convective stability states and mechanisms underlying large-scale rolls”. In: (2018).

[48] BA Kader and AM Yaglom. “Mean fields and fluctuation moments in unstably stratified turbulent boundary layers”. In: *Journal of Fluid Mechanics* 212 (1990), pp. 637–662. DOI: 10.1017/S0022112090002129.

[49] B. Kadoch, D. del-Castillo-Negrete, W. J. T. Bos, and K. Schneider. “Lagrangian statistics and flow topology in forced two-dimensional turbulence”. In: *Phys. Rev. E* 83 (3 2011), p. 036314. DOI: 10.1103/PhysRevE.83.036314.

[50] J. C. Kaimal, J. C. Wyngaard, D. A. Haugen, O. R. Coté, Y. Izumi, S. J. Caughey, and C. J. Readings. “Turbulence Structure in the Convective Boundary Layer”. In: *Journal of*

the Atmospheric Sciences 33.11 (1976), pp. 2152–2169. DOI: 10.1175/1520-0469(1976)033⟨2152:TSITCB⟩2.0.CO;2.

[51] J.C. Kaimal and J.J. Finnigan. *Atmospheric Boundary Layer Flows: Their Structure and Measurement*. Atmospheric Boundary Layer Flow: Their Structure and Measurement. Oxford University Press, 1994. ISBN: 9780195062397.

[52] Gabriel G Katul, Alexandra G Konings, and Amilcare Porporato. "Mean velocity profile in a sheared and thermally stratified atmospheric boundary layer". In: *Physical review letters* 107.26 (2011), p. 268502. DOI: 10.1103/PhysRevLett.107.268502.

[53] Samir Khanna and James G Brasseur. "Analysis of Monin–Obukhov similarity from large-eddy simulation". In: *Journal of Fluid Mechanics* 345 (1997), pp. 251–286. DOI: 10.1017/S0022112097006277.

[54] M Köhler, M Ahlgrimm, and A Beljaars. "Unified treatment of dry convective and stratocumulus-topped boundary layers in the ECMWF model". In: *Quarterly Journal of the Royal Meteorological Society* 137.654 (2011), pp. 43–57. DOI: 10.1002/qj.713.

[55] T. Kukulka and K. Brunner. "Passive buoyant tracers in the ocean surface boundary layer: 1. Influence of equilibrium wind-waves on vertical distributions". In: *Journal of Geophysical Research: Oceans* 120.5 (2015), pp. 3837–3858. DOI: 10.1002/2014JC010487.

[56] T. Kukulka, Kara L. Law, and Giora Proskurowski. "Evidence for the Influence of Surface Heat Fluxes on Turbulent Mixing of Microplastic Marine Debris". In: *Journal of Physical Oceanography* 46.3 (2016), pp. 809–815. DOI: 10.1175/JPO-D-15-0242.1.

[57] T. Kukulka, A. J. Plueddemann, and P. P. Sullivan. "Inhibited upper ocean restratification in nonequilibrium swell conditions". In: *Geophysical Research Letters* 40.14 (2013), pp. 3672–3676. DOI: 10.1002/grl.50708.

[58] Vijayant Kumar, Jan Kleissl, Charles Meneveau, and Marc B Parlange. "Large-eddy simulation of a diurnal cycle of the atmospheric boundary layer: Atmospheric stability and scaling issues". In: *Water resources research* 42.6 (2006). DOI: 10.1029/2005WR004651.

[59] W. G. Large, J. C. McWilliams, and S. C. Doney. “Oceanic vertical mixing: A review and a model with a nonlocal boundary layer parameterization”. In: *Reviews of Geophysics* 32.4 (1994), pp. 363–403. DOI: 10.1029/94RG01872.

[60] William G Large, Edward G Patton, and Peter P Sullivan. “Nonlocal Transport and Implied Viscosity and Diffusivity throughout the Boundary Layer in LES of the Southern Ocean with Surface Waves”. In: *Journal of Physical Oceanography* 49.10 (2019), pp. 2631–2652. DOI: 10.1175/JPO-D-18-0202.1.

[61] Nathan J. M. Laxague, Tamay M. Özgökmen, Brian K. Haus, Guillaume Novelli, Andrey Shcherbina, Peter Sutherland, Cédric M. Guigand, Björn Lund, Sanchit Mehta, Matias Alday, and Jeroen Molemaker. “Observations of Near-Surface Current Shear Help Describe Oceanic Oil and Plastic Transport”. In: *Geophysical Research Letters* 45.1 (2018), pp. 245–249. DOI: 10.1002/2017GL075891.

[62] B Lehr, S Nristol, and A Possolo. “Oil Budget Calculator. Deepwater Horizon, Technical Documentation: A Report to the National Incident Command”. In: *Federal Interagency Solutions Group* (2010).

[63] S Leibovich. “The form and Dynamics of Langmuir Circulations”. In: *Annual Review of Fluid Mechanics* 15.1 (1983), pp. 391–427. DOI: 10.1146/annurev.fl.15.010183.002135.

[64] Dan Li. “Turbulent Prandtl number in the atmospheric boundary layer - where are we now?” In: *Atmospheric Research* 216 (2019), pp. 86–105. DOI: 10.1016/j.atmosres.2018.09.015.

[65] Ming Li, Chris Garrett, and Eric Skyllingstad. “A regime diagram for classifying turbulent large eddies in the upper ocean”. In: *Deep Sea Research Part I: Oceanographic Research Papers* 52.2 (2005), pp. 259–278. DOI: 10.1016/j.dsr.2004.09.004.

[66] Qing Li and Baylor Fox-Kemper. “Assessing the Effects of Langmuir Turbulence on the Entrainment Buoyancy Flux in the Ocean Surface Boundary Layer”. In: *Journal of Physical Oceanography* 47.12 (2017), pp. 2863–2886. DOI: 10.1175/JPO-D-17-0085.1.

[67] Qing Li, Brandon G. Reichl, Baylor Fox-Kemper, Alistair J. Adcroft, Stephen E. Belcher, Gokhan Danabasoglu, Alan L. M. Grant, Stephen M. Griffies, Robert Hallberg, Tetsu Hara, Ramsey R. Harcourt, Tobias Kukulka, William G. Large, James C. McWilliams, Brodie

Pearson, Peter P. Sullivan, Luke Van Roekel, Peng Wang, and Zhihua Zheng. “Comparing Ocean Surface Boundary Vertical Mixing Schemes Including Langmuir Turbulence”. In: *Journal of Advances in Modeling Earth Systems* 11.11 (2019), pp. 3545–3592. DOI: 10.1029/2019MS001810.

[68] Qing Li, Adrean Webb, Baylor Fox-Kemper, Anthony Craig, Gokhan Danabasoglu, William G Large, and Mariana Vertenstein. “Langmuir mixing effects on global climate: WAVEWATCH III in CESM”. In: *Ocean Modelling* 103 (2016), pp. 145–160.

[69] Jun-Hong Liang, James C. McWilliams, Peter P. Sullivan, and Burkard Baschek. “Modeling bubbles and dissolved gases in the ocean”. In: *Journal of Geophysical Research: Oceans* 116.C3 (2011). DOI: 10.1029/2010JC006579.

[70] Jun-Hong Liang, Xiaoliang Wan, Kenneth A. Rose, Peter P. Sullivan, and James C. McWilliams. “Horizontal Dispersion of Buoyant Materials in the Ocean Surface Boundary Layer”. In: *Journal of Physical Oceanography* 0.0 (2018), null. DOI: 10.1175/JPO-D-18-0020.1.

[71] D. K. Lilly. “The representation of small scale turbulence in numerical simulation experiments”. In: *Proceedings of the IBM Scientific Computing Symposium on environmental sciences*. Yorktown heights, 1967, pp. 195–210. DOI: 10.5065/D62R3PMM.

[72] Ziemowit Malecha, Greg Chini, and Keith Julien. “A multiscale algorithm for simulating spatially-extended Langmuir circulation dynamics”. In: *Journal of Computational Physics* 271 (2014), pp. 131–150. DOI: 10.1016/j.jcp.2013.07.003.

[73] Stuart Marlatt, Scott Waggy, and Sedat Biringen. “Direct Numerical Simulation of the Turbulent Ekman Layer: Evaluation of Closure Models”. In: *Journal of the Atmospheric Sciences* 69.3 (2012), pp. 1106–1117. DOI: 10.1175/JAS-D-11-0107.1.

[74] Jesús Martín, César Dopazo, and Luis Valiño. “Dynamics of velocity gradient invariants in turbulence: Restricted Euler and linear diffusion models”. In: *Physics of Fluids* 10.8 (1998), pp. 2012–2025. DOI: 10.1063/1.869717.

[75] M. R. Maxey. “The gravitational settling of aerosol particles in homogeneous turbulence and random flow fields”. In: *Journal of Fluid Mechanics* 174 (1987), pp. 441–465. DOI: 10.1017/S0022112087000193.

[76] James C McWilliams, Edward Huckle, Junhong Liang, and Peter P Sullivan. “Langmuir turbulence in swell”. In: *Journal of physical oceanography* 44.3 (2014), pp. 870–890.

[77] James C. McWilliams. *Fundamentals of Geophysical Fluid Dynamics*. Cambridge University Press, 2006. ISBN: 9780521856379.

[78] James C. McWilliams and Juan M. Restrepo. “The Wave-Driven Ocean Circulation”. In: *Journal of Physical Oceanography* 29.10 (1999), pp. 2523–2540. DOI: 10.1175/1520-0485(1999)029⟨2523:TWDOC⟩2.0.CO;2.

[79] James C. McWilliams and Peter P. Sullivan. “Vertical Mixing by Langmuir Circulations”. In: *Spill Science & Technology Bulletin* 6.3 (2000). Langmuir Circulation and Oil Spill Modeling, pp. 225–237. DOI: 10.1016/S1353-2561(01)00041-X.

[80] James C. McWilliams, Peter P. Sullivan, and Chin-Hoh Moeng. “Langmuir turbulence in the ocean”. In: *Journal of Fluid Mechanics* 334 (1997), pp. 1–30. DOI: 10.1017/S0022112096004375.

[81] W Kendall Melville. “The role of surface-wave breaking in air-sea interaction”. In: *Annual review of fluid mechanics* 28.1 (1996), pp. 279–321. DOI: 10.1146/annurev.fl.28.010196.001431.

[82] W Kendall Melville, Robert Shear, and Fabrice Veron. “Laboratory measurements of the generation and evolution of Langmuir circulations”. In: *Journal of Fluid Mechanics* 364 (1998), pp. 31–58. DOI: 10.1017/S0022112098001098.

[83] Irving A. Mendelssohn, Gary L. Andersen, Donald M. Baltz, Rex H. Caffey, Kevin R. Carman, John W. Fleeger, Samantha B. Joye, Qianxin Lin, Edward Maltby, Edward B. Overton, and Lawrence P. Rozas. “Oil Impacts on Coastal Wetlands: Implications for the Mississippi River Delta Ecosystem after the Deepwater Horizon Oil Spill”. In: *BioScience* 62.6 (2012), pp. 562–574. DOI: 10.1525/bio.2012.62.6.7.

[84] Charles Meneveau. “Lagrangian Dynamics and Models of the Velocity Gradient Tensor in Turbulent Flows”. In: *Annual Review of Fluid Mechanics* 43.1 (2011), pp. 219–245. DOI: 10.1146/annurev-fluid-122109-160708.

[85] Charles Meneveau and Joseph Katz. “Scale-Invariance and Turbulence Models for Large-Eddy Simulation”. In: *Annual Review of Fluid Mechanics* 32.1 (2000), pp. 1–32. DOI: 10.1146/annurev.fluid.32.1.1.

[86] Jean A. Mensa, Tamay M. Özgökmen, Andrew C. Poje, and Jörg Imberger. “Material transport in a convective surface mixed layer under weak wind forcing”. In: *Ocean Modelling* 96 (2015), pp. 226–242. DOI: 10.1016/j.ocemod.2015.10.006.

[87] Chin-Hoh Moeng and Peter P Sullivan. “A comparison of shear-and buoyancy-driven planetary boundary layer flows”. In: *Journal of the Atmospheric Sciences* 51.7 (1994), pp. 999–1022. DOI: 10.1175/1520-0469(1994)051⟨0999:ACOSAB⟩2.0.CO;2.

[88] Walter Munk, Laurence Armi, Kenneth Fischer, and F. Zachariasen. “Spirals on the sea”. In: *Proceedings of the Royal Society of London A: Mathematical, Physical and Engineering Sciences* 456.1997 (2000), pp. 1217–1280. DOI: 10.1098/rspa.2000.0560.

[89] Ramakrishna R Nemani, Michael A White, Daniel R Cayan, Gregory V Jones, Steven W Running, Joseph C Coughlan, and David L Peterson. “Asymmetric warming over coastal California and its impact on the premium wine industry”. In: *Climate research* 19.1 (2001), pp. 25–34. DOI: 10.3354/cr019025.

[90] Y. Noh, I. S. Kang, M. Herold, and S. Raasch. “Large eddy simulation of particle settling in the ocean mixed layer”. In: *Physics of Fluids* 18.8 (2006), p. 085109. DOI: 10.1063/1.2337098.

[91] Y. Noh and Satoshi Nakada. “Estimation of the particle flux from the convective mixed layer by large eddy simulation”. In: *Journal of Geophysical Research: Oceans* 115.C5 (2010). C05007, n/a–n/a. DOI: 10.1029/2009JC005669.

[92] James J O’Brien. “A note on the vertical structure of the eddy exchange coefficient in the planetary boundary layer”. In: *Journal of the Atmospheric Sciences* 27.8 (1970), pp. 1213–1215. DOI: 10.1175/1520-0469(1970)027⟨1213:ANOTVS⟩2.0.CO;2.

[93] Akira Okubo. “Horizontal dispersion of floatable particles in the vicinity of velocity singularities such as convergences”. In: *Deep Sea Research and Oceanographic Abstracts* 17.3 (1970), pp. 445–454. DOI: 10.1016/0011-7471(70)90059-8.

[94] Tamay M. Ozgokmen, Andrew C. Poje, Paul F. Fischer, and Angelique C. Haza. “Large eddy simulations of mixed layer instabilities and sampling strategies”. In: *Ocean Modelling* 39.3 (2011), pp. 311–331. DOI: 10.1016/j.ocemod.2011.05.006.

[95] Brodie C. Pearson, Alan L. M. Grant, Jeff A. Polton, and Stephen E. Belcher. “Langmuir Turbulence and Surface Heating in the Ocean Surface Boundary Layer”. In: *Journal of Physical Oceanography* 45.12 (2015), pp. 2897–2911. DOI: 10.1175/JPO-D-15-0018.1.

[96] J. Pedlosky. *Geophysical Fluid Dynamics*. 2nd ed. Springer study edition. Springer-Verlag New York, 1987. ISBN: 978-0-387-96387-7. DOI: 10.1007/978-1-4612-4650-3.

[97] Prasad Perlekar, Samriddhi Sankar Ray, Dhrubaditya Mitra, and Rahul Pandit. “Persistence Problem in Two-Dimensional Fluid Turbulence”. In: *Phys. Rev. Lett.* 106 (5 2011), p. 054501. DOI: 10.1103/PhysRevLett.106.054501.

[98] Marc Perlin, Wooyoung Choi, and Zhigang Tian. “Breaking waves in deep and intermediate waters”. In: *Annual review of fluid mechanics* 45 (2013), pp. 115–145. DOI: 10.1146/annurev-fluid-011212-140721.

[99] S.B. Pope. *Turbulent Flows*. Cambridge University Press, 2000. ISBN: 9780521598866.

[100] Fernando Porté-Agel, Charles Meneveau, and Marc B. Parlange. “A scale-dependent dynamic model for large-eddy simulation: application to a neutral atmospheric boundary layer”. In: *Journal of Fluid Mechanics* 415 (2000), pp. 261–284. DOI: 10.1017/S0022112000008776.

[101] L. Prandtl. “Bemerkungen zur Theorie der freien Turbulenz .” In: *ZAMM - Journal of Applied Mathematics and Mechanics / Zeitschrift für Angewandte Mathematik und Mechanik* 22.5 (1942), pp. 241–243. DOI: 10.1002/zamm.19420220502.

[102] James F. Price, Robert A. Weller, and Robert Pinkel. “Diurnal cycling: Observations and models of the upper ocean response to diurnal heating, cooling, and wind mixing”. In: *Journal of Geophysical Research: Oceans* 91.C7 (1986), pp. 8411–8427. DOI: 10.1029/JC091iC07p08411.

[103] Scott T. Salesky, Marcelo Chamecki, and Elie Bou-Zeid. “On the Nature of the Transition Between Roll and Cellular Organization in the Convective Boundary Layer”. In: *Boundary-Layer Meteorology* 163.1 (2017), pp. 41–68. DOI: 10.1007/s10546-016-0220-3.

[104] A Pier Siebesma, Pedro MM Soares, and João Teixeira. “A combined eddy-diffusivity mass-flux approach for the convective boundary layer”. In: *Journal of the atmospheric sciences* 64.4 (2007), pp. 1230–1248. DOI: 10.1175/JAS3888.1.

[105] J. Smagorinsky. “General Circulation Experiments with the Primitive Equations”. In: *Monthly Weather Review* 91.3 (1963), pp. 99–164. DOI: 10.1175/1520-0493(1963)091⟨0099:GCEWTP⟩2.3.CO;2.

[106] Katherine M. Smith, Peter E. Hamlington, and Baylor Fox-Kemper. “Effects of submesoscale turbulence on ocean tracers”. In: *Journal of Geophysical Research: Oceans* 121.1 (2016), pp. 908–933. DOI: 10.1002/2015JC011089.

[107] William D. Smyth, Eric D. Skyllingstad, Gregory B. Crawford, and Hemantha Wijesekera. “Nonlocal fluxes and Stokes drift effects in the K-profile parameterization”. In: *Ocean Dynamics* 52.3 (2002), pp. 104–115. DOI: 10.1007/s10236-002-0012-9.

[108] Roland B Stull. *An introduction to boundary layer meteorology*. Vol. 13. Springer Science & Business Media, 1988.

[109] Roland B. Stull. “Review of non-local mixing in turbulent atmospheres: Transilient turbulence theory”. In: *Boundary-Layer Meteorology* 62.1 (1993), pp. 21–96. DOI: 10.1007/BF00705546.

[110] Peter P. Sullivan and James C. McWilliams. “Dynamics of Winds and Currents Coupled to Surface Waves”. In: *Annual Review of Fluid Mechanics* 42.1 (2010), pp. 19–42. DOI: 10.1146/annurev-fluid-121108-145541.

[111] Peter P. Sullivan and Edward G. Patton. “The Effect of Mesh Resolution on Convective Boundary Layer Statistics and Structures Generated by Large-Eddy Simulation”. In: *Journal of the Atmospheric Sciences* 68.10 (2011-10), pp. 2395–2415. DOI: 10.1175/JAS-D-10-05010.1.

[112] Yuhei Takaya, Jean-Raymond Bidlot, Anton CM Beljaars, and Peter AEM Janssen. “Refinements to a prognostic scheme of skin sea surface temperature”. In: *Journal of Geophysical Research: Oceans* 115.C6 (2010). DOI: 10.1029/2009JC005985.

[113] Geoffrey I. Taylor. “Dispersion of soluble matter in solvent flowing slowly through a tube”. In: *Proceedings of the Royal Society of London A: Mathematical, Physical and Engineering Sciences* 219.1137 (1953), pp. 186–203. DOI: 10.1098/rspa.1953.0139.

[114] John Taylor. “Accumulation and Subduction of Buoyant Material at Submesoscale Fronts”. In: *Journal of Physical Oceanography* 48.6 (2018), pp. 1233–1241. DOI: 10.1175/JPO-D-17-0269.1.

[115] S.A. Thorpe. “Langmuir Circulation”. In: *Annual Review of Fluid Mechanics* 36.1 (2004), pp. 55–79. DOI: 10.1146/annurev.fluid.36.052203.071431.

[116] Kristen M. Thyng. “Deepwater Horizon Oil could have naturally reached Texas beaches”. In: *Marine Pollution Bulletin* 149 (2019), p. 110527. DOI: 10.1016/j.marpolbul.2019.110527.

[117] IB Troen and L Mahrt. “A simple model of the atmospheric boundary layer; sensitivity to surface evaporation”. In: *Boundary-Layer Meteorology* 37.1-2 (1986), pp. 129–148. DOI: 10.1007/BF00122760.

[118] Yusuke Uchiyama, Yota Suzue, and Hidekatsu Yamazaki. “Eddy-driven nutrient transport and associated upper-ocean primary production along the Kuroshio”. In: *Journal of Geophysical Research: Oceans* 122.6 (2017), pp. 5046–5062. DOI: 10.1002/2017JC012847.

[119] LP Van Roekel, B Fox-Kemper, PP Sullivan, PE Hamlington, and SR Haney. “The form and orientation of Langmuir cells for misaligned winds and waves”. In: *Journal of Geophysical Research: Oceans* 117.C5 (2012). DOI: 10.1029/2011JC007516.

[120] Pauli Virtanen et al. “SciPy 1.0–Fundamental Algorithms for Scientific Computing in Python”. In: *arXiv e-prints*, arXiv:1907.10121 (2019), arXiv:1907.10121.

[121] Dailin Wang. “Effects of the earth’s rotation on convection: Turbulent statistics, scaling laws and Lagrangian diffusion”. In: *Dynamics of Atmospheres and Oceans* 41.2 (2006), pp. 103–120. DOI: 10.1016/j.dynatmoce.2006.01.001.

[122] John Weiss. “The dynamics of enstrophy transfer in two-dimensional hydrodynamics”. In: *Physica D: Nonlinear Phenomena* 48.2 (1991), pp. 273–294. DOI: 10.1016/0167-2789(91)90088-Q.

[123] A. G. Williams and J. M. Hacker. “Interactions between coherent eddies in the lower convective boundary layer”. In: *Boundary-Layer Meteorology* 64.1 (1993), pp. 55–74. DOI: 10.1007/BF00705662.

[124] Achim Wirth. “On the Ekman spiral with an anisotropic eddy viscosity”. In: *Boundary-layer meteorology* 137.2 (2010), pp. 327–331. DOI: 10.1007/s10546-010-9527-7.

[125] Marcin L. Witek, Joao Teixeira, and Georgios Matheou. “An Integrated TKE-Based Eddy Diffusivity/Mass Flux Boundary Layer Closure for the Dry Convective Boundary Layer”. In: *Journal of the Atmospheric Sciences* 68.7 (2011), pp. 1526–1540. DOI: 10.1175/2011JAS3548.1.

[126] Boris Worm, Heike K. Lotze, Isabelle Jubinville, Chris Wilcox, and Jenna Jambeck. “Plastic as a Persistent Marine Pollutant”. In: *Annual Review of Environment and Resources* 42.1 (2017), pp. 1–26. DOI: 10.1146/annurev-environ-102016-060700.

[127] J.C. Wyngaard. *Turbulence in the Atmosphere*. Cambridge University Press, 2010. ISBN: 9781139485524.

[128] John C Wyngaard and Richard A Brost. “Top-down and bottom-up diffusion of a scalar in the convective boundary layer”. In: *Journal of the Atmospheric Sciences* 41.1 (1984), pp. 102–112. DOI: 10.1175/1520-0469(1984)041⟨0102:TDABUD⟩2.0.CO;2.

[129] John C Wyngaard and Jeffrey C Weil. “Transport asymmetry in skewed turbulence”. In: *Physics of Fluids A: Fluid Dynamics* 3.1 (1991), pp. 155–162. DOI: 10.1063/1.857874.

[130] Di Yang, Marcelo Chamecki, and Charles Meneveau. “Inhibition of oil plume dilution in Langmuir ocean circulation”. In: *Geophysical Research Letters* 41.5 (2014), pp. 1632–1638. DOI: 10.1002/2014GL059284.

[131] Di Yang, Bicheng Chen, Marcelo Chamecki, and Charles Meneveau. “Oil plumes and dispersion in Langmuir, upper-ocean turbulence: Large-eddy simulations and K-profile parameterization”. In: *Journal of Geophysical Research: Oceans* 120.7 (2015), pp. 4729–4759. DOI: 10.1002/2014JC010542.

[132] Di Yang, Bicheng Chen, Scott A. Socolofsky, Marcelo Chamecki, and Charles Meneveau. “Large-eddy simulation and parameterization of buoyant plume dynamics in stratified flow”. In: *Journal of Fluid Mechanics* 794 (2016), pp. 798–833. DOI: 10.1017/jfm.2016.191.

[133] Li Zheng and Poojitha D. Yapa. “Buoyant Velocity of Spherical and Nonspherical Bubbles/Droplets”. In: *Journal of Hydraulic Engineering* 126.11 (2000), pp. 852–854. DOI: 10.1061/(ASCE)0733-9429(2000)126:11(852).

[134] Bowen Zhou, Shiwei Sun, Kai Yao, and Kefeng Zhu. “Reexamining the Gradient and Countergradient Representation of the Local and Nonlocal Heat Fluxes in the Convective Boundary Layer”. In: *Journal of the Atmospheric Sciences* 75.7 (2018), pp. 2317–2336. DOI: 10.1175/JAS-D-17-0198.1.

[135] Sergej Zilitinkevich. “A generalized scaling for convective shear flows”. In: *Boundary-Layer Meteorology* 70.1 (1994), pp. 51–78. DOI: 10.1007/BF00712523.